



THE UNIVERSITY *of* EDINBURGH

This thesis has been submitted in fulfilment of the requirements for a postgraduate degree (e. g. PhD, MPhil, DClinPsychol) at the University of Edinburgh. Please note the following terms and conditions of use:

- This work is protected by copyright and other intellectual property rights, which are retained by the thesis author, unless otherwise stated.
- A copy can be downloaded for personal non-commercial research or study, without prior permission or charge.
- This thesis cannot be reproduced or quoted extensively from without first obtaining permission in writing from the author.
- The content must not be changed in any way or sold commercially in any format or medium without the formal permission of the author.
- When referring to this work, full bibliographic details including the author, title, awarding institution and date of the thesis must be given.

Machine Learning Aided Bioimpedance Tomography for Tissue Engineering

Zhou Chen



THE UNIVERSITY
of EDINBURGH

*A thesis submitted for the degree of
Doctor of Philosophy*
THE UNIVERSITY OF EDINBURGH

May 2023

This thesis is dedicated to my parents and brother

FENGBO CHEN
HONGLING ZHOU
and
YUANYANG CHEN

who have given me endless love, support and encouragement

Abstract

In tissue engineering, miniature Electrical Impedance Tomography (mEIT) (or bioimpedance tomography), is an emerging tomographic modality that contributes to non-destructive and label-free imaging and monitoring of 3-D cellular dynamics. The main challenge of mEIT comes from the nonlinear and ill-posed image reconstruction problem, leading to the increased sensitivity to imperfect measurement signals. Physical model-based image reconstruction methods have been successfully applied to conventional setups, but are less satisfying for the mEIT setup regarding image quality, conductivity retrieval and computational efficiency. Data-driven or learning-based methods have recently become a new frontier for tomographic image reconstruction, particularly for medical imaging modalities, e.g., Computed Tomography (CT), Positron Emission Tomography (PET), and Magnetic Resonance Imaging (MRI). However, the study of learning-based image reconstruction methods in challenging micro-scale sensor setups and the seamless integration of such algorithms with the tomography instrument remains a gap. This thesis aims to develop 2-D and 3-D imaging platforms integrating multi-frequency EIT and machine learning-based image reconstruction algorithms to extract spectroscopic electrical properties of 3-D cultivated cells under in vitro conditions, in a non-destructive, robust, and computation-efficient manner.

Recent advances in deep learning have pointed out a promising alternative for EIT image reconstruction. However, it is still challenging to image multiple objects with varying conductivity levels with a single neural network. A deep learning and group sparsity regularization-based hybrid image reconstruction framework was proposed to enable high-quality cell culture imaging with mEIT. A deep neural network was proposed to estimate the structural information in binary masks, given the limited number of data sets. Then the structural information is encoded in group sparsity regularization to obtain the final conductivity estimation. We validated our approach by imaging 3D cancer cell spheroids (MCF-7). Our method can be readily translated to spheroids, organoids, and cell culture in scaffolds of biomaterials. As the measured conductivity is a proxy for cell viability, mEIT has excellent potential to enable non-invasive, real-time, long-term monitoring of 3D cell growth, opening new avenues in regenerative medicine and drug testing.

Deep learning provides binary structural information in the above-mentioned hybrid learning approach, whereas the regularization algorithm determines conductivity contrasts. Despite the advancement of structure distribution, the exact conductivity values of different objects are less accurately estimated by the regularization-based framework, which essentially prevents EIT's transition from generating qualitative images to quantitative images. A structure-aware dual-branch deep learning method was proposed to further tackle this issue to predict

structure distribution and conductivity values. The proposed network comprises two independent branches to encode the structure and conductivity features, respectively, and the two branches are joined later to make final predictions of conductivity distributions. Numerical and experimental evaluation results on MCF-7 human breast cancer cell spheroids demonstrate the superior performance of the proposed method in dealing with the multi-level, continuous conductivity reconstruction problem.

Multi-frequency Electrical Impedance Tomography (mfEIT) is an emerging biomedical imaging modality to reveal frequency-dependent conductivity distributions in biomedical applications. Conventional model-based image reconstruction methods suffer from low spatial resolution, unconstrained frequency correlation and high computational cost. Most existing learning-based approaches deal with the single-frequency setup, which is inefficient and ineffective when extended to the multi-frequency setup. A Multiple Measurement Vector (MMV) model-based learning algorithm named MMV-Net was proposed to solve the mfEIT image reconstruction problem. MMV-Net considers the correlations between mfEIT images and unfolds the update steps of the Alternating Direction Method of Multipliers for the MMV problem (MMV-ADMM). The nonlinear shrinkage operator associated with the weighted $l_{1,2}$ regularization term of MMV-ADMM is generalized in MMV-Net with a cascade of a Spatial Self-Attention module and a Convolutional Long Short-Term Memory (ConvLSTM) module to capture intra- and inter-frequency dependencies better. The proposed MMV-Net was validated on our Edinburgh mfEIT Dataset and a series of comprehensive experiments. The results show superior image quality, convergence performance, noise robustness and computational efficiency against the conventional MMV-ADMM and the state-of-the-art deep learning methods.

Finally, few work on image reconstruction for Electrical Impedance Tomography (EIT) focuses on 3D geometries. Existing reconstruction algorithms adopt voxel grids for representation, which typically results in low image quality and considerable computational cost, and limits their applicability to real-time applications. In contrast, point clouds are a more efficient format for 3D surfaces, and such representation can naturally handle 3D shapes of arbitrary topologies with fine-grained details. Therefore, a learning-based 3D EIT reconstruction algorithm with efficient 3D representations (i.e., point cloud) was proposed to achieve higher image accuracy, spatial resolution and computational efficiency. A transformer-like point cloud network is adopted for 3D image reconstruction. This network simultaneously recovers the 3D coordinates of points to adaptively portray the objects' surface and predicts each point's conductivity. The results show that point cloud provides more efficient fine-shape descriptions and effectively alleviates computational costs.

In summary, the work demonstrated in this thesis addressed the research void in tissue imaging with bioimpedance tomography by developing learning-based imaging approaches. The results achieved in this thesis could promote bioimpedance tomography as a robust, intelligent imaging technique for tissue engineering applications.

Lay Summary

In tissue engineering, 3-D cell culture models are capable of mimicking the complexity and pathophysiology of “closer-to-in vivo” biological behaviour, which have become increasingly attractive in drug response studies, cancer research, gene and protein expression applications, etc. While traditional cellular assays are generally destructive and label-based, miniature bioimpedance tomography with specialized microelectrode arrays is potentially a rapid 3D tissue imaging method that can provide insight into 3D cell dynamics in a label-free and non-destructive manner.

Bioimpedance tomography is a tomographic imaging modality that images the 3D conductivity distribution within the Region of Interest (ROI) by measuring a sequence of differential voltages at the boundary of the ROI. Despite its intrinsic characteristics of portability, non-destructiveness, low-cost fabrication, and non-ionizing radiation, 3D tissue imaging with micro-scale impedance sensors has been particularly demanding in solving the image reconstruction problem, as the trend of sensor micro-miniaturization will lead to much weaker measurement signals and considerably increased sensitivity to sensor imperfection. Another critical challenge in the image reconstruction problem of bioimpedance tomography lies in its highly nonlinear and ill-conditioned characteristics, which further contribute to its susceptibility to distorted electric field lines and imperfect measurement data.

Focusing on these problems, this thesis systematically demonstrates the development of image reconstruction methods based on machine learning in challenging micro-scale sensor setups and the integration of such methods with the in-house developed 3D bioimpedance tomography system to promote the micro-scale bioimpedance tomography as a robust, intelligent tissue imaging technique for tissue engineering applications.

Acknowledgements

First and foremost words cannot express my deepest gratitude to my principal supervisor Dr. Yunjie Yang for his invaluable patience, continuous support, and guidance during my PhD study. His immense knowledge and plentiful experience have encouraged me in all the time of my academic research and daily life. This endeavour would not have been possible without his insightful comments and suggestions at every stage of this research. I would also like to thank my assistant supervisors, Dr. Jiabin Jia and Dr. Pierre Bagnaninchi, for their valuable suggestions and technical support on my PhD study.

I would like to highlight three truly exceptional colleagues, Dr. Delin Hu, Zhe Liu, and Dr. Jinxi Xiang, for their academic and coding support. It has been an amazing experience collaborating with them and being able to discuss ideas with them. They were always there for discussions about anything that I was unsure about.

I am also grateful to members of the Agile Tomography Group for their help, support, and friendship. They are Rui Zhang, Dr. Zhixi Zhang, Dr. Shengnan Wang, Dr. Haokun Wang, Yalei Fu, Jiangnan Xia, Yinghao Li, and Wei Han.

I would also like to express my special thanks to Miss Ke Xu for the mechanical keyboard, with which I accomplished this thesis smoothly.

Lastly, but most importantly, I would be remiss in not mentioning my family, especially my parents and brother. Their belief in me has kept my spirits and motivation high and made the past four years much more enjoyable throughout the whole process.

Declaration

I declare that this thesis was composed by myself, that the work contained herein is my own except where explicitly stated otherwise in the text, and that this work has not been submitted for any other degree or professional qualification except as specified.

Zhou Chen
25th May 2023

Contents

Abstract	iii
Lay Summary	v
Acknowledgements	vi
Declaration	vii
List of Figures	xi
List of Tables	xiv
Acronyms and Abbreviations	xv
Publication list	xvii
1 Introduction	1
1.1 Background and motivation	1
1.2 Aims and objectives	3
1.3 Main contribution	3
1.4 Overview of the thesis	4
2 Literature Review	5
2.1 Introduction	5
2.2 Electrical Impedance Tomography	5
2.2.1 Foundation of EIT	5
2.2.2 EIT for Tissue Engineering	7
2.3 EIT Image Reconstruction Algorithms	10
2.3.1 Model-based Methods	10
2.3.2 Learning-based Methods	16
2.3.3 Recent Challenge in Tissue Engineering	24
2.4 Summary	26
3 Cell Culture Imaging Using Hybrid Learning	27
3.1 Introduction	27
3.2 DL-GS: A Hybrid Learning Method for Cell Aggregate Imaging	28
3.2.1 DL-GS Framework	28
3.2.2 Evaluation Metrics	32

CONTENTS	ix
3.3 Experimental Setup	33
3.3.1 Data Set Generation	33
3.3.2 Data Normalization	35
3.3.3 Network Training	36
3.4 Results and Discussions	37
3.4.1 Learning Curve of FC-UNet	37
3.4.2 Results Based on Simulation Data	38
3.4.3 Results Based on Experimental Data	41
3.5 Summary	42
4 Cell Culture Imaging Using Structure-aware Learning	43
4.1 Introduction	43
4.2 SADB-Net: A Learning-based Method for Cell Culture Imaging	44
4.2.1 Multi-Modal Deep Neural Network	44
4.2.2 SADB-Net for EIT Image Reconstruction	45
4.2.3 Loss Function	47
4.2.4 Supervision Strategy	48
4.2.5 Evaluation Metrics	49
4.3 Experimental Setup	49
4.3.1 Training Data Generation	49
4.3.2 Network Training	51
4.3.3 Baseline	51
4.4 Results and Discussions	52
4.4.1 Evaluation on Simulation Data	52
4.4.2 Evaluation on Experimental Data	56
4.5 Summary	58
5 Multi-frequency Tissue Imaging with Model-based Learning	59
5.1 Introduction	59
5.2 MMV-Net: A Model-based Learning Method	60
5.2.1 Multi-frequency EIT	60
5.2.2 MMV-ADMM for mfEIT image reconstruction	61
5.2.3 MMV-Net for mfEIT image reconstruction	63
5.2.4 Network Training	68
5.3 Experiments and Results	68
5.3.1 The Edinburgh mfEIT Dataset	68
5.3.2 Evaluation on Simulation Data	69
5.3.3 Computational Complexity Evaluation	77
5.3.4 Evaluation on Experimental Data	78
5.4 Summary	80

CONTENTS	x
6 3D Tissue Imaging with Point Cloud Network	81
6.1 Introduction	81
6.2 Related Work	82
6.2.1 3D Representations	82
6.2.2 Transformer	83
6.3 Point Cloud Network	84
6.3.1 Problem Definition	84
6.3.2 Point Cloud Network	84
6.3.3 Network Training	87
6.4 Results and Discussion	87
6.4.1 3D EIT Dataset	87
6.4.2 Evaluation on Simulation Data	89
6.4.3 Evaluation on Experimental Data	93
6.5 Summary	95
7 Conclusions and Future Work	97
7.1 Conclusions	97
7.2 Future Work	99
Reference	101

List of Figures

2.1	Sensing schematic of EIT.	6
2.2	Comparison of 2D and 3D cell culture systems.	8
2.3	(a) An illustration of a typical deep architecture for image reconstruction. (b) Supervision strategy with mean squared error (MSE) as the objective function for training. (c) Multilayer Perceptron (MLP): neurons are fully connected at each layer. (d) Convolution: neurons are sparsely connected and restricted to local neighbours.	18
2.4	The generic pipeline of image post-processing approaches.	19
2.5	The network architecture of UNet.	20
2.6	The general idea of model-based deep learning approach based on algorithm unrolling. Starting from an iterative algorithm, a deep network is generated by cascading the iterations $g(\cdot; \boldsymbol{\theta})$ of the iterative algorithm. Each iteration is mapped into a network layer parameterized by $\boldsymbol{\theta}^k, k = 1, \dots, K_s$. Layer parameters can be shared across layers or layer-specific. Stacking K_s layers to construct a deep network is equivalent to executing the iterative algorithm with K_s iterations. Therefore, this network structure naturally inherits the interpretability from the physics of the iteration algorithm. The parameters $\{\boldsymbol{\theta}^1, \boldsymbol{\theta}^2, \dots, \boldsymbol{\theta}^{K_s}\}$ are learned through end-to-end training. (a) An abstract iterative image reconstruction algorithm. (b) The corresponding unrolled deep network.	22
3.1	Schematic illustration of the proposed DL-GS framework.	28
3.2	The architecture of FC-UNet.	29
3.3	Pixel grouping based on FC-UNet result.	31
3.4	A 4-object example of simulation data. (a) Boundary voltage change. (b) Corresponding conductivity distribution.	34
3.5	Experimental setup for carrot and rubber phantom. (a) The miniature EIT sensor (Y. Yang et al., 2016). (b) Carrot cylinder. (c) Rubber cylinder.	35
3.6	Experimental setup for cell imaging. (a) Sensor schematic. (b) The manufactured quasi-2D miniature EIT sensor (Y. Yang, Wu, & Jia, 2018). (c) MCF-7 cell aggregates.	36
3.7	The learning curves of the FC-UNet.	37
3.8	Multi-conductivity-level phantoms and binary masks generated by FC-UNet. (a) Ground Truth (b) Corresponding binary masks from FC-UNet.	38
3.9	Correlation coefficients of the FC-UNet results.	39

3.10	Image reconstruction results of four phantoms from testing data set (SNR = 50 dB) (note we use inverted color bar). (a) Ground truth (b)-(e) Corresponding results of l_1 , SBL, AGS, LeNet, and DL-GS respectively.	40
3.11	Image reconstruction results using experimental data (note we use inverted color bar). (a) Three setups. (b)-(e) corresponds to results of l_1 , SBL, AGS, LeNet, and DL-GS, respectively.	42
4.1	Schematic illustration of generic modality-specific deep neural network.	45
4.2	Schematic illustration of the proposed Structure-aware Dual-branch Network (SADB-Net).	46
4.3	Deep supervision of SADB-Net.	49
4.4	Sensor modelling and examples of nine patterns in the EIT data set.	50
4.5	Image reconstruction results based on simulation data (SNR = 50 dB) in testing set. Each column corresponds to a phantom.	53
4.6	Numerical comparisons of six phantoms based on <i>RIE</i>	53
4.7	(a) High-contrast profile in (3) of Fig. 4.5 and (b) low-contrast profile in (4) of Fig. 4.5.	54
4.8	Noise robustness comparison in terms of <i>RIE</i>	56
4.9	Experimental results on miniature EIT sensors. (a) Experiment phantom 1: cucumber and carrot cylinders. (b) Experiment phantom 2: potato and carrot cylinders. (c)-(d) Experiment phantom 3 and 4: two MCF-7 cell spheroids.	57
5.1	Illustration of intra- and inter-frequency correlation between mfEIT images.	63
5.2	(a) The iterative MMV-ADMM algorithm. (b) Illustration of the four updating steps at the k^{th} iteration corresponding to (5.10a)-(5.10d). (c) The overall architecture of the proposed MMV-Net. MMV-Net is an unrolled architecture for K_s iterations. It alternates among the four update steps. These update steps share parameters across all iterations.	64
5.3	Comparison of the proposed MMV-Net with the state-of-the-art imaging approaches on two simulated phantoms in the testing set.	71
5.4	Two failure cases of MMV-Net.	72
5.5	An example of image reconstruction results from ablation study.	73
5.6	Intermediate reconstructed images by MMV-Net, FISTA-Net and MMV-ADMM at different iterations.	75
5.7	Generalization ability study of different noise levels.	76
5.8	Convergence performance analysis on the testing set.	77
5.9	Experiment phantoms using two different 16-electrode EIT sensors. (a) Phantom 1: potato rod, sweet potato rod and metal rod. (b) Geometric distribution of phantom 1. (c) Phantom 2: potato rod and sweet potato rod. (d) Geometric distribution of phantom 2. (e) Phantom 3: sweet potato rod and plastic rod. (f) Geometric distribution of phantom 3. (g) Phantom 4: MCF-7 cell pellet	78

5.10	mfEIT image reconstruction results of four experimental phantoms.	79
6.1	The network architecture of the proposed point-cloud transformer for 3D EIT image reconstruction (ptEIT). The voltage measurement and position information are embedded and then mapped into a latent space by an encoder. Based on the latent code, the conductivity decoder estimates conductivity values \hat{Y}^C and makes constraints K on structural information for the shape decoder. Meanwhile, the measurement data is reused to provide an initial guess about the shape distribution $\hat{Y}^{S_{int}}$. With the latent code, the initial shape is fed into the shape decoder to reconstruct a fine-tuned shape \hat{Y}^S . Finally, \hat{Y}^C and \hat{Y}^S are concatenated to provide the targeted point cloud S . (a) The encoder $E(\cdot)$. (b) The conductivity decoder $D_c(\cdot)$. (c) The shape decoder $D_s(\cdot)$	85
6.2	(a) Sensor modelling: the inner diameter is 28.7 cm and the height is 20.6 cm. (b)-(c) An example of 3D conductivity distribution represented by point clouds and corresponding voltage measurement.	88
6.3	3D reconstruction results from the testing set. The ground truth, initial shapes where ptEIT starts from, and results of ptEIT are represented by point clouds, whereas the other two algorithms are based on the voxel grid. Apart from 3D reconstructions, two critical 2D slices for each 3D image are visualized for qualitative comparison. For each row, numerical coordinate ranges to generate 2D slices for point clouds correspond to slice numbers in voxel grids.	90
6.4	Qualitative comparison of the two learning-based algorithms. Cyan boxes: zoomed-in region of interest.	91
6.5	An example of qualitative results under different noise levels.	92
6.6	Experimental results on EIT sensors. For each row, numerical coordinate ranges for point clouds correspond to the selected 2D slice numbers for voxel grids. The results of ptEIT start from initial shapes. (a) Experiment phantom 1: a spheroid. (b) Experiment phantom 2: a cuboid (left) and a spheroid (right). (c) Experiment phantom 3: a conductive cuboid (upper left wrapped with copper) and a spheroid (lower right).	96

List of Tables

2.1	Comparison of representative model-based methods for EIT image reconstruction.	15
2.2	Recent representative learning-based methods for electrical tomographic image reconstruction.	23
2.3	Comparison of model-based and learning-based image reconstruction algorithms.	25
3.1	Number of samples in each data set	34
3.2	Comparison of average CC	40
3.3	Comparison of average model execution time per image [s]	40
3.4	CC of experimental results	41
4.1	Number of samples in each dataset	51
4.2	Performance comparisons (<i>RIE</i> and Speed) under different phantom patterns and noise levels.	55
5.1	Groups of simulated conductivity values at different frequencies.	69
5.2	Performance comparisons (PSNR, SSIM and RMSE) on the <i>Edinburgh mfEIT Dataset</i>	70
5.3	Ablation study on the validation set. (SSA: Spatial Self-attention Module; ConvLSTM: Convolutional LSTM Module.)	73
5.4	Improvement in reconstruction quality on validation data with the increasing number of iterations of the network.	74
5.5	Complexity evaluation. FPS means frame per second. FLOPS means floating point operations per second	77
5.6	Numerical comparisons of experimental results based on SSIM.	80
6.1	3D EIT dataset constitution. For each object, the conductivity value and geometry are randomly selected from the given sets.	88
6.2	Numerical comparisons (OWCD, OWHD, CA, RMSE, SSIM, FPS, and FLOPS) on the testing set.	89
6.3	Evaluation on the testing set under different noise levels.	92
6.4	Visual quality under different point resolutions and evaluation metrics.	94

Acronyms and Abbreviations

1D, 2D, 3D	1 Dimensional, 2 Dimensional, 3 Dimensional
AGS	Adaptive Group Sparsity
ADMM	Alternating Direction Method of Multipliers
BCE	Binary Cross Entropy
CD	Chamfer Distance
CEM	Complete Electrode Model
CGO	Complex Geometrical Optics
CT	Computed Tomography
CV	Computer Vision
ConvLSTM	Convolutional Long Short-Term Memory
CNN	Convolutional Neural Network
CC	Correlation Coefficient
CF	cystic fibrosis
DNN	Deep Neural Network
DC-DLS	Dominant-Current Deep Learning Scheme
EMD	Earth Mover's Distance
ECT	Electrical Capacitance Tomography
EIS	Electrical Impedance Spectroscopy
EIT	Electrical Impedance Tomography
ERT	Electrical Resistance Tomography
EMT	Electromagnetic Tomography
FISTA	Fast Iterative Shrinkage and Thresholding Algorithm
FEM	Finite Element Method
FLOPS	Floating Point Operations Per Second
FPS	Frame Per Second
FD	Frequency Difference
fdEIT	frequency-difference EIT
GS	Group Sparsity
HD	Hausdorff Distance
ISTA	Iterative Shrinkage and Thresholding Algorithm
Lap	Laplacian filter
LS	Least-squares
MAP	Maximum <i>a posteriori</i>
MRI	Magnetic Resonance Imaging
MSE	Mean Squared Error

mEIT	miniature EIT
MA	Modality-specific Architecture
mfEIT	multi-frequency EIT
MLP	Multilayer Perceptron
MMV	Multiple Measurement Vector
MR	Multiplicative Regularization
NLP	Natural Language Processing
ND	Neumann-to-Dirichlet
OWCD	Object-Wise CD
OWHD	Object-Wise HD
PSNR	Peak Signal to Noise Ratio
PLA	polylactide
PET	Positron Emission Tomography
ReLU	Rectified Linear Unit
RNN	Recurrent Neural Network
ROI	Region Of Interest
RIE	Relative Image Error
RBM	Restricted Boltzmann Machine
RMSE	Root Mean Square Error
SNR	Signal-to-Noise Ratio
SBL	Sparse Bayesian Learning
SSA	Spatial Self-Attention
SSIM	Structural Similarity Index Measure
SADB-Net	Structure-Aware Dual-Branch Network
SA-SBL	Structure-Aware Sparse Bayesian Learning
TD	Time Difference
TV	Total Variation
TEER	Trans-epithelial Electrical Resistance

Publication list

Journal Papers

1. **Z. Chen**, H. Zhang, D. Hu, Z. Liu, C. Tan, and Y. Yang, "ptEIT: Point-cloud Transformer for 3D Electrical Impedance Tomography," *IEEE Trans. Pattern Anal. Mach. Intell.*, submitted.
2. Z. Liu*, **Z. Chen***, and Y. Yang, "Review of Machine Learning for Bioimpedance Tomography in Regenerative Medicine," *Diverse Perspectives and State-of-the-Art Approaches to the Utilization of Data-Driven Clinical Decision Support Systems*, pp. 271-292. IGI Global, 2023.
3. **Z. Chen**, Z. Liu, L. Ai, S. Zhang, and Y. Yang, "Mask-guided Spatial-Temporal Graph Neural Network for Multi-frequency Electrical Impedance Tomography in Cell Culture Imaging," *IEEE Trans. Instrum. Meas.*, vol. 71, 2022.
4. **Z. Chen**, J. Xiang, P. Bagnaninchi, and Y. Yang, "MMV-Net: A Multiple Measurement Vector Network for Multi-frequency Electrical Impedance Tomography," *IEEE Trans. Neural Netw. Learn. Syst.*, doi: 10.1109/TNNLS.2022.3154108, 2022.
5. **Z. Chen**, and Y. Yang, "Structure-Aware Dual-Branch Network for Electrical Impedance Tomography in Cell Culture Imaging," *IEEE Trans. Instrum. Meas.*, vol. 70, 2021.
6. **Z. Chen**, Y. Yang, and P. Bagnaninchi, "Hybrid Learning based Cell Aggregate Imaging with Miniature Electrical Impedance Tomography," *IEEE Trans. Instrum. Meas.*, vol. 70, 2021.
7. Z. Liu, H. Gu, **Z. Chen**, P. Bagnaninchi, and Y. Yang, "Dual-modal Image Reconstruction for Electrical Impedance Tomography with Overlapping Group Lasso and Laplacian Regularization," *IEEE Trans. Biomed. Eng.*, 2023.
8. Z. Liu, **Z. Chen**, Q. Wang, S. Zheng, and Y. Yang, "Regularized Shallow Image Prior for Electrical Impedance Tomography," *IEEE Trans. Pattern Anal. Mach. Intell.*, submitted.
9. D. Hu, **Z. Chen**, P. Baisamy, Z. Liu, F. Giorgio-Serchi, and Y. Yang, "Simultaneous touch recognition and deformation tracking of soft manipulators with capacitive e-skin and deep learning," *Soft Robotics*, submitted.

Conference Papers

1. **Z. Chen**, Z. Liu, and Y. Yang, "3D EIT Image Reconstruction Based on Point Cloud Network," in *EIT 2023*, Aachen, Germany, 2023, accepted.
2. **Z. Chen**, Z. Liu, and Y. Yang, "3D Tissue Imaging with 3D Graph Neural Network," in *BioMedEng22*, London, 2022.

3. **Z. Chen**, Y. Yang, and P. Bagnaninchi, "3D Cell Culture Imaging Using Hybrid Learning Assisted Miniature Electrical Impedance Tomography," in *6th World Congress of the Tissue Engineering and Regenerative Medicine International Society (TERMIS2021)*, Maastricht, the Netherlands, 2021.
4. **Z. Chen**, Y. Yang, J. Jia, and P. Bagnaninchi, "Deep Learning Based Cell Imaging with Electrical Impedance Tomography," in *2020 IEEE International Instrumentation and Measurement Technology Conference (I2MTC)*, Dubrovnik, Croatia, 2020.
5. Z. Liu, **Z. Chen**, and Y. Yang, "Impedance-optical Dual-modal Imaging for 3D Cell Culture," in *EIT 2023*, Aachen, Germany, 2023, accepted.
6. Z. Liu, H. Dong, **Z. Chen**, and Y. Yang, "Gradient-Guided Multi-Modal Image Reconstruction for Electrical Impedance Tomography," in *2023 IEEE International Instrumentation and Measurement Technology Conference (I2MTC)*, 2023.
7. Z. Liu, **Z. Chen**, P. Bagnaninchi, and Y. Yang, "Structure-function Joint Imaging using Optical Coherence and Bioimpedance Tomography for Tissue Engineering," in *Bio-MedEng22*, London, 2022.
8. J. Xiang, **Z. Chen**, Y. Dong, and Y. Yang, "Image Reconstruction for Multi-frequency Electromagnetic Tomography based on Multiple Measurement Vector Model," in *2020 IEEE International Instrumentation and Measurement Technology Conference (I2MTC)*, Dubrovnik, Croatia, 2020.

Introduction

1.1 Background and motivation

Standard two-dimensional (2-D) cell culture which cultivates mono-layer cells possesses considerable limitations in mimicking the complexity and pathophysiology of in vivo conditions in tissue engineering (Vinci et al., 2012). In contrast, three-dimensional (3-D) cell culture models present “closer-to-in vivo” biological behaviour and therefore have been extensively applied in drug response studies, cancer research, gene and protein expression applications, etc. (Ravi, Paramesh, Kaviya, Anuradha, & Solomon, 2015). Compared to traditional cellular assay methods that are destructive and label-based, rapid imaging in a label-free, non-destructive manner has been increasingly attractive in tissue engineering (Justice, Badr, & Felder, 2009).

Recent research (Y. Yang, Wu, Jia, & Bagnaninchi, 2019) pointed out the potential of miniature Electrical Impedance Tomography (EIT) with specialized microelectrode arrays in non-destructive and label-free imaging of cellular dynamics. EIT is a tomographic modality that images the cross-section conductivity distribution within the Region of Interest (ROI) via measuring differential voltages at the boundary of the ROI. On account of its intrinsic characteristics of non-destructiveness, low-cost fabrication, portability, non-ionizing radiation and real-time imaging capability, EIT has been extensively exploited in functional lung imaging (Schullcke et al., 2016), cell culture imaging (Y. Yang et al., 2016), and cell-drug response imaging (H. Wu, Yang, Bagnaninchi, & Jia, 2018) over the last decades.

Among the aforementioned biomedical applications, 3D cell culture imaging with miniature EIT sensors has been particularly demanding in solving the image reconstruction problem, as the trend of sensor micro-miniaturization (H. Wu, Yang, et al., 2018; Y. Yang et al., 2016) will lead to much weaker measurement signals and considerably increased sensitivity to sensor imperfection. Therefore, performing robust, high-quality image reconstruction with high spatial resolution becomes essential. In addition, the need to process large amounts of sensing data sequences in real-time imaging settings suggests that high computational efficiency is preferable.

Another critical challenge in the EIT image reconstruction problem is its highly nonlinear and ill-conditioned characteristics, which further contributes to its susceptibility to imperfect measurement data (Lu et al., 2011). Most physical model-based image reconstruction methods linearize the EIT model and approximate the solution by minimizing least square errors and introducing various regularization terms that encode prior information. Prevailing algorithms of this kind include l_1 regularization (Tehrani, McEwan, Jin, & Van Schaik, 2012), Adaptive Group Sparsity (AGS) regularization (Y. Yang & Jia, 2017a), etc. In addition, image reconstruction approaches from statistical perspectives stimulate novel insights. Examples include Structure-Aware Sparse Bayesian Learning (SA-SBL) for 2D image reconstruction (S. Liu, Jia, Zhang, & Yang, 2018) and its extended version to deal with 3D geometries (S. Liu, Wu, Huang, Yang, & Jia, 2019). Whilst time-consuming, results of these methods suggest that introducing structural sparsity information as prior knowledge leads to significant improvement of image quality. Despite the remarkable progress of these state-of-the-art algorithms, improvements are still in demand in terms of spatial resolution, noise reduction performance and computational efficiency to facilitate high-quality cell culture imaging with the miniature EIT setup.

Data-driven or learning-based methods have recently become a new frontier for tomographic image reconstruction, particularly for mature medical imaging modalities (G. Wang, Ye, Mueller, & Fessler, 2018). Significant improvements in image quality and fast inference capability contribute to their growing popularity, although these methods rely heavily on the quality and availability of training data sets, and their training time is usually considerable. According to G. Wang et al. (2018), existing learning-based image reconstruction algorithms for Computed Tomography (CT), Positron Emission Tomography (PET), Magnetic Resonance Imaging (MRI), and Photoacoustic Tomography can be generally classified as (a) image domain learning, which mainly removes artefacts of post-reconstructed images, (b) data domain learning, a more aggressive strategy that directly maps measurement data to images, (c) hybrid methods, which uses machine learning to provide image prior, and (d) end-to-end workflows, where image reconstruction and analysis are trained jointly. In electrical tomography, Zheng et al. (2018) proposed an auto-encoder structure and Tan, Lv, Dong, and Takei (2018) employed a LeNet-like network to reconstruct tomographic images, both mapping directly the measurement data to 2D images. These pioneering studies utilize data domain learning structure, demonstrating the superiority of deep learning methods over conventional image reconstruction methods under conventional sensing setups. However, thus far, the application of learning-based image reconstruction methods in more challenging miniature EIT sensor setups remains unexplored.

1.2 Aims and objectives

Based on the existing EIT system and miniature EIT sensors developed in the research group (Y. Yang & Jia, 2017b), this thesis aims to develop a 2D and 3D imaging platform integrating multi-frequency EIT and machine-learning based image reconstruction algorithms, to extract spectroscopic electrical properties of 3D cultivated cells under in vitro conditions, in a non-destructive, robust and computation-efficient manner. Specific targets include EIT data generation, advanced learning-based 2D and 3D reconstruction algorithms, and algorithm evaluation on simulation and experimental data. The ultimate goal is to promote miniature EIT as a robust cellular imaging technique for tissue engineering applications. Distinct objectives are listed as follows:

1. Establish multi-physics simulation-based tissue imaging datasets with a considerable number and diversity of conductivity distributions.
2. Explore various machine learning methods to tackle the 2D and 3D EIT inverse problems and improve reconstructed image quality.
3. Conduct substantial quantitative and qualitative experimental evaluation of the developed methods in micro-scale setups for cell imaging.

1.3 Main contribution

The main contributions of this thesis are summarised as follows:

1. A large-scale ($\sim 75k$ samples) EIT dataset that mimics tissue engineering applications was generated via simulation for machine learning algorithm development and analysis. This dataset is made open-sourced at: *Edinburgh EIT Dataset* and *Edinburgh mfEIT Dataset*, which can serve as a benchmark for the EIT community.
2. Two image reconstruction algorithms based on hybrid learning and deep learning were proposed for cell aggregate imaging with miniature EIT (mEIT). The proposed approaches can address the multi-level, continuous conductivity reconstruction problem and demonstrate superior performance in terms of image quality, computational efficiency and generalization ability compared to existing algorithms.
3. A Multiple Measurement Vector (MMV) model-based learning algorithm named MMV-Net was proposed to address the simultaneous image reconstruction problem of multi-frequency EIT (mfEIT). The proposed MMV-Net outperformed the state-of-the-art methods regarding image quality, generalization ability, noise robustness and convergence performance.
4. A transformer-like point cloud network was proposed to tackle the challenging 3D EIT image reconstruction problem. Compared to voxel grid-based representation, point cloud provides more efficient fine-shape descriptions. The proposed point cloud network outperformed the existing 3D EIT image reconstruction methods.

These contributions can assist in promoting bioimpedance tomography as an effective real-time imaging modality for 3D cell culture systems. Relevant outcomes have been published in or submitted to renowned journals and international conferences as given in the publication list.

1.4 Overview of the thesis

The thesis comprises seven chapters, and the remainder is structured as follows. Following the introductory part, Chapter 2 provides a brief review of the foundation of EIT, the application of EIT in tissue engineering, the state-of-the-art EIT image reconstruction algorithms, and the recent challenge in tissue engineering.

Chapter 3 presents the development of a novel Deep Neural Network (DNN) and physical model-based hybrid image reconstruction framework to address the challenging multi-conductivity-level EIT image reconstruction problem frequently encountered in cell imaging. The proposed framework first leverages DNN to predict binary structural information and then determines the conductivity in a continuous manner using regularization. The effectiveness and superiority of this framework are verified based on phantom simulation and real-world data on MCF-7 breast cancer cell aggregates.

Chapter 4 proposes another 2D image reconstruction algorithm using a structure-aware dual-branch deep learning method to accurately predict the exact conductivity values while preserving the structure distribution. Two independent branches learn the structural and conductivity features in the first place, which are subsequently fused to make final predictions on conductivity distributions. The results demonstrate the superior performance of the proposed method in dealing with the multilevel, continuous conductivity reconstruction problem.

Chapter 5 develops an effective model-based deep learning approach to solve the mfEIT-image-reconstruction problem. The proposed approach unrolls an iterative algorithm for mfEIT into a single pipeline to incorporate the advantages of both the physical model and deep network. *Edinburgh mfEIT Dataset* and various real-world experiments validate the proposed approach's superior reconstruction quality, convergence performance, and noise robustness.

Chapter 6 introduces an efficient point-cloud-based 3D reconstruction network directly working on 3D geometries. Even with limited points to describe fine-grained details of 3D surfaces, the transformer-like point cloud network exhibits the superior performance of reconstruction quality over voxel-based 3D reconstruction algorithms.

Finally, Chapter 7 summarises the scientific contribution of this thesis and discusses future work.

Literature Review

2.1 Introduction

This chapter succinctly reviews the foundation of EIT, based on which the emerging application of EIT in tissue engineering is comprehensively reviewed. Furthermore, the state-of-the-art EIT image reconstruction algorithms are summarised, including model-based and learning-based methods. Finally, the recent challenge of EIT imaging in tissue engineering is discussed.

2.2 Electrical Impedance Tomography

2.2.1 Foundation of EIT

EIT is an emerging medical imaging modality that visualizes the conductivity distribution $\sigma \in \mathbb{R}^n$ inside the sensing region Ω by injecting currents I into electrode pairs and detecting the induced boundary voltages \mathbf{V} at the remaining electrode pairs (see illustration in Fig. 2.1). The numerical computation of boundary voltage measurements is termed the forward problem of EIT, which can be most accurately described by the Complete Electrode Model (CEM) (Cheng, Isaacson, Newell, & Gisser, 1989). Let N be the number of electrodes attached at the boundary $\partial\Omega$, and n be the outward unit normal of $\partial\Omega$. With CEM, the potential \mathbf{u} can be calculated using

$$\nabla \cdot (\sigma \nabla \mathbf{u}) = 0, \quad x \in \Omega \quad (2.1)$$

$$\mathbf{u} + z_\ell \sigma \frac{\partial \mathbf{u}}{\partial n} = U_\ell, \quad x \in e_\ell, \ell = 1, \dots, N \quad (2.2)$$

$$\int_{e_\ell} \sigma \frac{\partial \mathbf{u}}{\partial n} dS = I_\ell, \quad x \in e_\ell, \ell = 1, \dots, N \quad (2.3)$$

$$\sigma \frac{\partial \mathbf{u}}{\partial n} = 0, \quad x \in \partial\Omega \setminus \cup_{\ell=1}^N e_\ell \quad (2.4)$$

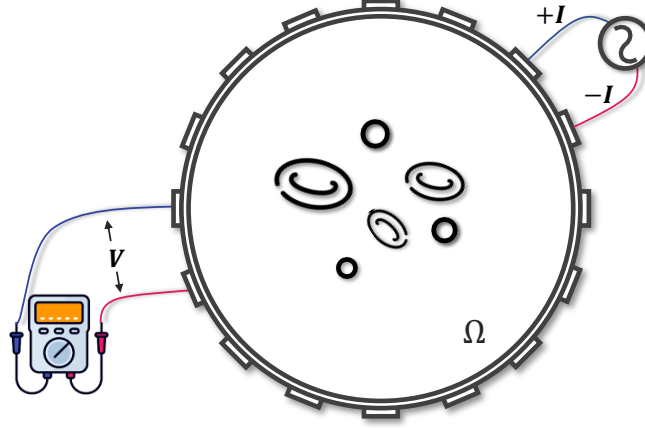


Figure 2.1: Sensing schematic of EIT.

where e_ℓ represents the ℓ th electrode; z_ℓ , I_ℓ , and U_ℓ denote contact impedance, injected currents and corresponding potential on e_ℓ , respectively. The conservation of the charge and the choice of the reference point are added to CEM for the existence and uniqueness of the solution \mathbf{u} , which are expressed as

$$\sum_{\ell=1}^N I_\ell = 0, \quad \sum_{\ell=1}^N V_\ell = 0. \quad (2.5)$$

The resulting voltage measurements $\mathbf{V} \in \mathbb{R}^m$ are then used to reconstruct the discrete spatial conductivity distribution $\boldsymbol{\sigma}$ within the ROI through reconstruction algorithms, which is termed the inverse problem of EIT (or EIT image reconstruction problem). The nonlinear relationship between \mathbf{V} and $\boldsymbol{\sigma}$ can be generally described as:

$$\mathbf{V} = F(\boldsymbol{\sigma}) + \mathbf{e} \quad (2.6)$$

where $F(\cdot)$ represents the nonlinear forward operator, and \mathbf{e} is the noise vector. To eliminate the common modelling errors, difference imaging is usually considered, wherein (2.6) is linearized by assuming a perturbation of conductivity distribution $\Delta\boldsymbol{\sigma} \in \mathbb{R}^n$. The change of induced boundary voltages $\Delta\mathbf{V} \in \mathbb{R}^m$ can be approximated by

$$\Delta\mathbf{V} = \mathbf{J}\Delta\boldsymbol{\sigma} + \mathbf{e} \quad (2.7)$$

where $\mathbf{J} \in \mathbb{R}^{m \times n}$ donates the Jacobian matrix (also known as the sensitivity matrix). The sensitivity at the k^{th} pixel of the sensing region is calculated by

$$\mathbf{J}_{ij}(k) = \frac{\partial V_{ij}}{\partial \sigma_k} = - \int_{\text{pixel } k} \nabla \mathbf{u}(I_i) \cdot \nabla \mathbf{u}(I_j) dV \quad (2.8)$$

where $\nabla \mathbf{u}(I_i)$ and $\nabla \mathbf{u}(I_j)$ are gradients of the potential fields \mathbf{u} , when the current is injected into the i^{th} and j^{th} electrode pairs, respectively.

Conventionally, the EIT image reconstruction problem based on (2.7) can be formulated as the following constrained problem:

$$\begin{cases} \min_{\Delta \sigma} \mathcal{R}(\Delta \sigma) \\ \text{s.t. } \mathbf{J} \Delta \sigma = \Delta \mathbf{V} \end{cases} \quad (2.9)$$

where \mathcal{R} denotes the regularization function, which integrates the prior knowledge of $\Delta \sigma$.

2.2.2 EIT for Tissue Engineering

EIT has appealing properties of non-destructiveness, low cost, portability, radiation-free measurement and real-time imaging capability, making it an up-and-coming candidate in biomedical imaging, including functional lung imaging (Santos, Czaplik, Orschulik, Hochhausen, & Leonhardt, 2018; Schullcke et al., 2016), biological tissue imaging (A. Adler & Boyle, 2017; Ahn, Oh, Jun, Seo, & Woo, 2011), stroke diagnosis (Goren et al., 2018; McDermott et al., 2020), breast cancer detection (Choi, Kao, Isaacson, Saulnier, & Newell, 2007; Sadleir, Sajib, Kim, Kwon, & Woo, 2013) and brain imaging (Goren et al., 2018; Romsauerova et al., 2006). This thesis mainly focuses on miniature EIT for tissue engineering, particularly 3D cell culture imaging.

Tissue engineering combines biology with engineering aiming at cultivating functional tissues or cellular products in vitro to restore or improve malfunctioning tissues in the human body. Before in vivo transplantation, it takes days to grow fully differentiated and mature 3D tissues or cells (Carlson, Alt-Holland, Egles, & Garlick, 2008; Rahman, Register, Vuppala, & Bhansali, 2008; H. Wu, Yang, et al., 2018). 3D cell culture can better mimic the function of living tissues based on the cellular responses to drugs/compounds/external stimuli compared to cell monolayers (see Fig. 2.2). 3D in vitro models are promising for drug screening, cancer research, gene and protein expression applications, and cell-based analysis (Ravi et al., 2015). Providing better models of cell behavior may benefit the study and treatment of human diseases, reduce animal testing, and facilitate the development of decisional tools in regenerative medicine. A key challenge in 3D cell culture is determining the cellular state in-depth and over time. This process requires real-time monitoring, visualization, and evaluation of tissue-engineered cultures to control and optimize cellular functions, e.g., growth, proliferation, differentiation, and viability (De León, Pupovac, & McArthur, 2020).

To date, the gold standard techniques of monitoring 3D culture models are end-point histology and fluorescence microscopy (Dmitriev, 2017), while requiring physical destruction of the cultured samples by sectioning and staining. Indirect and non-invasive assessment of cell culture via measuring other parameters of cell health is more attractive and has been extens-

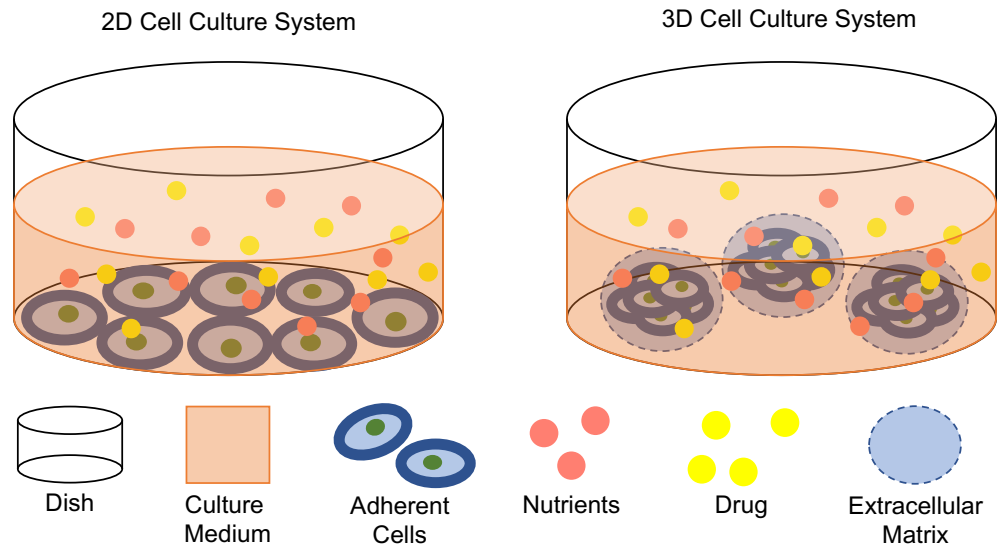


Figure 2.2: Comparison of 2D and 3D cell culture systems.

ively investigated for 2D cell cultures. Bavli et al. (2016) and Mahfouzi, Amoabediny, Doryab, Safiabadi-Tali, and Ghanei (2018) provided effective 2D spatial resolution by measuring oxygen, glucose, and lactate concentrations. These approaches are limited by the molecule diffusion into the culture media, which is unsuitable for 3D cell culture systems. Alternatively, physiological, morphological, and pathological conditions of cells can be determined by characterizing electrical properties of cells in culture (K'Owino & Sadik, 2005; Miklavčič, Pavšelj, & Hart, 2006). Trans-epithelial electrical resistance (TEER) measurements (S. Chen, Einspanier, & Schoen, 2015) allowed real-time monitoring based on the characterization of electrical properties of cells but only at single frequency. In contrast, electrical impedance spectroscopy (EIS) (Benson, Cramer, & Galla, 2013) is a well-established tool enabling frequency sweeping to capture frequency-dependent electrical characteristics of cell cultures. Migrating from 2D to 3D environment, the EIS system has been integrated with external electrodes either horizontally (Lei, Liu, & Tsang, 2018) or in parallel (Del Agua et al., 2018; Groeber et al., 2015; Pan et al., 2019). These early studies of 3D applications demonstrated the impedance spectrum of 3D cells and the correlation of impedance changes with cell number. However, integrating electrodes with 3D cell culture systems while preserving the functionality of cells remains very challenging.

Based on impedance spectroscopy studies, bioimpedance tomography targets imaging 3D culture processes with high spatial resolution. Obtaining the spatial resolution within 3D cell cultures is of great interest to efficiently identify the number, shape, and location of cells over time to distinguish cell metabolism and health status in different areas of the tissue. Bioimpedance tomography is an emerging promising technique that measures bioimpedance to image cells and accordingly infers the physical properties of cells, such as the physiological

status, shape, location, and dynamic response to regenerative medicines. Recent years have witnessed the explosive research of EIT in cell culture imaging (Y. Yang et al., 2016, 2019), cell-drug response imaging (H. Wu, Yang, et al., 2018), cell growth and viability assessment (H. Wu, Zhou, Yang, Jia, & Bagnaninchi, 2018), monitoring of single cell mitosis (X. Li, Yang, He, & Rubinsky, 2019), and tissue electroporation imaging (Davalos, Otten, Mir, & Rubinsky, 2004). EIT has exhibited great potential in providing information regarding the morphological and functional behavior of the cell cultures in a real-time and non-invasive manner.

The first EIT system was developed in 1978 (Henderson & Webster, 1978), while the Sheffield Mk1 was the first EIT system specially designed for biomedical purposes (Brown & Seagar, 1987). With the developments of micro technologies (Griffiths, Tucker, Sage, & Herrenden-Harker, 1996; Linderholm, Maescot, Loke, & Renaud, 2007; Rahman et al., 2008), instrumentation miniaturization of EIT has become prevailing by deploying a set of microelectrodes inside the cell culture environment. In other words, the feasibility of system fabrication at the cellular level allows EIT to accommodate the needs of 3D cell culture monitoring. E. J. Lee et al. (2014) proposed a KHU Mark2 micro-EIT system which placed a large number of electrodes on parallel walls to obtain large data points with the intention of high image resolution but was not yet examined with cells. Instead, Yin, Wu, Jia, and Yang (2018) employed 17 circular microelectrodes radially distributed at the bottom of the well while Y. Yang et al. (2016) placed 16 rectangular microelectrodes surrounding the substrate of the cylindrical chamber. This deployment enabled the authors to image human breast cancer cell spheroids (Y. Yang et al., 2016) and to characterize cell viability in the Triton X-100 solution (H. Wu, Yang, et al., 2018). The data acquisition speed of Yang's work can be up to 546 fps in serial mode and 1014 fps in semi-parallel mode (Y. Yang & Jia, 2017b). The spatial resolution that EIT can typically achieve is around 10% of the diameter of the sensing region (Metherall, Barber, Smallwood, & Brown, 1996).

These studies have demonstrated a prospective use for EIT in 3D cell culture monitoring. One challenge is the trend of sensor micro-miniaturization in cell imaging (H. Wu, Yang, et al., 2018; Y. Yang et al., 2016, 2019) has led to much weaker measurement signals and increased sensitivity to sensor imperfection, which requires improving spatial resolution and obtaining robust, high-quality image reconstruction. The other challenge is the need to process large amounts of sensing data sequences in real-time for cell imaging, suggesting that high computational efficiency is preferable.

2.3 EIT Image Reconstruction Algorithms

In tissue engineering, imaging 3D cell culture with spatial resolution at the cellular level (ideally $\sim 50\mu m$ (De León et al., 2020)) is of great interest to efficiently identify the number, shape and location of cells over time and to determine cell metabolism and health status. EIT is an emerging imaging technique that can potentially obtain better spatial resolution of 3D tissue cultures. As a typical inverse problem, the image reconstruction of EIT, in essence, suffers from nonlinearity, under-determination and ill-posedness. The development of EIT image reconstruction algorithms has been extensively investigated in terms of spatial resolution, noise resistance performance and computational efficiency to facilitate high image quality. Most EIT image reconstruction algorithms have been recently summarised by Chitturi and Farrukh (2017); M. Zhang, Ma, Huang, and Ge (2022); Zong, Wang, and Wei (2020). This section briefly reviews recent progress for EIT image reconstruction algorithms from the perspectives of model-based, learning-based/data-driven methods and recent challenges in tissue engineering.

2.3.1 Model-based Methods

Model-based methods refer to techniques that model the physical processes of the underlying problem and capture prior domain knowledge. Conventional model-based reconstruction approaches are partitioned into one-step, iterative, stochastic, and nonlinear methods.

One-step method

One-step reconstruction is constructed based on the idealized mathematical inversion of the forward model. This type of reconstruction algorithms is suitable for real-time imaging due to its fast running speed. As a universal method, Tikhonov regularization (Lukaschewitsch, Maass, & Pidcock, 2003) promotes smoothness of solutions with l_2 norm as the quadratic penalty, i.e. $\mathcal{R}(\Delta\sigma) = \|\Delta\sigma\|^2$. The EIT image reconstruction problem in (2.9) can then be formulated as an analytical expression:

$$\Delta\sigma = (\mathbf{J}^T\mathbf{J} + \lambda\mathbf{I})^{-1}\mathbf{J}^T\Delta\mathbf{V} \quad (2.10)$$

where \mathbf{I} is the identity matrix. Another common method GREIT (A. Adler et al., 2009) adopts the one-step Gauss-Newton solver with the Laplacian filter \mathbf{L} :

$$\Delta\sigma = (\mathbf{J}^T\mathbf{J} + \lambda\mathbf{L}^T\mathbf{L})^{-1}\mathbf{J}^T\Delta\mathbf{V} \quad (2.11)$$

However, the one-step method usually performs poorly in practice, resulting in image blurriness and artefacts. The main reason is that the sensor data easily deviate from what the analytic expression of the mathematical model would predict. Typically, one-step reconstruction serves as an initial guess for more advanced reconstruction algorithms, e.g., the adaptive group sparsity (AGS) (Y. Yang & Jia, 2017a; Y. Yang, Wu, & Jia, 2017).

Iterative method

The iterative reconstruction method is more reliable than one-step reconstruction. First, it combines the numerical forward model with a feedback loop, which enables strong noise robustness and artifact reduction. Second, it allows for introducing external prior knowledge as additional constraints \mathcal{R} to further enrich the sensor data information and enhance the ultimate reconstruction quality. Different choices of \mathcal{R} result in different patterns. Third, the iterative method is an alternate solution for cases where closed-form solutions are intractable. Optimizations of iterative algorithms can be solved by iterative Landweber method (Jang, Lee, Kim, & Choi, 2006), conjugate gradient algorithms (Wei, Liu, & Chen, 2019), alternating direction method of multipliers (ADMM) optimization algorithm (Fukushima, 1992; J. Wang, Huang, Zhang, & Wang, 2020), Gauss-Newton method (K. Zhang, Li, Yang, Xu, & Abubakar, 2019), and iterative shrinkage and thresholding algorithm (ISTA) (Gehre et al., 2012).

Total variation (TV) regularisation (Borsic, Graham, Adler, & Lionheart, 2009; González, Kolehmainen, & Seppänen, 2017; Zhou et al., 2015) is a widely used regularisation method for EIT reconstruction, which is especially suitable for conductivity distributions with a sharp boundary for the inclusions:

$$\mathcal{R}(\Delta\sigma) = \sum_{(i,j) \in \Omega} \sqrt{|\Delta\sigma_{(i+1,j)} - \Delta\sigma_{(i,j)}|^2 + |\Delta\sigma_{(i,j+1)} - \Delta\sigma_{(i,j)}|^2} \quad (2.12)$$

where (i, j) donates pixel index inside Ω . l_1 (or sparsity) regularization offers monadic penalties to promote sparsity or discontinuity (Gehre et al., 2012; Jin, Khan, & Maass, 2012; Tehrani et al., 2012), which is defined by:

$$\mathcal{R}(\Delta\sigma) = \sum_k |\langle \Delta\sigma, \phi_k \rangle| \quad (2.13)$$

where $\{\phi_k\}$ a basis/overcomplete frame/dictionary. This is suitable for circumstances where objects are naturally sparse inside the sensing region as prior knowledge, which is capable of suppressing pixels belonging to the background very close to zero and promoting nonzero pixels belonging to the targeted objects. Furthermore, group sparsity regularization (Y. Yang & Jia, 2017a) and its advanced version (Y. Yang et al., 2017) extended the concept of sparsity via pixel grouping to construct the underlying structure of the solutions. Assuming the conductivity change $\Delta\sigma$ can be classified into S_N groups, group sparsity regularization can be formulated

as

$$\mathcal{R}(\Delta\boldsymbol{\sigma}) = \|\Delta\boldsymbol{\sigma}\|_{2,1} = \sum_{i=1}^N \|\Delta\boldsymbol{\sigma}_{S_i}\|^2 \quad (2.14)$$

where $\|\cdot\|_{2,1}$ denotes the $l_{2,1}$ norm, which is the sum of energy of each defined group. These works demonstrated that the adoption of the group sparsity could potentially facilitate cancer cell spheroid imaging and tissue culture monitoring in biomedical applications. K. Zhang et al. (2019) utilized the multiplicative regularization (MR) algorithm to sharpen blurred edges. This smoothing regularization is based on the weighted l_2 norm with edge-preserving characteristics as follows:

$$\begin{aligned} \mathcal{R}_i(\Delta\boldsymbol{\sigma}) &= \frac{1}{v} \int_{\Omega} b_{i-1} (|\nabla\Delta\boldsymbol{\sigma}|^2 + \delta_{i-1}) d\mathbf{r}, \\ b_{i-1} &= \frac{1}{|\nabla\Delta\boldsymbol{\sigma}_{i-1}|^2 + \delta_{i-1}}, \\ \delta_{i-1} &= \frac{\|\Delta\mathbf{V} - \mathbf{J}\Delta\boldsymbol{\sigma}_{i-1}\|^2}{\|\Delta\mathbf{V}\|^2} \cdot \frac{1}{\tilde{\Delta}}, \end{aligned} \quad (2.15)$$

where i is the iteration index, v is the volume of Ω , b_i is the weighted for l_2 norm, $\tilde{\Delta}$ is a positive parameter related to the mesh size, and δ_i is a positive parameter to control the strength of regularization. In this regularization scheme, the dynamic regularization weight alleviates the complexity of parameter fine-tuning.

Stochastic method

The stochastic method solves the inverse problem in (2.9) from the statistical perspective. The above methods make estimations on $\Delta\boldsymbol{\sigma}$ deterministically, whereas this method regards $\Delta\boldsymbol{\sigma}$ as a random variable. It allows quantification of the uncertainty in the reconstruction to enhance robustness to data disturbance. Mathematically, it incorporates the Bayesian framework by implementing maximum a *posteriori* (MAP):

$$\operatorname{argmax}_{\Delta\boldsymbol{\sigma}} p(\Delta\boldsymbol{\sigma}|\Delta\mathbf{V}) \stackrel{\Delta}{=} \operatorname{argmin}_{\Delta\boldsymbol{\sigma}} [-\log p(\Delta\mathbf{V}|\Delta\boldsymbol{\sigma}) - \lambda \log p(\Delta\boldsymbol{\sigma}; \boldsymbol{\theta})] \quad (2.16)$$

where the parametric prior probability $p(\Delta\boldsymbol{\sigma}; \boldsymbol{\theta})$ introduces the prior knowledge, e.g. Gaussian distribution, which has the same function as $\mathcal{R}(\Delta\boldsymbol{\sigma})$; the likelihood $p(\Delta\mathbf{V}|\Delta\boldsymbol{\sigma})$ amounts to the data fidelity term in (2.9), which encapsulates the physics process to generate the measurement $\Delta\mathbf{V}$; the posterior probability $p(\Delta\boldsymbol{\sigma}|\Delta\mathbf{V})$ provides a distribution of all possible solutions for reconstruction.

For EIT imaging, structure-aware sparse Bayesian learning (SA-SBL) (S. Liu et al., 2018) and its 3D version (S. Liu et al., 2019) were proposed to promote clustered sparsity constraint from the statistical perspective. This Bayesian framework achieved promising results when extended to frequency-difference EIT (fdEIT) within the multiple measurement vector (MMV) models (S. Liu, Huang, Wu, Tan, & Jia, 2020). Generally, they considered $\Delta\boldsymbol{\sigma}$ as a set of

clusters with an equal size h and the clusters were allowed to overlap. The clustering partition is embedded with a matrix Ψ so that $\Delta\sigma$ is factorized by:

$$\Delta\sigma \triangleq \Psi \mathbf{x} \triangleq [\Psi_1, \dots, \Psi_g] [\mathbf{x}_1^T, \dots, \mathbf{x}_g^T]^T \quad (2.17)$$

where $g = n - h + 1$ donates the total number of possible clusters. $\forall i = 1, \dots, g$, $\Psi_i \triangleq [\mathbf{0}_{(i-1) \times h}^T, \mathbf{I}_{h \times h}^T, \mathbf{0}_{(n-i-h+1) \times h}^T]^T \in \mathbb{R}^{n \times h}$ donates the i -th cluster structure, and $\mathbf{x}_i = [x_i, \dots, x_{i+h-1}]^T \in \mathbb{R}^{h \times 1}$ denotes weights of each cluster. The linearized EIT model in (2.7) incorporates structure sparsity by:

$$\Delta \mathbf{V} = \mathbf{J} \Psi \mathbf{x} + \mathbf{e} \triangleq \Phi \mathbf{x} + \mathbf{e} \quad (2.18)$$

where $\Phi = \mathbf{J} \Psi \triangleq [\Phi_1, \dots, \Phi_g]$, $\Phi_i \triangleq \mathbf{J} \Psi_i \in \mathbb{R}^{m \times h}$, and the noise vector \mathbf{e} is subject to multivariate Gaussian distribution, i.e. $\mathbf{e} \sim \mathcal{N}(\mathbf{0}, \alpha \mathbf{I})$. The prior of \mathbf{x} is assumed to follow a zero-mean Gaussian distribution:

$$p(\mathbf{x}; \{\theta_i\}_{i=1}^g) = \mathcal{N}(\mathbf{0}, \Sigma_0) \quad (2.19)$$

where the covariance matrix $\Sigma_0 \in \mathbb{R}^{gh \times gh}$ is designed as a cluster diagonal matrix. The optimal clustering strategy was learned by sparse Bayesian learning (SBL). This method exhibited strong noise resistance performance.

However, these approaches may not be suitable for real-time monitoring where computation efficiency is a crucial criterion. In addition, they are based on the linearized EIT model and sparsity assumption, making it challenging to accurately estimate conductivity values and deal with non-sparse cases.

Nonlinear method

In the above methods, the approximated linearization of the EIT model incurs model errors, limiting the reconstruction quality. Error is inevitable when interpreting conductivity levels based on the sensitivity matrix \mathbf{J} from the measurement data. To mitigate this issue, the non-linear reconstruction algorithm opens a new research area to improve image quality by modelling the non-linear EIT problem.

The D-bar method as a classical non-linear method was proposed for solving EIT image reconstruction (Knudsen, Lassas, Mueller, & Siltanen, 2007, 2009; Watenig & Fox, 2009). It provides non-iterative/real-time absolute reconstruction by firstly applying the nonlinear Fourier transform to the boundary measurement in the form of Neumann-to-Dirichlet (ND) map Λ_σ :

$$\mathbf{t}^{exp}(k) = \int_{\partial\Omega} e^{ik\bar{z}} (\Lambda_\sigma - \Lambda_1) e^{ikz} ds(z), \text{ for } k \in \mathbb{C}, 0 < |k| \leq R \quad (2.20)$$

where Λ_1 the ND map of the homogeneous conductivity 1, $ds(z)$ denotes arclength measure on $\partial\Omega$, $\mathbf{t}^{exp}(k)$ is the generated scattering data, and R is the chosen radius. Secondly, $\mathbf{t}^{exp}(k)$ is then used to solve the low-pass D-bar equation. This equation directly recovers the absolute conductivity distribution σ , which is defined as:

$$\begin{aligned}\sigma^{exp}(z) &= [\mu^{exp}(z, 0)]^2, \text{ for } z \in \Omega \\ \mu^{exp}(z, k) &= 1 + \frac{1}{4\pi^2} \int_{\partial\Omega} \frac{\mathbf{t}^{exp}(k')}{(k-k')\bar{k}'} e(z, -k') \overline{\mu^{exp}(z, k')} dk'_1 dk'_2,\end{aligned}\tag{2.21}$$

where $e(z, k) := \exp(i(kz + \bar{k}\bar{z}))$ is a unitary multiplier. The robustness of the D-bar algorithm to incorrect electrode locations and boundary shape was explicitly proven (Hamilton, Mueller, & Santos, 2018). The D-bar method with EIT was further validated in pediatric cystic fibrosis (CF) patients for lung function assessment (Muller et al., 2018). Despite these advances, the existence and uniqueness of the D-bar solution were proven for only two-dimensional inverse problem by Nachman (1996). In addition, the D-bar method suffers from images' degraded sharpness, which is an important feature in medical imaging.

In the context of difference imaging, (D. Liu, Kolehmainen, Siltanen, & Seppänen, 2015) proposed a nonlinear approach by simultaneously reconstructing both the initial state of the conductivity distribution σ_1 and the conductivity change $\Delta\sigma$. The nonlinear model in (2.6) was reformulated as:

$$\begin{bmatrix} \mathbf{V}_1 \\ \mathbf{V}_2 \end{bmatrix} = \begin{bmatrix} F_{FEM}(\sigma_1) \\ F_{FEM}(\sigma_1 + \Delta\sigma) \end{bmatrix} + \begin{bmatrix} \mathbf{e}_1 \\ \mathbf{e}_2 \end{bmatrix}\tag{2.22}$$

where \mathbf{V}_1 and \mathbf{V}_2 donate voltage data measured at the initial state and after conductivity change, respectively; $F_{FEM}(\cdot)$ donates discretized forward mapping based on finite element method (FEM). The final estimate was obtained by minimizing regularized least squares formalism with independent regularization design for σ_1 and $\Delta\sigma$. This work demonstrated the robustness of difference imaging in the presence of modelling errors. Based on this nonlinear method, Khambampati, Liu, Konki, and Kim (2018) further proposed to automatically restrict $\Delta\sigma$ to a subdomain. However, their optimization with the iterative Gauss–Newton method suffers from heavy computational costs.

Table 2.1 comprehensively compares representative model-based methods. Despite the successive advancement of these advancing algorithms based on either mathematical or physical models, real-time 3D cell culture imaging with the miniature EIT system requires further improvements in terms of computational efficiency, spatial resolution at the miniaturised scale, and noise resistance performance.

Table 2.1: Comparison of representative model-based methods for EIT image reconstruction.

Method type	Reference	Algorithm	Regularization	Optimization	Characteristics
One-step	Lukaschewitsch et al. (2003)	Tikhonov	l_2 norm	-	Smoothness; real-time; geophysical imaging
	A. Adler et al. (2009)	GREIT	Laplacian filter	One step Gauss-Newton	Small position error; small ringing artefacts; real-time; lung imaging
Iterative	Tehrani et al. (2012)	Sparsity	l_1 constraint	ISTA	Sparsity; sharp edge; discontinuity
	Zhou et al. (2015)	Total variation	TV	Gauss-Newton	Sharp edge; discontinuity; blocky images
	Y. Yang and Jia (2017a)	AGS	Group sparsity	ADMM	Dynamic pixel grouping; cell spheroid imaging
	K. Zhang et al. (2019)	MR	Weighted l_2 norm	Gauss-Newton	Edge-preserving; reduced complexity of parameter fine-tuning; thorax imaging
Stochastic	S. Liu et al. (2018)	SA-SBL	Prior	MAP estimation	Structured sparsity; automatic structure clustering; higher spatial resolution and anti-noise performance
Nonlinear	D. Liu et al. (2015)	nonlinear difference reconstruction	l_2 norm, TV	Gauss-Newton	FEM approximation; robustness to modeling errors; difference imaging
	Hamilton et al. (2018)	D-bar	-	-	Nonlinear inversion; real-time; robustness to modeling errors; absolute imaging

2.3.2 Learning-based Methods

Conventional algorithms require manually determining regularization terms and fine-tuning hyper-parameters, such as penalty parameters and step sizes. In addition, the computational cost is considerable, preventing their wide adoption in biomedical applications that desire real-time imaging capability. Moreover, more advanced image reconstruction algorithms need to be studied to achieve a spatial resolution of reconstructed images that is appropriate for high-quality measurements.

Recent years have witnessed the revolution of deep learning, which can offer superior image quality and fast inference time. Instead of handcrafting prior knowledge in conventional iterative approaches, deep learning has proven its effectiveness and efficiency in automatically learning information from big data set. Encouraged by the unprecedented success of deep learning in the computer vision domain, medical tomographic image reconstruction is a new frontier of machine learning with noteworthy improvement in image quality and speed (G. Wang et al., 2020). In the context of EIT imaging, learning-based methods are also desirable for real-time imaging due to the faster execution time against the above conventional algorithms. These methods typically take advantage of a deep network $f_{\boldsymbol{\theta}}(\cdot)$ parameterised by network weights $\boldsymbol{\theta}$ to reconstruct the conductivity distribution based on the measurement input. Optimal $\boldsymbol{\theta}^*$ are determined based on training data \mathcal{D} of measurements and corresponding ground-truth conductivity distributions, $\{(\Delta\mathbf{V}^{(k)}, \Delta\boldsymbol{\sigma}_{gt}^{(k)})\}_{k=1}^K$. Then the image reconstruction problem is converted to a regression problem by minimising an objective function \mathcal{L} (here, Mean Squared Error is taken as an example):

$$\min_{\boldsymbol{\theta}} \mathcal{L}(\boldsymbol{\theta}; \mathcal{D}) := \frac{1}{2} \sum_{(\Delta\mathbf{V}, \Delta\boldsymbol{\sigma}_{gt}) \in \mathcal{D}} \|\Delta\boldsymbol{\sigma}_{gt} - f_{\boldsymbol{\theta}}(\Delta\mathbf{V})\|^2 + r(\boldsymbol{\theta}). \quad (2.23)$$

where r is the regularization term to avoid overfitting. Once the training procedure is finished, the execution of $f_{\boldsymbol{\theta}^*}(\cdot)$ is fast for reconstruction.

Existing learning-based EIT image reconstruction algorithms can be classified into three categories (Z. Chen, Xiang, Bagnaninchi, & Yang, 2022; Xiang, Dong, & Yang, 2021): (a) fully learning approaches that directly map measurement data to a conductivity image; (b) image post-processing approaches that employ a trained network to eliminate artifacts of a preliminary conductivity image obtained from model-based algorithms; (c) model-based deep learning approaches that unroll a finite number of iterations of the model-based methods into a network.

Fully Learning Approach

Empowered by big data, fully learning approaches directly learn the mapping from measurement data to the conductivity image via a neural network typically constructed by a sequence of convolutional layers, Multilayer Perceptron (MLP), and activation layers (Z. Chen et al., 2020; F. Li, Tan, & Dong, 2020; Tan et al., 2018). Rather than relying on the mathematical or physical model, these approaches are purely data-driven. Fig. 2.3 illustrates a typical deep network architecture for image reconstruction. MLP (Rumelhart, Hinton, & Williams, 1986) was the top choice to construct a neural network and its working mechanism is depicted in Fig. 2.3(c). The output neurons of the l^{th} hidden layer, i.e. $h_i^{(l)}$, are fully connected to every neuron in the previous layer, i.e. $h_j^{(l-1)}$. The analytic expression is formulated as:

$$h_i^{(l)} = \gamma\left(\sum_j W_{ij}^{(l)} h_j^{(l-1)} + b_i^{(l)}\right) \quad (2.24)$$

where $W_{ij}^{(l)}$ denotes the unit weight connecting the j^{th} neuron in layer $l - 1$ with the i^{th} neuron in layer l ; $b_i^{(l)}$ is the bias for the i^{th} neuron in layer l ; and γ is the non-linear activation function. Common choices of activation function γ for nonlinear operations can be the logistic function, rectified linear units, and the hyperbolic tangent function. The weights and biases construct the trainable network parameters θ that are learned during training in (2.23) (see Fig. 2.3(b)).

The linear operations by MLPs acquire massive parameter dimensionality and limit the depth of neural networks, which motivated the development of convolutional neural networks (CNNs) (Krizhevsky, Sutskever, & Hinton, 2017; LeCun, Bottou, Bengio, & Haffner, 1998). In CNNs, sparse connections successfully release heavy computation of MLPs by sharing weights across different spatial locations (see Fig. 2.3(d)).

A surge of efforts has introduced various CNNs to the field of electrical tomography and exhibited remarkable performance in tomographic imaging. Zheng et al. (2018) employed an auto-encoder structure where the encoder mimics the forward problem and the subsequent decoder solves the inverse problem of electrical capacitance tomography (ECT). Tan et al. (2018) alternatively developed a deep network taking the well-established architecture in computer vision, i.e. LeNet (LeCun et al., 1998) for electrical resistance tomography (ERT). Dedicated to EIT, Hu, Lu, and Yang (2019) took into account the geometrical structure of EIT sensors and introduced a CNN to map directly the measurement data to conductivity distribution. Z. Chen et al. (2020) proposed a novel deep network FC-UNet for cell imaging. The design of FC-UNet mimics the behavior of the human brain by taking steps to make predictions.

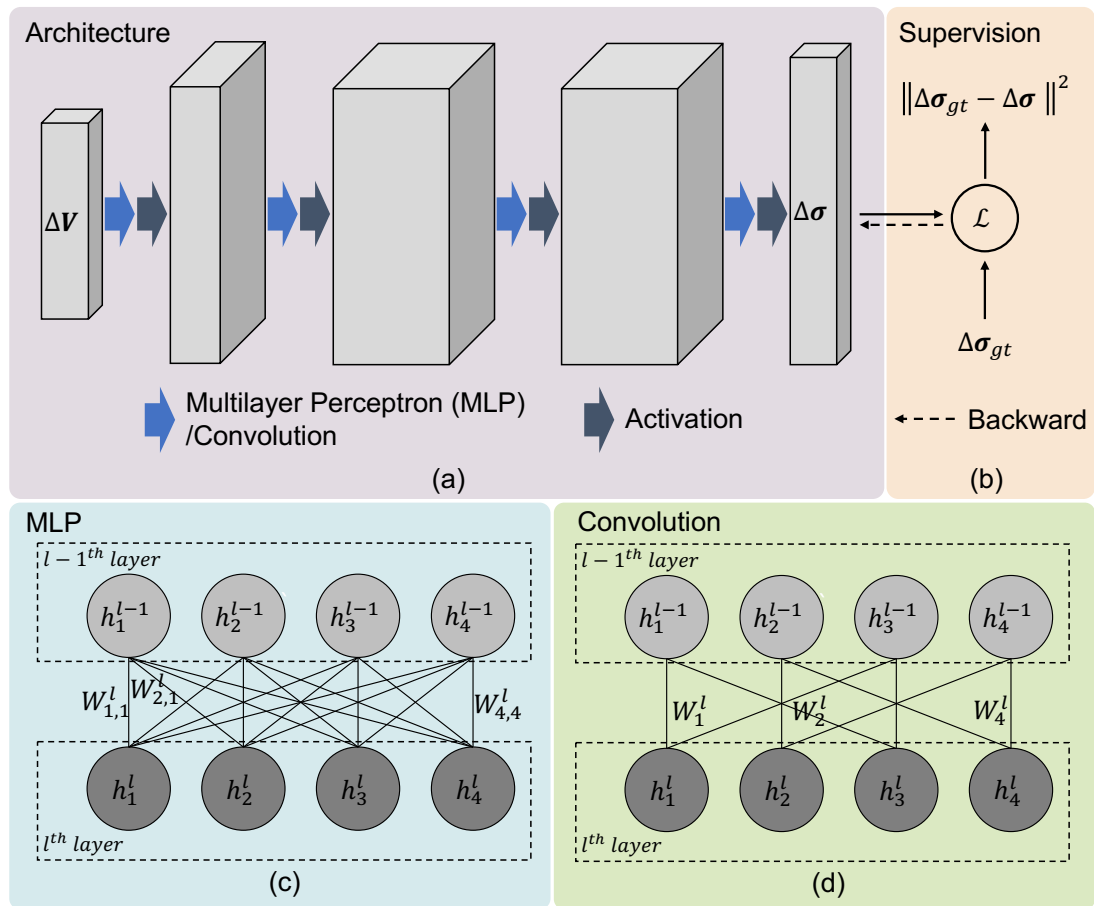


Figure 2.3: (a) An illustration of a typical deep architecture for image reconstruction. (b) Supervision strategy with mean squared error (MSE) as the objective function for training. (c) Multilayer Perceptron (MLP): neurons are fully connected at each layer. (d) Convolution: neurons are sparsely connected and restricted to local neighbours.

These fully learning-based methods utilize data domain learning structure and demonstrate the superiority of deep learning methods over conventional image reconstruction methods in identifying each object's position and geographical shape within the sensing region. A significant limitation of these early-stage studies is that only single-level (or binary) conductivity/permittivity changes are investigated, which is far from the practical cell culture systems with multi-level conductivity/permittivity distributions.

Another critical concern over the practical deployment of fully learning-based methods is the black-box nature. End-to-end training of deep networks is the lack of interpretability and the underlying structures neglect the physical processes of the inverse problem. Furthermore, such blind reconstruction tools highly depend on the quality and diversity of training data, which to some extent, degrades the generalization ability, especially in biomedical engineering.

Image Post-processing Approach

Instead of entirely ignoring the physical insights, image post-processing approaches start from the preliminary conductivity images generated by the mathematical inversion/iterative algorithms/nonlinear reconstructions (see Fig. 2.4). To eliminate the inevitable artefacts of the initial reconstructions, different deep networks are picked and trained as a post-processing step for denoising (Duan, Taurand, & Soleimani, 2019; Hamilton et al., 2018; Wei et al., 2019).

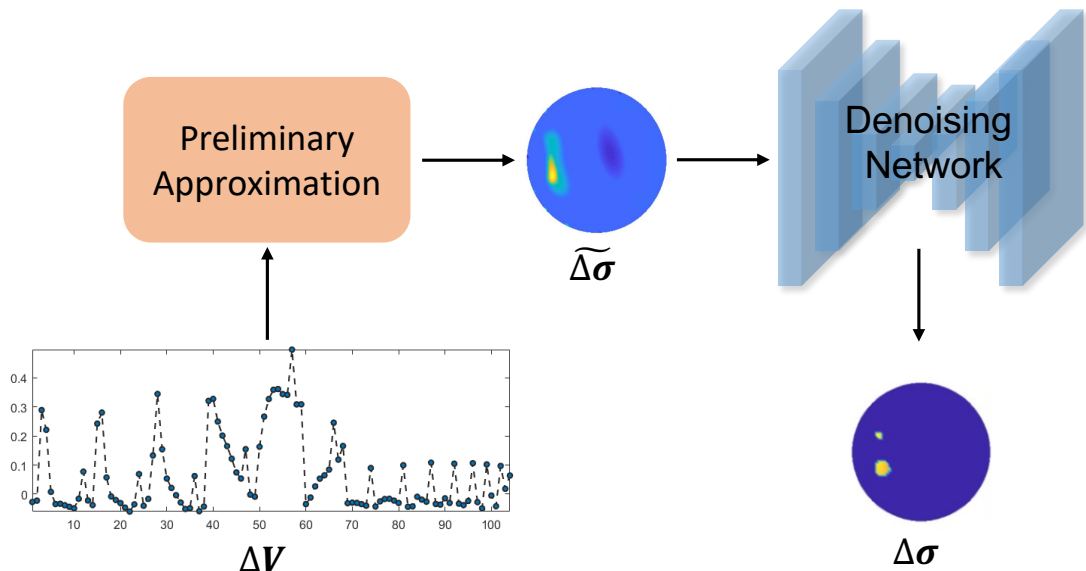


Figure 2.4: The generic pipeline of image post-processing approaches.

Similar to fully learning approaches, image post-processing took advantage of the availability of well-established deep-learning models in computer vision. Among all learning models, the UNet which was first proposed especially for biomedical image segmentation (Ronneberger, Fischer, & Brox, 2015) has become the most popular and indispensable denoising tool in EIT imaging. Fig. 2.5 illustrates an example of the UNet architecture. The main idea of UNet is to map an image to a latent vector and then reconstruct it back to an image. The contraction on the left-hand side applies two convolutional layers with a max pooling in each step whereas the layer at the bottom employs a upsample layer after convolutions. During expansion on the right-hand side, the corresponding feature maps from the contraction part are reused to reduce the distortion of images. They are appended directly after the upsampling layer. After the two-convolution operation for the last step, a 1×1 convolutional layer and a sigmoid layer are used for classification.

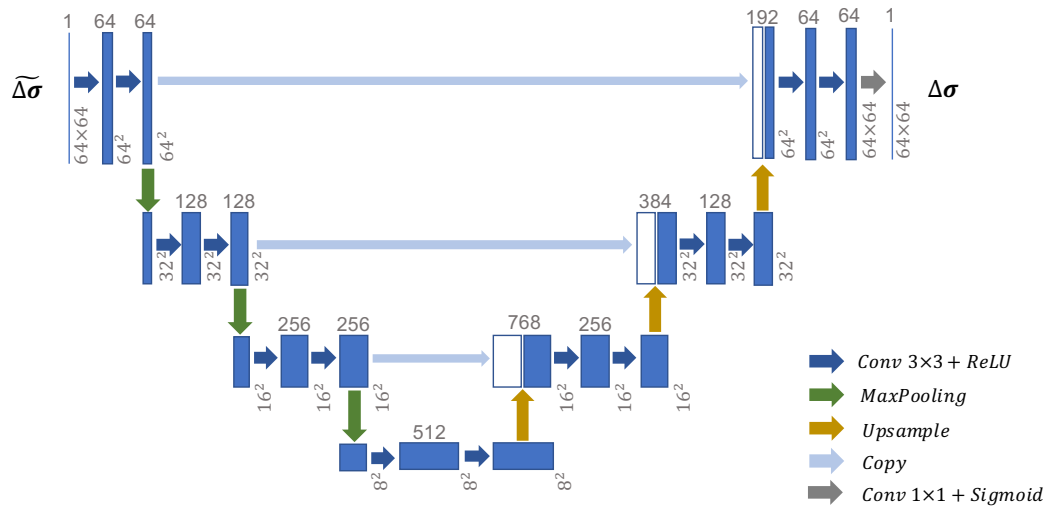


Figure 2.5: The network architecture of UNet.

For EIT imaging, the work in (Duan et al., 2019) adopted the UNet architecture to remove aliasing artefacts from the TV results (Borsic et al., 2009). The network was trained using only hundreds of samples. Similarly, the deep D-Bar approach (Hamilton et al., 2018) and the dominant-current deep learning scheme (DC-DLS) (Wei et al., 2019) used the UNet to estimate the conductivity based on the approximated solution from different model-based methods. In the deep D-bar, the network input is calculated based on the D-bar method (Hamilton et al., 2018). Compared to the deep D-Bar approach, the DC-DLS is relatively time-consuming as an iterative algorithm derives the approximation.

Unfortunately, learning-based post-processing approaches still suffer from image blurring, especially when insufficient data is collected for training, e.g., clinical data. In addition, the quality of preliminary images may affect the ultimate reconstruction performance.

Model-based Deep Learning Approach

The main drawback of generic deep networks in fully learning and image post-processing approaches is the black box nature and the requirement of large-scale data acquisition. These shortages limit the deployment of learning-based methods in clinical utility, which motivates contributions of model-based deep learning approaches. Unrolling or unfolding approaches (Monga, Li, & Eldar, 2021) are emerging techniques that systematically incorporate deep neural networks with conventional iterative algorithms instead of relying entirely on big data or physics. The main idea of unrolling strategy is to unfold the iterative steps of conventional iterative algorithms into cascaded blocks of a deep network. The schematic illustration is provided in Fig. 2.6. The repetitive iteration step of iterative algorithms is interpreted as one network layer. A stack of this network layer forming a deep neural network is equivalent to executing the iteration multiple times. The network parameters are learned via backpropagation. Consequently, the trained network inherits prior structures and domain knowledge of the iterative algorithms and computational benefits of conventional deep networks.

The seminal work of Gregor and LeCun (2010) was the first algorithm unrolling approach to improve the computational efficiency of sparse coding. In this work, the ISTA was unrolled into a compact network LISTA. The trained LISTA was reported roughly 20 times faster than the original ISTA. In the past few years, growing unrolling approaches have been explored for diverse underlying iterative algorithms. For example, L. Zhang, Wang, and Giannakis (2019) unrolled an iterative prox-linear solver for power system state estimation. Y. Yang, Sun, Li, and Xu (2018) unrolled the widely adopted ADMM into a deep architecture ADMM-CSNet for compressed sensing. Parameters of the ADMM solver are learned via training to achieve faster speed while preserving reconstruction accuracy. For tomographic reconstruction, J. Adler and Öktem (2018) proposed an iterative CNN by unrolling the primal-dual hybrid gradient (PDHG) algorithm and replacing the proximal operator with learned operators. Xiang et al. (2021) unrolled the fast iterative shrinkage and thresholding algorithm (FISTA) into a deep network FISTA-Net. FISTA-Net demonstrated good generalization ability over conventional methods for two image reconstruction modalities, i.e. Electromagnetic Tomography (EMT) and sparse-view Computational Tomography (CT).

Unrolling approaches provide a novel way to interpretable deep neural networks and relieve heavy parameter requirements compared to the hierarchical architecture adopted by generic deep networks. However, the network architecture design of unrolling approaches is overly complicated, which results in less effective network training.

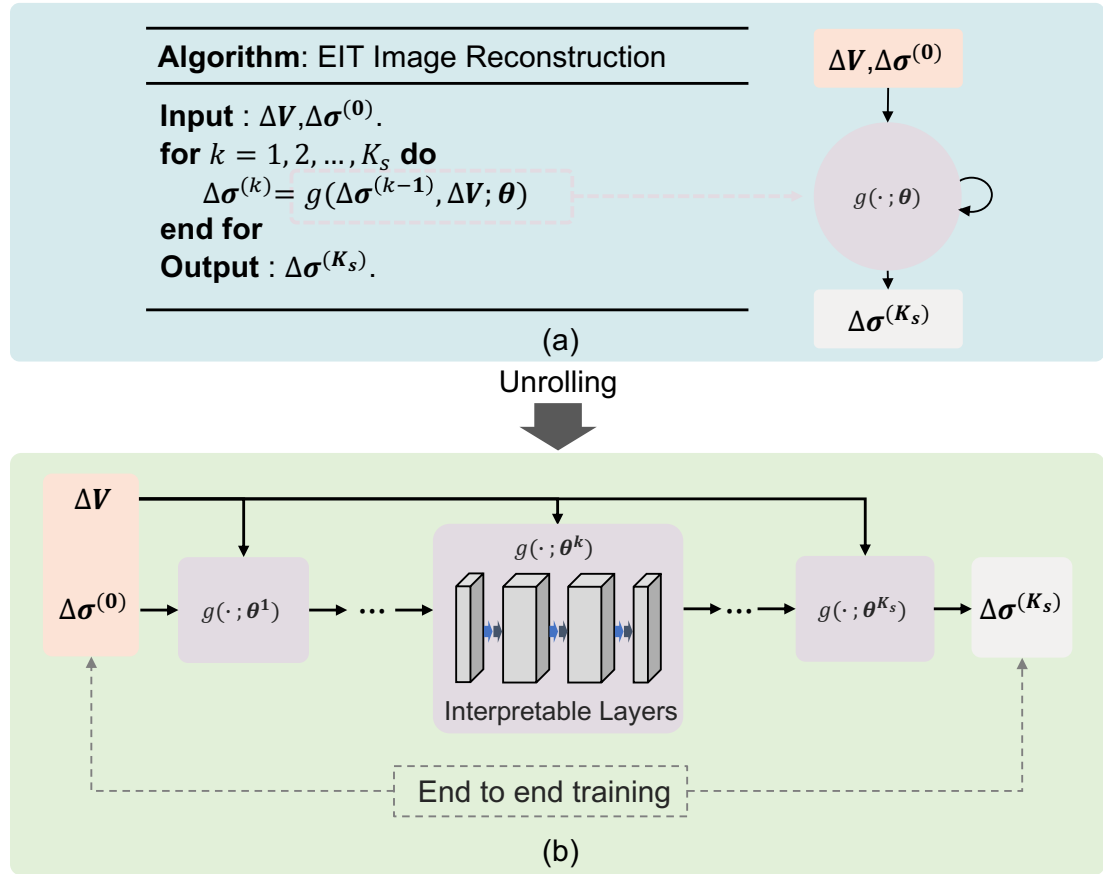


Figure 2.6: The general idea of model-based deep learning approach based on algorithm unrolling. Starting from an iterative algorithm, a deep network is generated by cascading the iterations $g(\cdot; \theta)$ of the iterative algorithm. Each iteration is mapped into a network layer parameterized by $\theta^k, k = 1, \dots, K_s$. Layer parameters can be shared across layers or layer-specific. Stacking K_s layers to construct a deep network is equivalent to executing the iterative algorithm with K_s iterations. Therefore, this network structure naturally inherits the interpretability from the physics of the iteration algorithm. The parameters $\{\theta^1, \theta^2, \dots, \theta^{K_s}\}$ are learned through end-to-end training. (a) An abstract iterative image reconstruction algorithm. (b) The corresponding unrolled deep network.

Table 2.2: Recent representative learning-based methods for electrical tomographic image reconstruction.

Methods	Year	Reference	Underlying network/algorithm	Image resolution	Computational speed (<i>ms</i>)	Application domain	Topics
Fully learning	2018	Zheng et al.	Auto-encoder	3228×1	-	Multiphase flow	ECT
	2018	Tan et al.	LeNet	812×1	7.8	Multiphase flow, biomedical monitoring, etc.	ERT
	2019	Hu et al.	CNN	64×64	-	Industrial process, cell culture imaging	EIT
	2020	F. Li et al.	V-Net	812×1	16.1	Multiphase flow	ERT
	2020	Z. Chen et al.	UNet	64×64	1.08	Cell culture imaging	EIT
	2021	Z. Chen et al.	Multimodal CNN	3228×1	1.82	Cell culture imaging	EIT
Image post-processing	2018	Hamilton et al.	UNet, D-Bar	64×64	7.65 (UNet only)	Medical imaging	EIT
	2019	Duan et al.	UNet, TV	50×50	-	Artificial skin	EIT
	2019	Wei et al.	UNet, bases-expansion subspace optimization	64×64	69×10^3	Medical imaging	EIT
	2022	X. Zhang et al.	VDD-Net, conjugate gradient algorithm	256×256	400	Medical imaging	EIT
Model-based deep learning	2021	Xiang et al.	CNN, ISTA	64×64	-	Biomedical imaging	EMT, CT
	2022	Z. Chen et al.	Self-attention, LSTM, ADMM	64×64	126	Biomedical imaging	Multifrequency EIT

Table 2.2 provides a brief overview of representative fully learning approaches, image post-processing approaches, and model-based deep learning approaches for tomographic image reconstruction applied in different domains over the past five years. The development of deep learning in the electrical tomography field is gradually increasing and enhancing industrial processes and biomedical imaging.

2.3.3 Recent Challenge in Tissue Engineering

Tissue engineering has achieved tremendous progress in aspects of renewable cell sources, advanced biomaterials for active modulation of cell growth, and 3D architecture technologies of tissue scaffolds (Khademhosseini & Langer, 2016). The recent challenge of tissue engineering lies in achieving biological functions of cellularized constructs and host compatibility, especially for clinical applications. Consequently, it is demanding to quantify cellular responses in-depth and over time in a label-free and non-invasive manner. End-point histology and fluorescence microscopy, which are current gold standard tools to monitor 3D culture models, are time-consuming and destructive despite offering high-resolution images.

In contrast, EIT is a potential solution for 3D cell culture monitoring with excellent properties of low-cost fabrication, non-invasiveness, portability, and fast speed. However, EIT intrinsically suffers from low spatial resolution due to the nature of nonlinear, ill-posed, and ill-conditioned image reconstruction problem and weak measurements. These long-standing challenges in image resolution have hindered the massive adoption of EIT as a standard tool in tissue engineering. As reported in De León et al. (2020), the ideal spatial resolution for 3D cell culture monitoring is $\sim 50\mu m$ to efficiently identify the cell metabolism and health status. The issues to be addressed urgently include high-resolution image reconstruction with preferable real-time performance and quantitative tomographic image analysis.

Table 2.3 compares the performance of conventional model-based reconstruction algorithms, and learning-based reconstruction methods in terms of accuracy, interpretability, generalizability, parameter dimensionality, and computational efficiency. Apparently, learning-based reconstruction methods exhibit more powerful performance in different aspects. Deep learning opens a new era of imaging research and translation. Therefore, the advancement of machine learning for EIT in tissue engineering has the potential to contribute to developing data-driven decisional tools in the field and thus ultimately generate significant clinical benefits for patients, transforming the healthcare practice into personalized, preventive and precision medicine.

Table 2.3: Comparison of model-based and learning-based image reconstruction algorithms.

Methods		Reconstruction accuracy	Interpretability	Generalizability	Parameter dimensionality	Computational efficiency
Model-based	One-step	Low				High
	Iterative	Middle	High	High	Low	Low
	Stochastic	Middle				Low
	Nonlinear	Low				High
Learning-based	Fully learning	High	Low	Low	High	High
	Image post-processing	High	Middle	Middle	High	Middle
	Model-based deep learning	High	High	Middle	Middle	High

2.4 Summary

This chapter provides a brief review of the foundation of EIT, a prospective use for EIT in tissue engineering, the state-of-the-art EIT image reconstruction algorithms, and the recent challenge in tissue engineering. The purpose of the chapter is to highlight the importance of deep learning to promote EIT as a gold standard technique for monitoring 3D culture models. The innovative work and scientific contribution of this thesis lies in hybrid learning-based cell imaging, structure-aware learning-based cell culture imaging, model-based learning algorithm for mfEIT image reconstruction and 3D imaging using point cloud network, which will be presented subsequently in the following chapters.

Cell Culture Imaging Using Hybrid Learning

3.1 Introduction

Rapid imaging of 3-D cell culture processes in a label-free, non-destructive manner is becoming increasingly attractive in tissue engineering, especially for drug discovery and long-term biological behavior monitoring. Cell imaging with EIT has been particularly challenging in solving the EIT-image-reconstruction problem. The trend of sensor micro-miniaturization in cell imaging (H. Wu, Yang, et al., 2018; Y. Yang et al., 2016, 2019) has led to much weaker measurement signals and increased sensitivity to sensor imperfection, which requires improving spatial resolution and obtaining robust, high-quality image reconstruction. In addition, the need to process large amounts of sensing data sequences in real-time for cell imaging suggests that high computational efficiency is preferable.

This chapter targets addressing the challenging multi-conductivity-level EIT image reconstruction problem that is frequently encountered in cell imaging. The main contribution lies in developing a novel Deep Neural Network (DNN) and physical model-based hybrid image reconstruction framework to recover multi-conductivity-level conductivity distributions effectively. As it is very challenging to estimate continuous, multi-level conductivity changes using a single neural network with limited training data, the problem is split into two sub-tasks, i.e. DNN based structural information estimation and physical model-based conductivity prediction. Some recent work (Hamilton et al., 2018; Wei et al., 2019) has demonstrated the success of combining DNN with the physical EIT model, where DNNs implement post-processing to remove artefacts of the initial low-quality images generated from the physical model-based reconstruction. Differently, the proposed framework first leverages DNN to predict binary structural information and then continuously determines the conductivity using regularization. A DNN named FC-UNet is established to identify binary structural information, i.e. position and geographical shape of each object within the sensing region. The structural information is then encoded into Group Sparsity (GS) regularization (Y. Yang & Jia, 2017a), an iterative

framework utilizing the structural information as constraint, to further estimate the conductivity levels of each object. The framework is named DL-GS and its effectiveness and superiority are verified based on phantom simulation and real-world data on MCF-7 breast cancer cell aggregates.

3.2 DL-GS: A Hybrid Learning Method for Cell Aggregate Imaging

3.2.1 DL-GS Framework

Fig. 3.1 presents the schematic illustration of the proposed DL-GS framework, where the input is boundary voltage measurement, and the output is conductivity change. We first construct a deep convolutional neural network to estimate the conductivity distribution with the input voltage measurement. This network distinguishes inclusions from background substances, and results are presented in a binary format. To train the network, we establish a training data set with multi-level conductivity distributions by finite element modelling with COMSOL Multiphysics (see details in Section 3.3.1). The binary result is then fed into a group index encoder, which generates a pixel grouping index vector depicting the underlying structural information of the conductivity (Y. Yang & Jia, 2017a). As prior knowledge, the structural information is finally integrated into GS regularization to estimate conductivity values in a continuous manner.

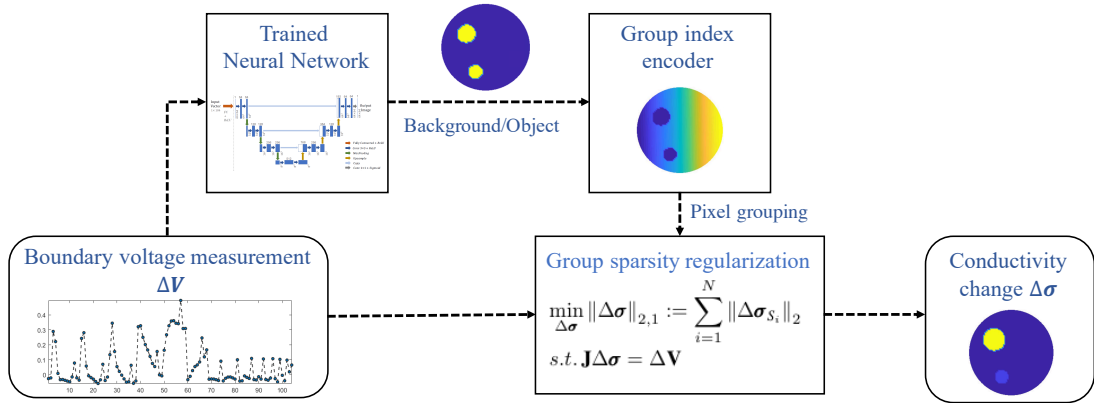


Figure 3.1: Schematic illustration of the proposed DL-GS framework.

Network Architecture

The objective of the neural network is to predict the positions and shapes of all possible objects, given the boundary voltage measurement. The neural network consists of a Fully Connected (FC) layer and a UNet (Ronneberger et al., 2015) (see Fig. 3.2); therefore, it is named as FC-UNet. In our previously reported Adaptive Group Sparsity (AGS) algorithm (Y. Yang & Jia, 2017a), the estimation of the positions and shapes of objects was achieved by a one-step Gauss-Newton solver with Laplacian regularization (Y. Yang, Jia, Polydorides, & McCann, 2014). This method is limited in that the results are coarse and sensitive to noise, which poses a challenge to accurately determining the boundary of objects. In contrast, the proposed FC-UNet is designed to enable faster and more accurate predictions.

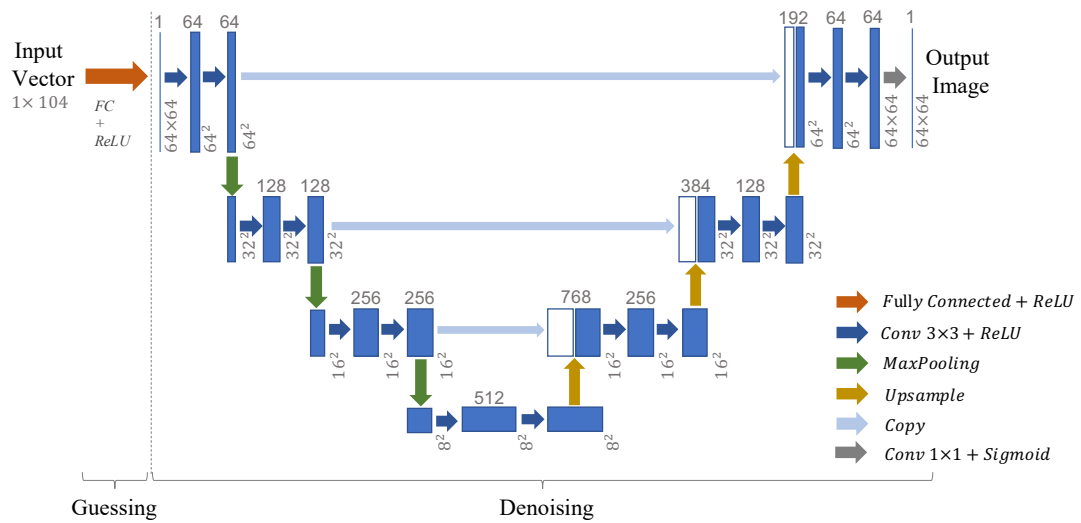


Figure 3.2: The architecture of FC-UNet.

As illustrated in Fig. 3.2, in FC-UNet, we first introduce an FC layer followed by a ReLU layer to implement an initial estimate of the conductivity distribution. A UNet-like architecture, which was proposed especially for biomedical image segmentation (Ronneberger et al., 2015), is employed afterwards to denoise the output of the FC layer. The main architecture of UNet is a typical auto-encoder, which maps an image to a low-dimension tensor and then reconstructs it back to an image. The contraction on the left-hand side comprises a stack of convolutional and max pooling layers. It applies two 3×3 convolutional layers with a 2×2 max pooling in each step, whereas the layer at the bottom employs a 2×2 upsample layer after convolutions. The expansion on the right-hand side is more or less symmetric to the contraction, using transposed convolutions to facilitate accurate localization. Skip connections are also inserted in expansion to capture tiny details and mitigate the vanishing gradient problem, where the corresponding feature maps from the contraction part are reused and concatenated in expansion steps. The feature maps are appended directly after the upsample layer. Finally, after the two-convolution operation, a 1×1 convolutional layer and a sigmoid layer are used for

classification. To choose a UNet structure well suited to EIT image reconstruction problems, we need to reduce hidden layers in the original architecture as a trade-off due to the considerable parameters for the FC layer at the beginning (i.e. 104×4096). After performing hyperparameter searching on the validation data set, we determine to have one less contraction step and one less expansion step.

Each pixel is eventually classified into either background or object. Then the binary mask $\mathbf{M} \in \mathbb{R}^n$ is given by the output, $\mathbf{M} = f_{FC-UNet}(\Delta\mathbf{V}|\boldsymbol{\theta})$, where $f_{FC-UNet}$ is the forward mapping of the FC-UNet parameterised by network weights $\boldsymbol{\theta}$. The network parameters $\boldsymbol{\theta}$ are learned during training. We use binary-cross-entropy as the loss function to train the FC-UNet:

$$\mathcal{L}(\boldsymbol{\theta}) = -\frac{1}{K} \sum_{i=1}^K (\mathbf{M}_i \cdot \log \hat{\mathbf{M}}_i + (1 - \mathbf{M}_i) \cdot \log(1 - \hat{\mathbf{M}}_i)) \quad (3.1)$$

where $\hat{\mathbf{M}}_i$ denotes the ground truth, and K is the total number of input-target pairs in the training data set.

Group Index Encoder

The group index encoder is to partition all pixels within the sensing region into different groups based on the structural information depicted by the binary mask \mathbf{M} from FC-UNet. Assuming the conductivity change $\Delta\boldsymbol{\sigma}$ can be classified into N groups, i.e.

$$\Delta\boldsymbol{\sigma} = \{\Delta\boldsymbol{\sigma}_{S_1}, \Delta\boldsymbol{\sigma}_{S_2}, \dots, \Delta\boldsymbol{\sigma}_{S_N}\} \quad (3.2)$$

where $S_i, i = 1, 2, \dots, N$ denotes the group index of the i^{th} group. The strategy of the group index encoder is (see Fig. 3.3 for schematic illustration):

1. pixel clusters classified as an object will be defined as a large group and assigned the same group index value; different objects correspond to different large groups; (the example in Fig. 3.3 has two large groups, i.e. $\Delta\boldsymbol{\sigma}_{S_1}, \Delta\boldsymbol{\sigma}_{S_2}$)
2. individual pixels classified as the background will be defined as a series of small groups; (Fig. 3.3 has $\Delta\boldsymbol{\sigma}_{S_3}, \dots, \Delta\boldsymbol{\sigma}_{S_N}$)
3. consecutive integers are assigned as group index for each group, i.e. $1, 2, \dots, N$;
4. the grouping follows $\bigcup_{i=1}^N \Delta\boldsymbol{\sigma}_{S_i} = \Delta\boldsymbol{\sigma}$.

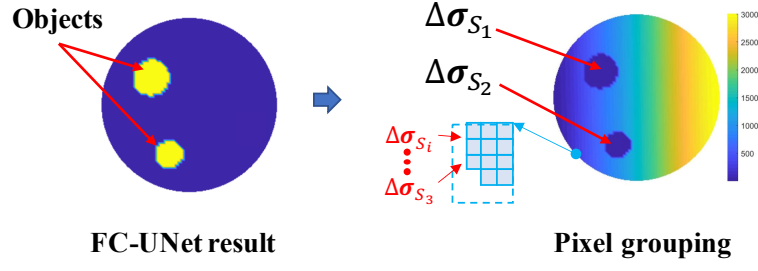


Figure 3.3: Pixel grouping based on FC-UNet result.

Group Sparsity Regularization

After obtaining the pixel grouping result, we impose this structural characteristic as a-priori information and estimate the continuous conductivity by using group sparsity regularization (Y. Yang & Jia, 2017a). As reported in Y. Yang and Jia (2017a), group sparsity promotes the underlying structural information of conductivity distribution. The constrained optimization problem can be formulated as

$$\begin{cases} \min_{\Delta\sigma} \|\Delta\sigma\|_{2,1} := \sum_{i=1}^N \|\Delta\sigma_{S_i}\|_2 \\ s.t. \mathbf{J}\Delta\sigma = \Delta\mathbf{V} \end{cases} \quad (3.3)$$

where $\|\cdot\|_{2,1}$ denotes the $l_{2,1}$ norm, which is the sum of energy of each defined group. It has been proved to facilitate group sparsity, i.e. minimizing the $l_{2,1}$ norm suppresses pixel groups with very small energies while promoting those present large energies (Huang & Zhang, 2010; Obozinski, Taskar, & Jordan, 2010). This way, it takes advantage of the structural prior and improves image quality.

We apply the Alternating Direction Method of Multipliers (ADMM) to solve (3.3). ADMM is a prevailing approach for solving constrained separable optimization problems by breaking the objective function into several sub-problems without coupled variables (Fukushima, 1992; J. Wang et al., 2020). By introducing an auxiliary vector $\mathbf{x} \in \mathbb{R}^n$, the problem in (3.3) can be rewritten as

$$\begin{cases} \min_{\Delta\sigma, \mathbf{x}} \sum_{i=1}^N \|\mathbf{x}_{S_i}\|_2 \\ s.t. \mathbf{x} = \Delta\sigma, \mathbf{J}\Delta\sigma = \Delta\mathbf{V} \end{cases} \quad (3.4)$$

Equivalently, we solve the following augmented Lagrangian problem.

$$\min_{\Delta\sigma, \mathbf{x}} \sum_{i=1}^N \|\mathbf{x}_{S_i}\|_2 - \boldsymbol{\gamma}_1^T (\mathbf{x} - \Delta\sigma) + \frac{\alpha_1}{2} \|\mathbf{x} - \Delta\sigma\|_2^2 - \boldsymbol{\gamma}_2^T (\mathbf{J}\Delta\sigma - \Delta\mathbf{V}) + \frac{\alpha_2}{2} \|\mathbf{J}\Delta\sigma - \Delta\mathbf{V}\|_2^2 \quad (3.5)$$

where $\boldsymbol{\gamma}_1, \boldsymbol{\gamma}_2 \in \mathbb{R}^n$ are multipliers and $\alpha_1, \alpha_2 \in \mathbb{R}$ denote the penalty parameters.

We then split (3.5) as two sub-problems which are expressed by

$$\mathbf{x}^{(k+1)} = \arg \min_{\mathbf{x}} \sum_{i=1}^N \left\| \mathbf{x}_{S_i}^{(k)} \right\|_2 - \boldsymbol{\gamma}_1^T \mathbf{x}^{(k)} + \frac{\alpha_1}{2} \left\| \mathbf{x}^{(k)} - \Delta \boldsymbol{\sigma} \right\|_2^2 \quad (3.6)$$

$$\Delta \boldsymbol{\sigma}^{(k+1)} = \arg \min_{\Delta \boldsymbol{\sigma}} \left\{ \boldsymbol{\gamma}_1^T \Delta \boldsymbol{\sigma}^{(k)} + \frac{\alpha_1}{2} \left\| \mathbf{x} - \Delta \boldsymbol{\sigma}^{(k)} \right\|_2^2 - \boldsymbol{\gamma}_2^T \mathbf{J} \Delta \boldsymbol{\sigma}^{(k)} + \frac{\alpha_2}{2} \left\| \mathbf{J} \Delta \boldsymbol{\sigma}^{(k)} - \Delta \mathbf{V} \right\|_2^2 \right\} \quad (3.7)$$

The sub-problem in (3.6) can be solved by soft-thresholding in a group-wise manner (Deng, Yin, & Zhang, 2013), i.e.

$$\mathbf{x}_{S_i} = \max \left\{ \left\| \Delta \boldsymbol{\sigma}_{S_i} + \frac{1}{\alpha_1} (\boldsymbol{\gamma}_1)_{S_i} \right\|_2 - \frac{1}{\alpha_1}, 0 \right\} \cdot \frac{\Delta \boldsymbol{\sigma}_{S_i} + \frac{1}{\alpha_1} (\boldsymbol{\gamma}_1)_{S_i}}{\left\| \Delta \boldsymbol{\sigma}_{S_i} + \frac{1}{\alpha_1} (\boldsymbol{\gamma}_1)_{S_i} \right\|_2} \quad (3.8)$$

While the sub-problem in (3.7) is a convex quadratic problem, which can be solved directly by asserting its gradient to zero, i.e.

$$\boldsymbol{\gamma}_1 + \alpha_1 (\Delta \boldsymbol{\sigma}^{(k)} - \mathbf{x}) + \mathbf{J}^T (\alpha_2 (\mathbf{J} \Delta \boldsymbol{\sigma}^{(k)} - \Delta \mathbf{V}) - \boldsymbol{\gamma}_2) = 0 \quad (3.9)$$

After solving these two sub-problems, we update the multipliers:

$$\begin{cases} \boldsymbol{\gamma}_1 = \boldsymbol{\gamma}_1 - \eta_1 \alpha_1 (\mathbf{x} - \Delta \boldsymbol{\sigma}) \\ \boldsymbol{\gamma}_2 = \boldsymbol{\gamma}_2 - \eta_2 \alpha_2 (\mathbf{J} \Delta \boldsymbol{\sigma} - \Delta \mathbf{V}) \end{cases} \quad (3.10)$$

where $\eta_1, \eta_2 \in \mathbb{R}$ represent the step sizes.

In summary, the pseudo-code implementation of the DL-GS algorithm is presented in Algorithm 1.

3.2.2 Evaluation Metrics

We quantitatively evaluate the performance of image reconstruction algorithms using Correlation Coefficient (CC), which is defined as

$$CC = \frac{\sum_{i=1}^n (\Delta \hat{\boldsymbol{\sigma}}_i - \overline{\Delta \hat{\boldsymbol{\sigma}}}) (\Delta \boldsymbol{\sigma}_i - \overline{\Delta \boldsymbol{\sigma}})}{\sqrt{\sum_{i=1}^n (\Delta \hat{\boldsymbol{\sigma}}_i - \overline{\Delta \hat{\boldsymbol{\sigma}}})^2 \sum_{i=1}^n (\Delta \boldsymbol{\sigma}_i - \overline{\Delta \boldsymbol{\sigma}})^2}} \quad (3.11)$$

Algorithm 1: DL-GS Algorithm**Input:** Boundary voltage measurement ΔV .**Initialize:** \mathbf{x} , $\Delta\sigma$, $\boldsymbol{\gamma}$, $\boldsymbol{\eta}$, η_1 , η_2 , α_1 , α_2 .

- 1 Calculate the binary mask \mathbf{M} using FC-UNet;
- 2 Calculate the group index vector based on S ;
- 3 **while** *the stopping criterion is not satisfied* **do**
 - a) Solve the first sub-problem (3.6) using (3.8);
 - b) Solve the second sub-problem (3.7) using (3.9);
 - c) Update multipliers using (3.10);

Output: Estimated conductivity change $\Delta\sigma$.

where $\Delta\hat{\sigma}$ and $\Delta\sigma$ represents the predicted conductivity and ground truth, respectively; $\Delta\hat{\sigma}_i$ and $\Delta\sigma_i$ denotes the i th element of $\Delta\hat{\sigma}$ and $\Delta\sigma$, respectively; $\overline{\Delta\hat{\sigma}}$ is the mean of $\Delta\hat{\sigma}$, and $\overline{\Delta\sigma}$ is the mean of $\Delta\sigma$; n is the total number of pixels. A larger CC indicates better image quality.

3.3 Experimental Setup

3.3.1 Data Set Generation

Simulation Data

To generate data set for FC-UNet training, we model a circular 16-electrode EIT sensor using COMSOL Multiphysics. We adopt the adjacent measurement strategy and discretize the sensing region with $n = 3228$ pixels.

3D cultivated cell aggregates are approximately circular. Therefore, we consider circular phantoms with uniformly randomly assigned object numbers (1 to 4), size (from 0.03d to 0.3d; d is the sensor diameter), location and conductivity values. The conductivity of the circular objects is bounded within the range of $0.0001 S \cdot m^{-1}$ and $0.05 S \cdot m^{-1}$. The background substance has a constant conductivity of $0.05 S \cdot m^{-1}$. The forward problem of EIT is calculated regarding each randomly generated phantom to obtain the corresponding measurement. An example of the generated phantom with its voltage data is shown in Fig. 3.4.

We finally generated 29,333 multi-level EIT samples, including 7035 1-object samples, 7298 2-object samples, 7500 3-object samples and 7500 4-object samples (the dataset is available at <https://datashare.ed.ac.uk/handle/10283/4440>). We then divided this dataset into a training set (6000 samples from each case), a validation set (500 samples from each case), and a testing set (the remaining samples). The three subsets contain 24k, 2k and 3,333 samples, respectively.

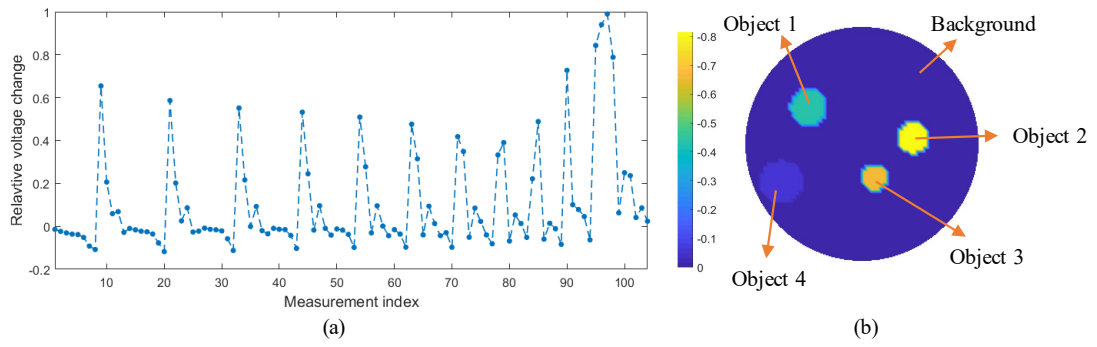


Figure 3.4: A 4-object example of simulation data. (a) Boundary voltage change. (b) Corresponding conductivity distribution.

In addition, we implement data augmentation by adding Gaussian noise to measurement data in both training and validation sets to enhance the robustness of our model when system noise or error is encountered. Additive noise with the Signal-to-Noise Ratio (SNR) of 50dB is added to half of the training and validation samples for each case. Additive noise with an SNR of 40dB is added to the other half of the training and validation data. As a result, both training and validation data are doubled. Testing data are added noise with SNR of 50dB, 40dB and 30dB. Table 3.1 summarizes the constitution of the training, validation, and testing data sets.

Table 3.1: Number of samples in each data set

Data set	Training	Validation	Testing
Noise Free Samples	24,000	2,000	3,333
50dB Samples	12,000	1,000	3,333
40dB Samples	12,000	1,000	3,333
30dB Samples	/	/	3,333
Total Samples	48,000	4,000	13,332

Experimental Data

To validate the multi-conductivity-level performance of the proposed method using mEIT, we employed the 16-electrode miniature EIT sensor designed in Y. Yang et al. (2016) to collect phantom experiment data (see Fig. 3.5). The inner diameter of the sensing chamber is 15 mm and the height is 10 mm. A carrot and a rubber cylinder, which has similar size but different conductivity (rubber: non-conductive; carrot: less conductive than the background), were imaged. Additionally, we conducted experiments on MCF-7 human breast cancer cell aggregates to examine the performance in cell imaging. In this case, a 16-electrode quasi-2D miniature EIT sensor (Y. Yang, Wu, & Jia, 2018), which is able to incorporate impedance sensing with optical imaging modalities, and a multi-frequency EIT system designed by Y. Yang and Jia (2017b) were employed for cell imaging (MCF-7 cell: less conductive than the background). The schematic and manufactured miniature EIT sensor, and 3D cultivated

MCF-7 cell aggregates are presented in Fig. 3.6. The sensing chamber has a diameter of 14mm and a height of 1.6mm. Two MCF-7 human breast cancer cell aggregates with a diameter of approximately 2mm were imaged. More details regarding experimental phantoms are presented in Section 3.4.3.

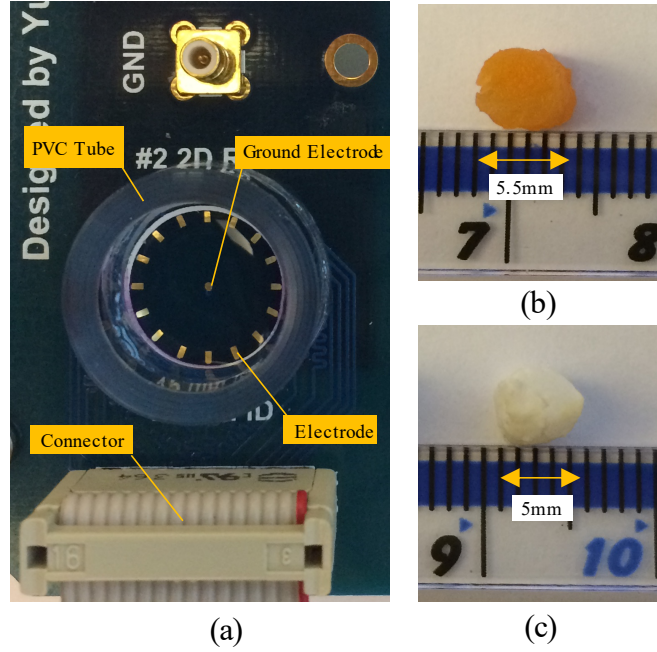


Figure 3.5: Experimental setup for carrot and rubber phantom. (a) The miniature EIT sensor (Y. Yang et al., 2016). (b) Carrot cylinder. (c) Rubber cylinder.

3.3.2 Data Normalization

In FC-UNet training, to reduce the effect of sensor imperfection, we normalize the voltage measurement and conductivity distribution by

$$\Delta \mathbf{V}_n = \frac{\mathbf{V}_{mea} - \mathbf{V}_{ref}}{\mathbf{V}_{ref}} \quad (3.12)$$

$$\Delta \boldsymbol{\sigma}_n = \frac{\boldsymbol{\sigma}_{mea} - \boldsymbol{\sigma}_{ref}}{\boldsymbol{\sigma}_{ref}} \quad (3.13)$$

where \mathbf{V}_{ref} and $\boldsymbol{\sigma}_{ref}$ represent the measurement and conductivity distribution, respectively, when the sensing region is only filled with background substance; \mathbf{V}_{mea} and $\boldsymbol{\sigma}_{mea}$ denote respectively the measurement and conductivity distribution after objects are present in the sensing region.

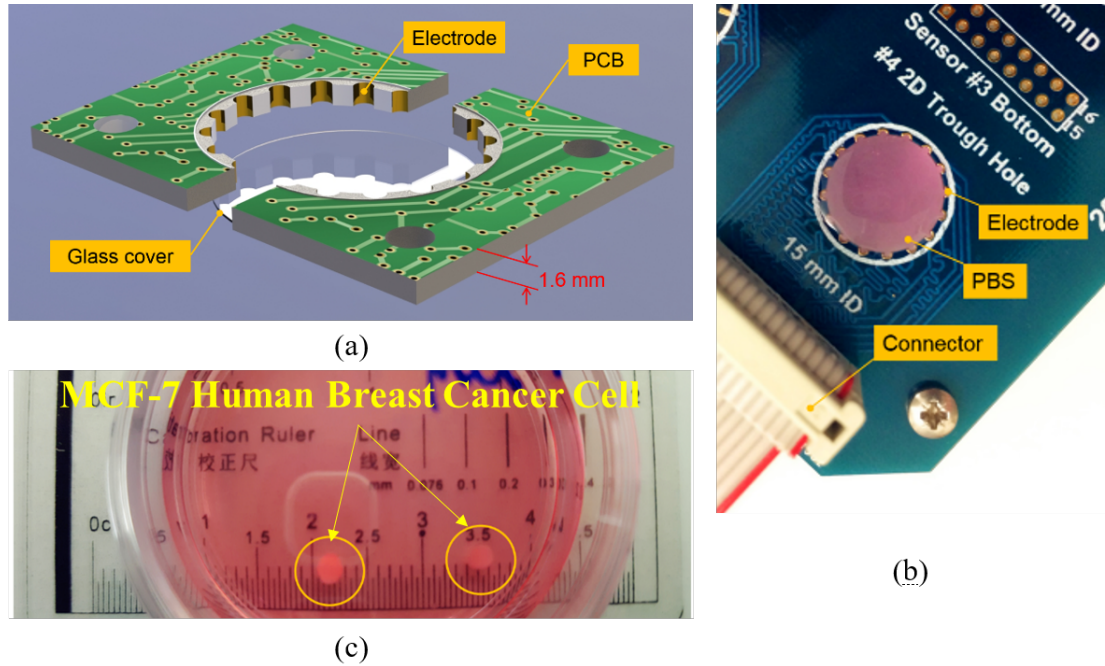


Figure 3.6: Experimental setup for cell imaging. (a) Sensor schematic. (b) The manufactured quasi-2D miniature EIT sensor (Y. Yang, Wu, & Jia, 2018). (c) MCF-7 cell aggregates.

During training, one option is to retain the varying conductivity changes from (3.13), in which case the FC-UNet solves a regression problem. Then all the output's non-zero pixels are set as one to generate the binary mask. Whilst the alternative is to binarize the conductivity values from (3.13) before training and use this binary format as ground truth so that it becomes a classification task. We investigated both options and found that the latter performs better in terms of accuracy. Therefore, we adopt the latter in training.

3.3.3 Network Training

To train the FC-UNet model, we use the well-known Adam (Kingma & Ba, 2014) for optimization. The initial learning rate is 0.0001. We also introduce the step decay for the training, where the learning rate is reduced by a factor of 0.1 every 25 epochs to promote faster convergence and higher accuracy. The effect of step decay will be discussed in Section 3.4.1. The model is trained with a batch size of 25.

Inspired by transfer learning which takes a pre-trained model of one task as a starting point for another task (Torrey & Shavlik, 2010), we initialize weights for the fully connected layer with the pre-calculated least-squares (LS) solution of (2.7) using training data, instead of random weights. During training, these weights are further fine-tuned. The rest is initialized with random weights as usual.

The maximum number of training epochs is set as 50. The final model is selected according to the validation loss. That is, the training process stops at the point with the least validation loss. Experiments are implemented using NVIDIA P5000 GPUs.

3.4 Results and Discussions

3.4.1 Learning Curve of FC-UNet

Learning curves (see Fig. 3.7) illustrate the effect of step decay when training the FC-UNet. It can be observed that the training curve in blue using step decay shows a step decrease at the 25th epoch when the learning rate is reduced by a factor of 0.1. This curve has a lower asymptote at the end compared to the training curve in green, which utilizes a constant learning rate in the entire learning process and converges at a local minimum. This implies that introducing the step decay term can promote convergence at a better minimum and achieve considerably lower loss.

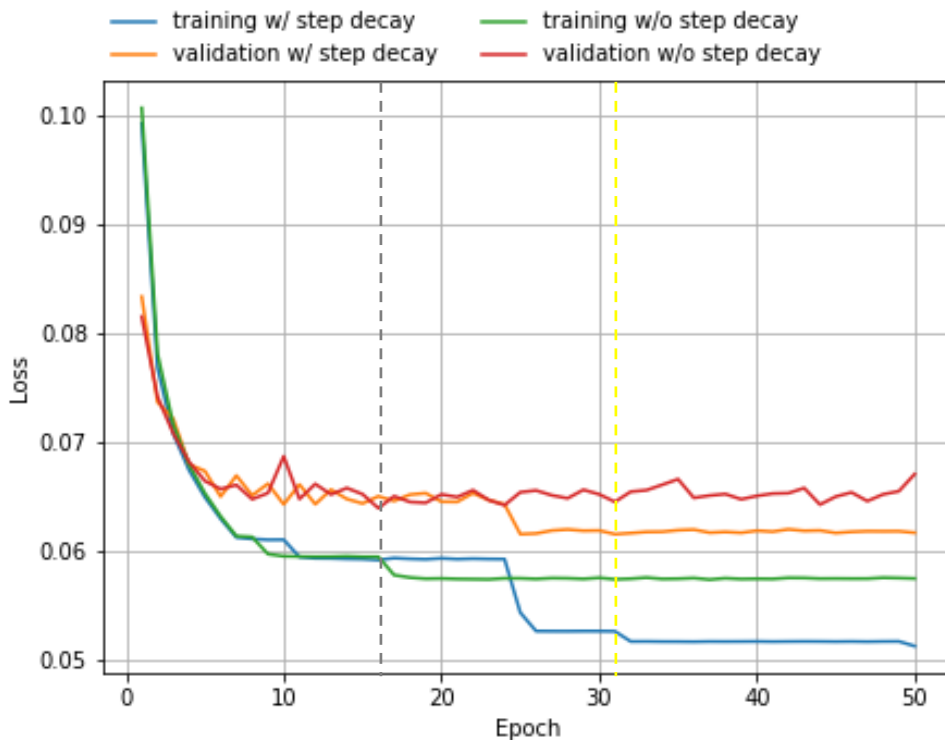


Figure 3.7: The learning curves of the FC-UNet.

The orange and red lines represent the validation loss curves with and without step decay, respectively. In the initial phase, both validation losses are smaller than the corresponding training losses. This means more training is required since the model underfits the training data. After 3 epochs, the training loss starts exceeding the validation loss. The dashed grey and yellow dashed lines indicate where the lowest validation loss is reached and the training process stops. Obviously, the step decay contributes to much better validation performance.

3.4.2 Results Based on Simulation Data

Fig. 3.8(a) shows four multi-level conductivity phantoms in the testing data set. In the simulation, additive Gaussian noise with an SNR of 50dB was added to the measurements. Theoretically, as the number of inclusion and conductivity levels increases, the estimation of conductivity distribution in the binary form is more challenging. Fig. 3.8(b) gives binary results generated by FC-UNet and correlation coefficients of all phantoms are shown in Fig. 3.9. The numerical results suggest that FC-UNet performs well in predicting the positions and shapes of the given multi-conductivity-level phantoms.

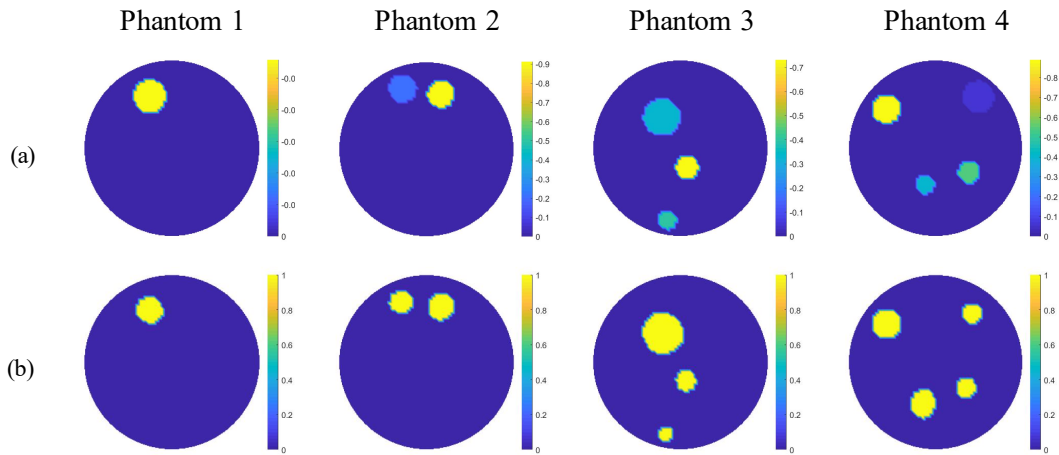


Figure 3.8: Multi-conductivity-level phantoms and binary masks generated by FC-UNet. (a) Ground Truth (b) Corresponding binary masks from FC-UNet.

We then compare the multi-conductivity-level reconstruction results of the proposed DL-GS method with some state-of-the-art EIT image reconstruction algorithms, i.e. l_1 regularization (l_1) (Tehrani et al., 2012), Sparse Bayesian Learning (SBL) (S. Liu et al., 2018), AGS (Y. Yang & Jia, 2017a), and LeNet (Tan et al., 2018). During implementation, stopping tolerance is set as $1e-7$. The maximum iteration numbers of l_1 , SBL, AGS, and DL-GS are respectively set as 50, 20, 500, and 500. The block size of SBL is 4. For AGS, the maximum diameter of the group is set as 10 pixels. The penalty vectors of AGS and DL-GS are respectively $[1/|\Delta\mathbf{V}|]$, $5/|\Delta\mathbf{V}|]$, and $[10/|\Delta\mathbf{V}|]$, $0.1/|\Delta\mathbf{V}|]$ throughout the experiment. The training procedure for LeNet is the same as that for FC-UNet except that mean square error is the loss function.

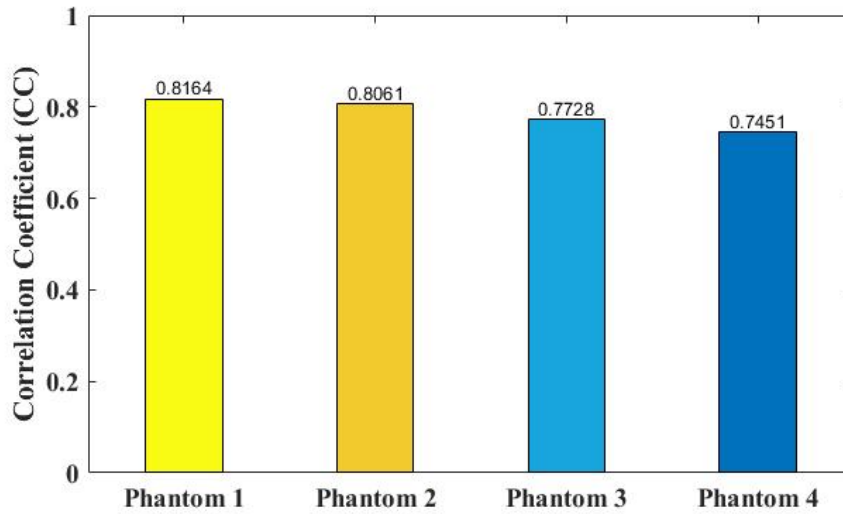


Figure 3.9: Correlation coefficients of the FC-UNet results.

Fig. 3.10 shows the relative conductivity changes reconstructed by different algorithms. For the phantom with a small conductivity change in the first row, AGS recovers better size compared to l_1 , SBL, and LeNet whereas they all underestimate the object dimension. In contrast, DL-GS provides much better results in terms of both structure and conductivity variation. As the number of objects and conductivity levels increases (see phantoms from the second to the fourth row), l_1 , SBL, AGS, and LeNet fail to reconstruct the shape and conductivity difference, and objects with smaller conductivity changes are barely recovered. In comparison, DL-GS outputs more accurate shapes as well as conductivity variations. Particularly, when there are four objects, DL-GS is the only algorithm that manages to recognize them all and recovers more faithful conductivity information.

Table 3.2 compares the average CC of all phantoms in the testing set when the noise of various levels is added to measurements. We can observe that DL-GS outperforms the other algorithms in all cases, with the highest CC. Noting that it performs even better than the purely deep learning method LeNet by 5.9%. All algorithms exhibit their robustness to noise and there is a continuous decrease in CC with the growth of SNR. Table 3.3 reports the average model execution time per image. LeNet achieves the fastest running time, indicating the prominent advantage of using a deep neural network. DL-GS is the second fastest algorithm, substantially 6.5 times better than AGS on average. As expected, the FC-UNet significantly reduces the computation time for pixel grouping whereas in AGS, the initial grouping from one-step Gauss-Newton requires much longer time.

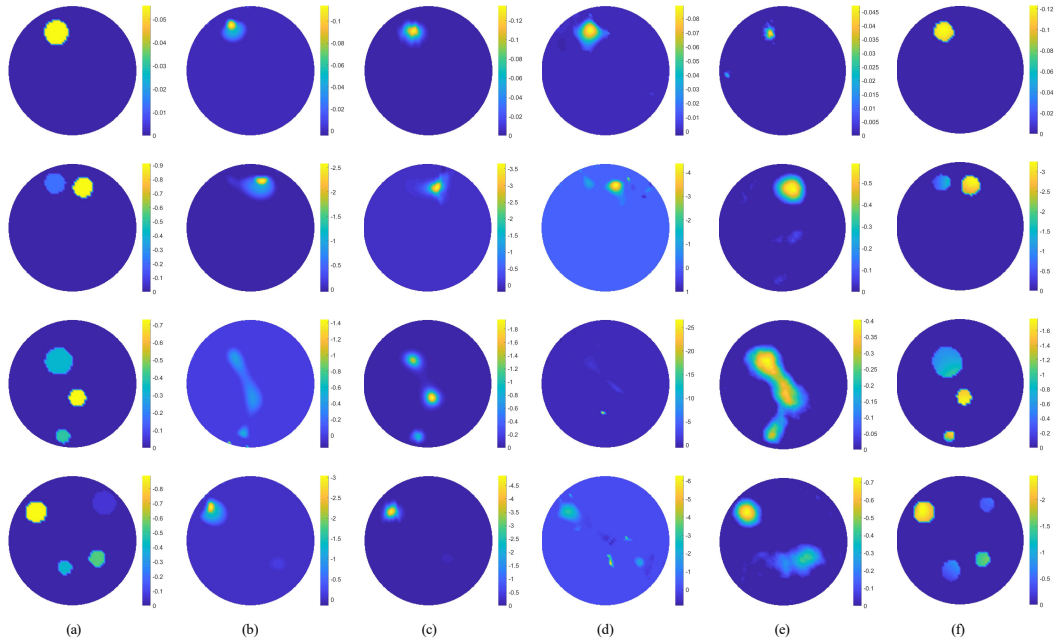


Figure 3.10: Image reconstruction results of four phantoms from testing data set (SNR = 50 dB) (note we use inverted color bar). (a) Ground truth (b)-(e) Corresponding results of l_1 , SBL, AGS, LeNet, and DL-GS respectively.

Table 3.2: Comparison of average CC

Image Reconstruction Algorithm	SNR			
	Noise Free	50dB	40dB	30dB
l_1 (Tehrani et al., 2012)	0.5268	0.5276	0.5244	0.5253
SBL(S. Liu et al., 2018)	0.5634	0.5633	0.5628	0.5617
AGS(Y. Yang & Jia, 2017a)	0.5263	0.5224	0.5196	0.4982
LeNet(Tan et al., 2018)	0.6445	0.6420	0.6124	0.5233
DL-GS	0.7215	0.6639	0.6161	0.5648

Table 3.3: Comparison of average model execution time per image [s]

Image Reconstruction Algorithm	SNR			
	Noise Free	50dB	40dB	30dB
l_1 (Tehrani et al., 2012)	0.4867	0.4878	0.4636	0.4689
SBL(S. Liu et al., 2018)	12.95	13.00	13.03	12.85
AGS(Y. Yang & Jia, 2017a)	0.7388	0.7573	0.7520	0.7396
LeNet(Tan et al., 2018)	0.22e-3	0.26e-3	0.25e-3	0.27e-3
DL-GS	0.1114	0.1131	0.1128	0.1127

3.4.3 Results Based on Experimental Data

In addition to validation with simulation data, we collect experimental data using different miniature EIT sensors to examine the performance of DL-GS. When implementing l_1 , SBL, AGS, LeNet, and DL-GS, all parameters are the same as in simulation settings.

Three phantoms as shown in the first column of Fig. 3.11 were imaged. The first phantom contains carrot and rubber cylinders with saline as the background. The excitation frequency is 20kHz and the maximum iteration of DL-GS is 350. Intrinsically, the rubber at the lower left corner has lower conductivity than the carrot (i.e. the rubber leads to larger conductivity change with respect to background), which is successfully recovered by all algorithms but most significantly by LeNet and DL-GS. DL-GS also reconstructs the best shape of both objects with clear boundaries. The other two phantoms image two cell aggregates. Observing the results, l_1 can roughly identify both cell aggregates but there exists obvious distortion and artifacts. SBL consistently manages to reconstruct the two cell aggregates with good positions, whilst it underestimates the size of the cell and the artifact at the center of ROI is also distinct. AGS fails to reconstruct the phantoms clearly, which is even worse than l_1 and SBL. The underlying reason might be that AGS utilizes a one-step algorithm to estimate the structural information, but in this case, the one-step algorithm struggles to provide meaningful results for pixel grouping. LeNet performs well when the two cell aggregates are far from each other but has the same issues as l_1 when they become closer. With regard to DL-GS, it is able to obtain much better shape and position of each cell aggregate for both cases. Compared to l_1 , SBL, and AGS, DL-GS yields sharper edges for all reconstructed cell aggregates. Table 3.4 gives CC of experimental results, further confirming the successful transition of DL-GS to various experimental data. DL-GS achieves the highest CC for all the phantoms, outperforming the other algorithms. The results indicate that DL-GS can be generalized to the mEIT setup and facilitate robust and high-quality cell imaging.

Table 3.4: CC of experimental results

Phantom	1	2	3
l_1 (Tehrani et al., 2012)	0.4809	0.6490	0.7145
SBL(S. Liu et al., 2018)	0.4473	0.6271	0.6689
AGS(Y. Yang & Jia, 2017a)	0.3188	0.3666	-0.0020
LeNet(Tan et al., 2018)	0.5449	0.7704	0.7224
DL-GS	0.7477	0.8008	0.7650

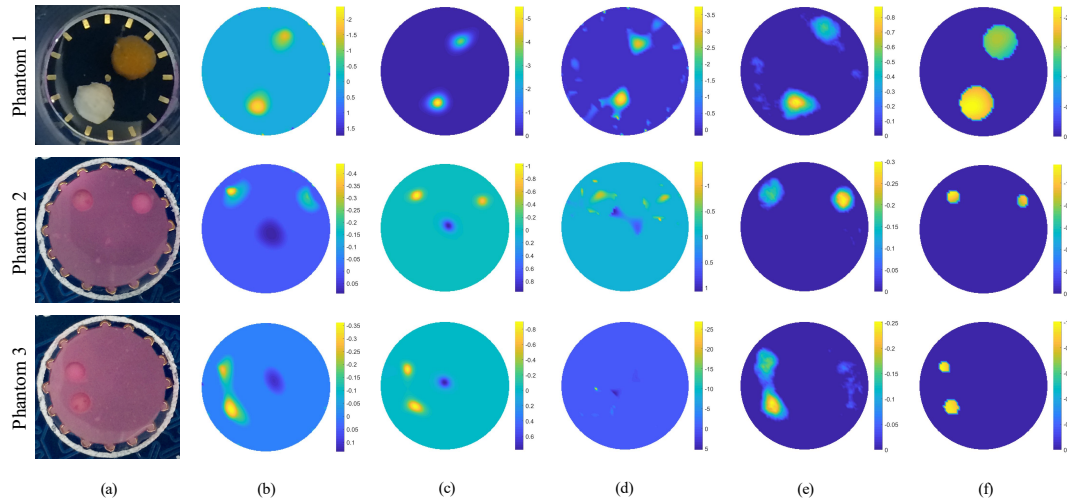


Figure 3.11: Image reconstruction results using experimental data (note we use inverted color bar). (a) Three setups. (b)-(e) corresponds to results of l_1 , SBL, AGS, LeNet, and DL-GS, respectively.

3.5 Summary

In this chapter, a deep learning and group sparsity regularization-based hybrid algorithm was proposed for 3D cultivated cell imaging with miniature EIT sensors. This work specifically focused on the challenge of performing multi-conductivity-level imaging under multiple objects setups. A novel EIT data set with continuously varying conductivity values for different sensing objects was established. An FC-UNet model was then developed to provide structural information of multi-level conductivity distribution. Afterwards, this structural information was integrated into group sparsity regularization to estimate the continuous conductivity values. Both simulation and experiments demonstrated that the proposed DL-GS method outperforms the other given image reconstruction approaches and demonstrates strong generalization ability on a practical miniature EIT sensor to image MCF-7 cell aggregates.

Cell Culture Imaging Using Structure-aware Learning

4.1 Introduction

Chapter 3 found the structure of target objects could be well-estimated in the form of binary masks and facilitate distinguishing the conductivity contrast of multiple targets. However, the conductivity value still could not be precisely estimated due to the error introduced by the linearized EIT model. Accurate reconstruction of continuous, multi-level conductivity variations and the structural distribution remain very challenging.

In this chapter, targeting cell culture imaging, a regression deep learning model is proposed to predict accurately both the geometric structure and conductivity value of multi-object, multi-conductivity-level conductivity distributions. Inspired by multi-modal learning for activity and context recognition (Radu et al., 2018) and the work of DL-GS in Chapter 3, a Structure-Aware Dual-Branch Network (SADB-Net) is developed for EIT image reconstruction. The SADB-Net consists of two branches to learn the structural and conductivity representations, respectively, in the first place. Then, the multi-branch features are fused by two fully connected layers. We demonstrate the effectiveness of the SADB-Net in reconstructing continuous, multi-level conductivity distributions with both simulation and experimental data on MCF-7 breast cancer cell aggregates, and benchmark the results with the baseline and state-of-the-art algorithms.

4.2 SADB-Net: A Learning-based Method for Cell Culture Imaging

4.2.1 Multi-Modal Deep Neural Network

We introduce the multi-branch characteristics of multi-modal deep learning to solve the target EIT-image-reconstruction problem. Some challenging learning tasks usually involve more than one sensing modality providing diverse input data. In such cases, the multi-modal solutions fuse different sensing streams to boost the accuracy of the predicted results. Deep architectures, e.g. Restricted Boltzmann Machine (RBM) (Ngiam et al., 2011) and Convolutional Neural Network (CNN) (Audebert, Le Saux, & Lefèvre, 2018), have been applied for multi-modal learning.

A straightforward strategy of multi-modal learning is to concatenate the inputs of different modalities, taking raw data or lightly pre-processed data at the input layer. Then the fused input is propagated through the neural network. However, this early fusion learning approach tends to emphasize the inherent cross-modality correlations (Ngiam et al., 2011), as early fusion and unbalanced mixture of inputs make it difficult to extract the potential intra-modality relations.

An alternative named Modality-specific Architecture (MA) (Radu et al., 2018) leverages both intra-modality and cross-modality correlations (see Fig. 4.1). In MA, information propagates through all layers. The input layer is fed with data from each modality and the output layer generates the final result. Separate branches (\mathcal{B}_n) are specified for each modality, without any connections in between. Through a couple of hidden layers in each branch, feature representations associated with every single modality are learned and merged afterwards by subsequent layers $u^{(i)}$ in the network. The output neurons of the L^{th} hidden layer, i.e. $h_i^{(L)}$, are determined by every neuron in the previous layer, i.e. $h_j^{(L-1)}$. In general, it can be formulated as:

$$h_i^{(L)} = \gamma\left(\sum_j w_{ij}^{(L)} h_j^{(L-1)}\right) \quad (4.1)$$

where $w_{ij}^{(L)}$ denotes the unit weight connecting the j^{th} neuron in layer $L - 1$ with the i^{th} neuron in layer L , and γ is the non-linear activation function. In this work, we simply adopt Rectified Linear Unit (ReLU) (Nair & Hinton, 2010):

$$\gamma(x) = \max(0, x). \quad (4.2)$$

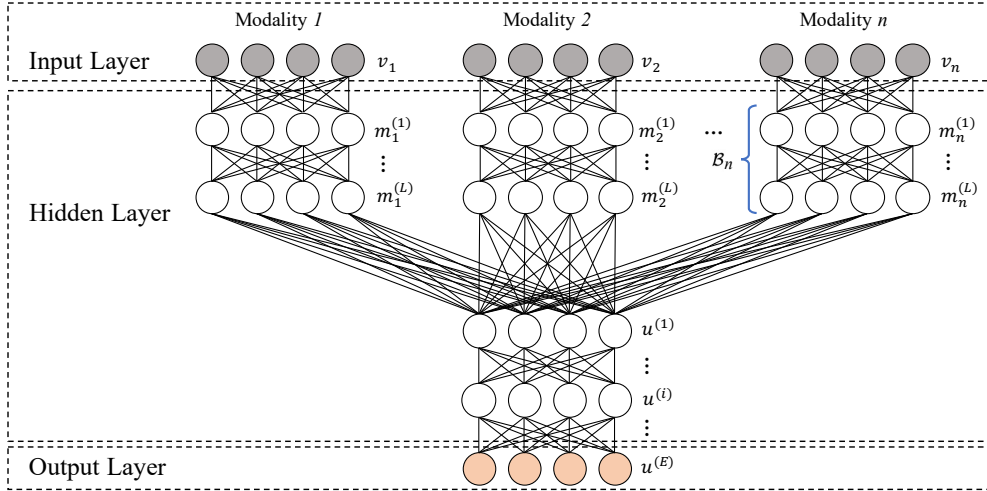


Figure 4.1: Schematic illustration of generic modality-specific deep neural network.

The generic MA in Fig. 4.1 comprises a multi-layer perceptron, which can be replaced with a CNN for multi-modal learning. CNN is characterized by shared weights in the form of stacks of filters, which parameters are trained to extract different high-level features. Using convolutional layers could avail more complicated patterns with far fewer parameters to learn. Inspired by MA, in this work we employ CNNs to learn intra-branch correlations over several layers and use fully connected layers to combine features from CNNs.

4.2.2 SADB-Net for EIT Image Reconstruction

We comprehend the EIT-image-reconstruction problem in a multi-modal context in the sense that the conductivity images reconstructed from the boundary voltage measurements generally contain two types of information: (a) geometric structure information and (b) conductivity value information. We first extract the binary structural information of the conductivity distribution and then utilize this binary image together with boundary voltage measurement as two inputs to tackle the regression problem. We will demonstrate this leads to a more accurate estimation of both structure distribution and conductivity values. Fig. 4.2 shows the schematic illustration of the proposed Structure-Aware Dual-Branch Network (SADB-Net) for EIT image reconstruction based on this idea. We design two separate branches to deal with the two types of information: one is the structure-related branch (see orange arrows in Fig. 4.2), and the other is the conductivity-value related branch (see blue arrows in Fig. 4.2).

The structure branch \mathcal{B}_S operates in the image domain, which consists of a mask generator and a feature extractor. The input vector first goes through the mask generator, which generates a binary mask to distinguish objects from the background. Following the work in Z. Chen, Yang, and Bagnaninchi (2020), we use the FC-UNet, a cascade of a fully connected layer and a UNet (Ronneberger et al., 2015) to learn the mapping from boundary voltage

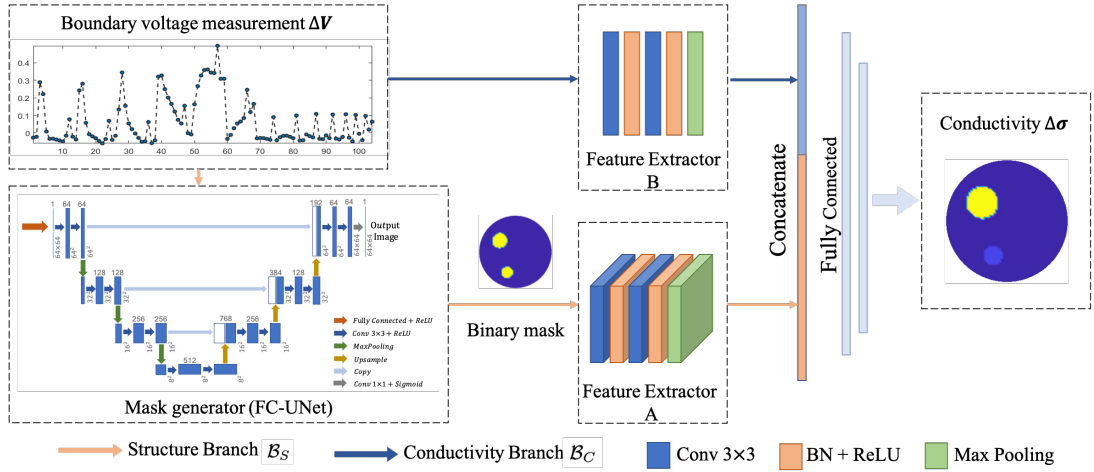


Figure 4.2: Schematic illustration of the proposed Structure-aware Dual-branch Network (SADB-Net).

measurement to a binary mask. A sigmoid activation function is selected as the last layer of FC-UNet to constrain all values within the range $[0, 1]$. The feature extractor A is constructed by a standard CNN, where the stack of two convolutional layers with 3×3 kernels and padding of 1 are followed by a max pooling layer. A batch normalization layer and a ReLU activation layer are applied after each convolutional layer. In this step, the binary mask (64×64) is reduced to a feature map of size $16 \times 16 \times 16$ (height, width, channel) by the feature extractor.

The conductivity branch \mathcal{B}_C takes the raw voltage measurement as input. Feature extractor B for \mathcal{B}_C has exactly the same architecture as that for the branch \mathcal{B}_S , except that all layers operate in one dimension. The output is a 52×16 (length, channel) feature map.

The two feature maps learned from branches \mathcal{B}_S and \mathcal{B}_C are then concatenated together into a 4928-dimensional vector. This vector passes through two fully-connected layers, which fuse the information from the two branches. The first fully-connected layer encodes the vector down to a hidden feature with 4900 neurons. The second finally predicts conductivity distributions in a continuous manner. Each fully-connected layer is followed by a ReLU activation layer.

4.2.3 Loss Function

Let $\Delta\sigma \in \mathbb{R}^n$ denote the conductivity variation distribution, $\Delta\mathbf{V} \in \mathbb{R}^m$ be the boundary voltage measurements change, and the SADB-Net $f_{SADB-Net}(\cdot)$ is parameterised by network weights θ , which calculation is described in Section 4.3.1.

Binary Cross Entropy Loss (\mathcal{L}_{BCE})

For binary mask generation in \mathcal{B}_S , we explicitly train the FC-UNet parameterised by network weights θ_{OD} using binary cross entropy loss on the predicted binary masks $\mathbf{M}_{pred} \in \mathbb{R}^n$, i.e.

$$\mathcal{L}_{BCE} = -\frac{1}{K} \sum_{i=1}^K (\mathbf{M}_{pred}^{(i)} \cdot \log \mathbf{M}_{gt}^{(i)} + (1 - \mathbf{M}_{pred}^{(i)}) \cdot \log(1 - \mathbf{M}_{gt}^{(i)})) \quad (4.3)$$

where K represents the size of dataset, $\mathbf{M}_{gt}^{(i)}$ denotes the ground truth for the i^{th} input-target pair. Given the ground truth of conductivity distribution $\Delta\sigma_{gt}^{(i)}$, $\mathbf{M}_{gt}^{(i)}$ is generated by setting all non-zero elements in $\Delta\sigma_{gt}^{(i)}$ to one while the rest remains zero.

Total Loss (\mathcal{L}_{Total})

For the ultimate reconstruction task, our loss function intends to combine the per-pixel reconstruction accuracy with spatial piecewise smoothness in the predicted conductivity values.

Given the predicted conductivity distribution $\Delta\sigma_{pred} = f_{SADB-Net}(\Delta\mathbf{V}; \theta)$ and training dataset \mathcal{D} , we first define per-pixel losses with Mean Square Error (MSE), i.e.

$$\mathcal{L}_{MSE} = \frac{1}{K} \sum_{(\Delta\mathbf{V}, \Delta\sigma_{gt}) \in \mathcal{D}} \|\Delta\sigma_{gt} - \Delta\sigma_{pred}\|^2. \quad (4.4)$$

In addition to MSE loss, we also include l_2 loss (a regularization term) that is a function of the network weights θ :

$$\mathcal{L}_{l_2} = \|\theta\|_2^2 = \sum_i |\theta_i|^2. \quad (4.5)$$

Inspired by the work in super-resolution style transfer (Johnson, Alahi, & Fei-Fei, 2016), the last loss term adopts the Total Variation (TV) loss \mathcal{L}_{TV} as the piecewise smoothing penalty for $\Delta\sigma_{pred}$, i.e.

$$\mathcal{L}_{TV} = \sum_{i,j \in \Omega} |\Delta\sigma_{pred}(i+1, j) - \Delta\sigma_{pred}(i, j)| + |\Delta\sigma_{pred}(i, j+1) - \Delta\sigma_{pred}(i, j)|. \quad (4.6)$$

The total loss \mathcal{L}_{Total} is a combination of the above three terms:

$$\mathcal{L}_{Total} = \lambda_{MSE} \mathcal{L}_{MSE} + \lambda_{l_2} \mathcal{L}_{l_2} + \lambda_{TV} \mathcal{L}_{TV} \quad (4.7)$$

where $\lambda_{MSE}, \lambda_{l_2}, \lambda_{TV}$ are scalars for corresponding loss terms. Larger scalars are assigned to loss terms that are more critical. Here we consider the pixel-by-pixel loss \mathcal{L}_{MSE} as the most critical term. The loss term scalars are determined by performing hyper-parameter searching on the validation data set. After a series of experiments, we found that (1, 3e-6, 1e-8) is the most appropriate setting for $(\lambda_{MSE}, \lambda_{l_2}, \lambda_{TV})$.

4.2.4 Supervision Strategy

A specialized supervision strategy is developed as illustrated in Fig. 4.3. Inspired by multi-task deep learning (Luvizon, Picard, & Tabia, 2020), we first train the mask generator only with \mathcal{L}_{BCE} for 100 epochs. Then we freeze all parameters of the object detector and train the remaining network with \mathcal{L}_{Total} for around 200 epochs. That is, the full network is established on top of the pre-initialized mask generator.

An easier way is to perform the end-to-end supervision by adding the binary cross entropy loss \mathcal{L}_{BCE} to the total loss \mathcal{L}_{Total} by imposing weighting factors. However, as the mask generator is closer to the input layer and away from the output layer, the gradients of the binary cross entropy loss become much smaller when they arrive at the object detector during back-propagation. Consequently, it requires much longer training time and is more likely to converge to a worse local minimum. In contrast, the proposed training strategy directly feeds \mathcal{L}_{BCE} to the mask generator, which has two advantages: first, the mask generator is more sensitive to gradients from \mathcal{L}_{BCE} during training; second, it facilitates faster and better convergence performance.

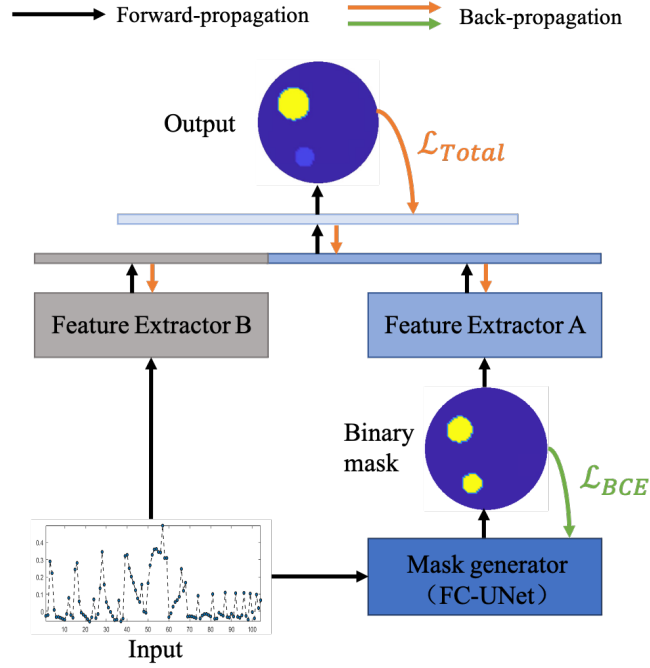


Figure 4.3: Deep supervision of SADB-Net.

4.2.5 Evaluation Metrics

We adopt the commonly used Relative Image Error (*RIE*) to assess the quality of the reconstructed images, i.e.

$$RIE = \frac{\|\Delta\sigma_{pred} - \Delta\sigma_{gt}\|}{\|\Delta\sigma_{gt}\|} \times 100\% \quad (4.8)$$

where $\Delta\sigma_{pred}$ and $\Delta\sigma_{gt}$ represent respectively the predicted and ground truth of conductivity distribution. *RIE* indicates the overall accuracy of the reconstruction quality in a pixel-by-pixel manner. Smaller *RIE* suggests better image quality.

4.3 Experimental Setup

4.3.1 Training Data Generation

To date, no open-source EIT dataset is available. Therefore, to mimic cell culture phantoms, we established an EIT dataset (the dataset is available at <https://datashare.ed.ac.uk/handle/10283/4440>) containing multiple continuously varying conductivity levels by modeling a circular 16-electrode EIT sensor in COMSOL Multiphysics (see Fig. 4.4(a)). The background conductivity is set as $0.05 \text{ S} \cdot \text{m}^{-1}$ and the conductivity of circular inclusions is uniformly randomly selected within the range $[1\text{e-}4, 0.05) \text{ S} \cdot \text{m}^{-1}$. Apart from uniformly distributed circular targets,

we also evaluated the performance of phantoms with single ring-shaped objects. We generated another group of ring-shaped dataset. Within each circular object, a smaller circular region is randomly created with the conductivity of $1 S \cdot m^{-1}$. The conductivity of the rest part of each object and the background is 0.1 and $2 S \cdot m^{-1}$, respectively. To evaluate the performance of non-circular imaging targets, we established another dataset containing 1 to 4 rectangular inclusions. The conductivity of each rectangular inclusion and the background are 0.0001 and $0.05 S \cdot m^{-1}$, respectively. We adopt adjacent measurement strategy (Brown & Seagar, 1987) and a completed non-redundant measurement vector contains 104 values. Further, we divide the circular sensing region by a 64×64 quadrate mesh, which contains 3228 pixels.

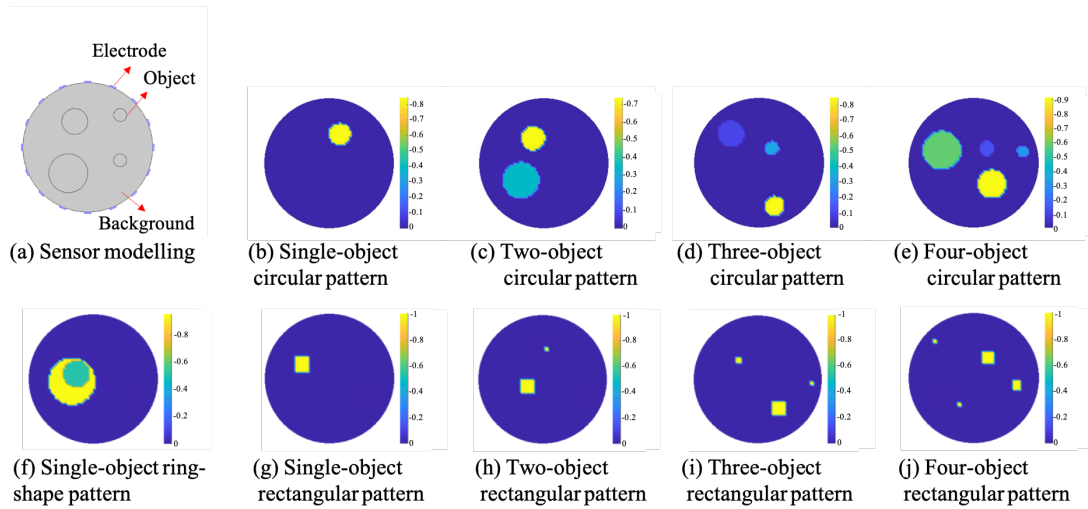


Figure 4.4: Sensor modelling and examples of nine patterns in the EIT data set.

In total, we randomly generated 54,333 pairs of samples through finite element modelling simulation. The dataset consists of nine different patterns with random object sizes, positions and conductivity values (see examples in Fig. 4.4). This data set is further partitioned into training set (6k samples of each circular pattern, 4k samples of ring-shape pattern, 4k samples of each rectangular pattern), validation set (500 samples of each pattern), and testing set (all the remaining samples). Accordingly, the three subsets contain 44k, 4,500 and 5,833 samples, respectively.

Data Augmentation

We implement data augmentation by adding Gaussian noise with diverse levels to voltage measurements in training, validation and testing data sets. The purpose is to mitigate the data limitation issue and improve robustness when dealing with noise-contaminated data. For the training and validation set, white noise with Signal-to-Noise Ratio (SNR) of 50dB and 40dB is added to half of the samples of each subset and the other half samples, respectively. The number of samples in the training and validation subset is then doubled. In addition, we add white noise with SNR of 50dB and 40dB to all samples in the testing subset to validate the performance of SADB-Net. Table 4.1 gives the number of samples in training, validation, and testing subsets before and after augmentation.

Table 4.1: Number of samples in each dataset

Dataset	<i>Training</i>	<i>Validation</i>	<i>Testing</i>
Before Augmentation	44,000	4,500	5,833
After Augmentation	88,000	9,000	17,499

Data Normalization

To reduce systematic defects caused by sensor imperfection, an additional pre-processing procedure is conducted to normalize the voltage measurements and conductivity in the data set as did in (3.12) and (3.13).

4.3.2 Network Training

To train the FC-UNet as a mask generator, the optimization setup is exactly the same as that in previous work (Z. Chen et al., 2020). For the rest of the SADB-Net, we use Adam (Kingma & Ba, 2014) with a batch size of 25 and a base learning rate of 0.0001, which is reduced by a factor of 0.1 with a step size of 25. Except for the pre-trained weights of FC-UNet, all other weights are initialized randomly. The weight decay in Adam has the same function with the l_2 penalty and thus is set as $3e-6$. The training was carried out on two NVIDIA P5000 GPUs, and we select the model with the least validation loss as the final one to avoid overfitting.

4.3.3 Baseline

We select the FC-UNet reported in Z. Chen et al. (2020) as the baseline algorithm since it does not require further preprocessing of the dataset. As this chapter solves a regression problem, we replace the last sigmoid layer (suited for classification/segmentation) in the original FC-UNet with a ReLU layer.

We also compare performance with L1 regularization (L1) (Jin et al., 2012), Laplacian filter (Lap) (Y. Yang et al., 2014), Sparse Bayesian Learning (SBL) (S. Liu et al., 2018) and LeNet (Tan et al., 2018). L1 (Jin et al., 2012) is an iterative model-based reconstruction algorithm with a maximum iteration number of 50. Lap is the one-step linear Gauss-Newton solver with Laplacian filter with a regularization factor of 0.05 (Y. Yang et al., 2014). LeNet and SBL are two recently reported learning-based EIT image reconstruction algorithms. SBL was implemented according to S. Liu et al. (2018), where we select the stopping tolerance to be $1e - 9$, the maximum iteration number to be 20 and the block size to be 7, after a careful tuning process.

4.4 Results and Discussions

4.4.1 Evaluation on Simulation Data

Case Study

We show some representative reconstruction examples using testing data under 50dB SNR (see Fig. 4.5). Fig. 4.6 gives the RIE of each phantom.

Overall, SADB-Net outperforms the other five methods. L1, Lap, SBL, LeNet and the baseline are suboptimal because the Lap, LeNet and baseline contain artifacts, L1 and SBL keep underestimating the shape of the objects (see Fig. 4.5). In Phantom 1 and 2, only SADB-Net manages to recover all objects in terms of both shape and conductivity value. SADB-Net uses an extra pipeline to learn the conductivity value, merges this feature with the structural feature from the other pipeline, and could better recover the global information. In these cases, L1, Lap, SBL, LeNet and the baseline are unable to reveal the conductivity difference of the objects, whereas SADB-Net succeeds to reconstruct this critical information. Regarding the more challenging Phantom 3, L1, Lap, SBL and LeNet even fail to recognize the correct number of objects within the region and the baseline hardly distinguishes the two objects in the middle, not to mention the conductivity levels. However, SADB-Net recovers the best structural information and at least figures out the conductivity value of the one at the lower left corner that is most significantly different from the background. For non-uniformly distributed inclusions, the reconstruction results demonstrate that all networks can handle Phantom 4 and 5 better than L1, Lap, and SBL, especially in terms of shape reconstruction. The baseline is comparable to SADB-Net but SADB-Net can better localize the region with a lower conductivity contrast. Comparing the reconstruction results of Phantom 6, it is obvious that only SADB-Net provides the most accurate shape while the other methods tend to generate unexpected circular objects.

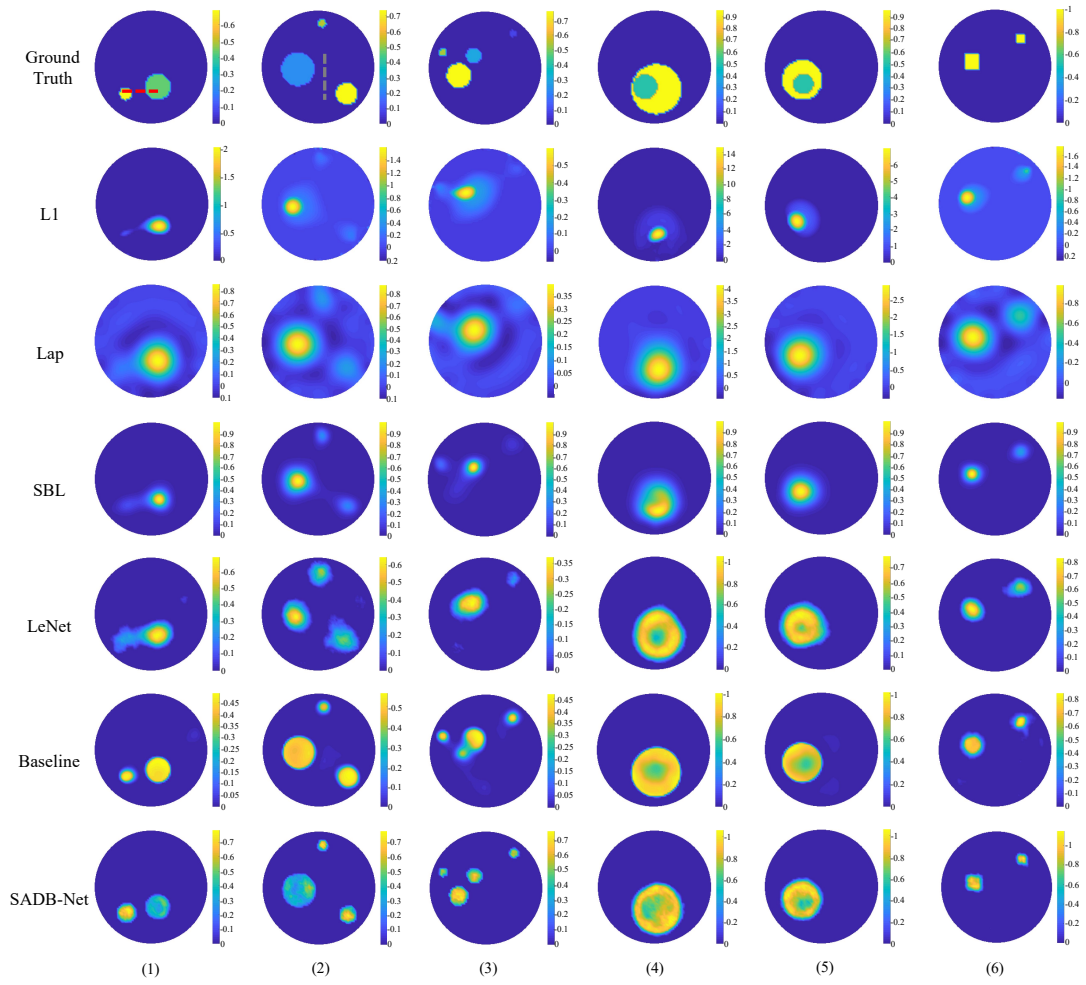


Figure 4.5: Image reconstruction results based on simulation data (SNR = 50 dB) in testing set. Each column corresponds to a phantom.

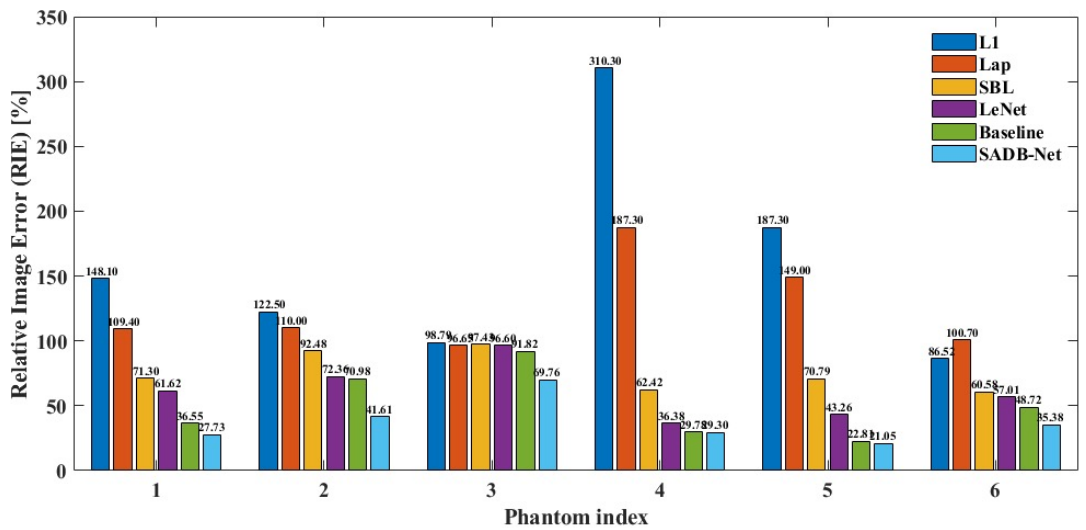


Figure 4.6: Numerical comparisons of six phantoms based on *RIE*.

However, a remarkable advantage of the baseline can be noted, i.e. its shallower architecture with a straight pipeline is more sensitive to \mathcal{L}_{TV} so that the reconstructed results are smoother than those of SADB-Net. The multi-branch representations which are joined later in SADB-Net are more informative, which consequently improves the overall image quality in terms of conductivity values of multiple objects, at the expense of less smoothness in the reconstructed images.

In Fig. 4.6, RIE of all methods, in general, gets worse as the number of objects increases. SADB-Net consistently yields the best RIE of 27.73%, 41.61%, and 69.76% relatively for Phantom 1-3, suggesting its high accuracy of estimating complicated conductivity distributions. The gap among L1, Lap, SBL, LeNet and baseline shrinks with increasing inclusions. For ring targets in Phantom 4 and 5 and rectangular targets in Phantom 6, deep learning methods show significantly lower RIE than conventional methods.

Fig. 4.7 presents high- and low-contrast profiles of reconstructions for Phantom 1 and 2, marked by dashed line segments in the first row of Fig. 4.5. For the high-contrast case, L1, Lap, SBL and LeNet deviate far from the ground truth, while the baseline and SADB-Net can smooth the details but SADB-Net better follows the two transitions. With respect to the low-contrast profile, L1 and SADB-Net overlap with the ground truth, but Lap, LeNet and baseline show deep troughs, suggesting obvious artefacts in their reconstructed background.

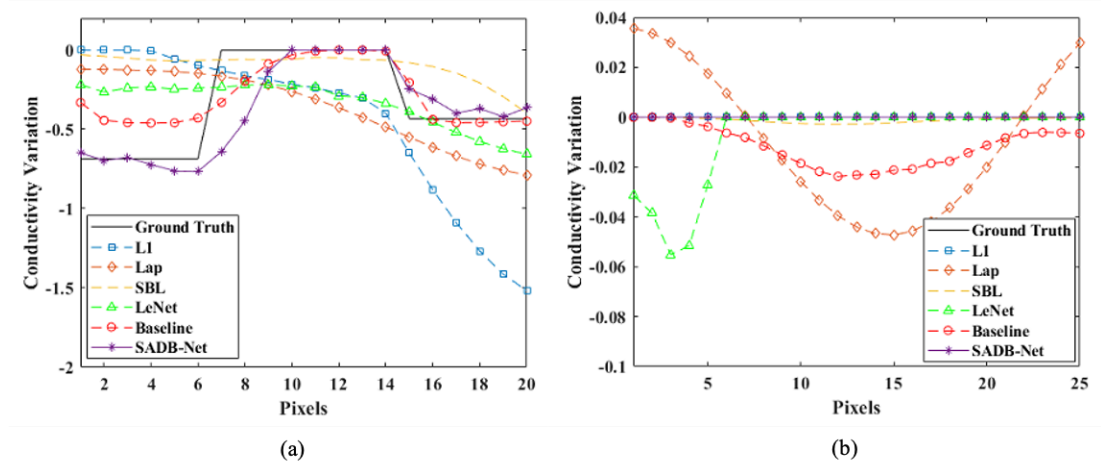


Figure 4.7: (a) High-contrast profile in (3) of Fig. 4.5 and (b) low-contrast profile in (4) of Fig. 4.5.

Quantitative comparisons

Table 4.2 reports the statistical average of *RIE* and running speed over all the testing data. We partition the results based on four different phantom patterns in Fig. 4.4 and three noise levels, i.e. *noise free*, *50dB*, and *40dB*.

Table 4.2: Performance comparisons (*RIE* and Speed) under different phantom patterns and noise levels.

No. of Objects	Noise Free				50dB				40dB			
	1	2	3	4	1	2	3	4	1	2	3	4
<i>RIE(L1)</i> (%)	95.73	111.9	118.6	116.9	96.29	111.9	118.8	117.3	96.76	112.4	119.5	117.1
<i>RIE(Lap)</i> (%)	87.31	104.3	111.6	110.1	87.43	104.6	111.7	111.5	87.61	104.8	111.6	111.7
<i>RIE(SBL)</i> (%)	77.95	80.74	83.68	84.29	77.19	80.22	83.55	84.30	78.26	79.21	83.04	84.01
<i>RIE(LeNet)</i> (%)	62.62	75.76	78.50	82.71	62.83	75.98	78.55	82.99	65.32	77.48	79.87	83.88
<i>RIE(Baseline)</i> (%)	49.65	62.11	65.71	73.73	58.60	65.61	70.53	77.04	64.24	73.49	76.96	82.03
<i>RIE(SADB-Net)</i> (%)	32.40	59.28	62.99	72.43	53.28	60.61	66.18	74.91	59.08	56.71	72.64	81.01
Speed(<i>L1</i>)(s)		0.05				0.05				0.05		
Speed(<i>Lap</i>)(s)		0.59				0.60				0.59		
Speed(<i>SBL</i>)(s)		12.63				13.09				12.91		
Speed(<i>LeNet</i>)(s)		0.22e-3				0.26e-3				0.25e-3		
Speed(<i>Baseline</i>)(s)		1.08e-3				1.08e-3				1.09e-3		
Speed(<i>SADB-Net</i>)(s)		1.83e-3				1.91e-3				1.92e-3		

Best results are highlighted in bold. Speed computes average model execution time per image.

Similar to the trend in Fig. 4.6, all methods show degraded performance with the increasing number of objects in the ROI, as reconstruction becomes more challenging. Fig. 4.8 further evaluates the performance of the given approaches under a wide range of SNR levels from 30dB to 70dB. It suggests all methods are generally robust to noise, with deep learning-based methods, i.e. LeNet, baseline and SADB-Net, yielding much better *RIE* than conventional methods. Overall, SADB-Net performs the best in terms of *RIE*. This implies that learning the structure- and conductivity-related information with separate branches helps effectively to discriminate conductivity levels among inclusions, compared with concatenated learning with simple network architectures.

Regarding the reconstruction time, we compute the average running time of all the given algorithms on all cases in the testing data set, a conventional approach adopted in K. He, Gkioxari, Dollár, and Girshick (2017). Deep learning-based approaches achieve high-quality image reconstruction results at a very fast speed, approximately 50 times faster than L1, 600 times faster than Lap, and 10,000 times faster than SBL. The LeNet consistently runs slightly faster than SADB-Net by 1.64ms, as it has a shallower structure, which costs slightly less computation for inferences. Nevertheless, the execution time of SADB-Net (below 2ms) is sufficiently good for implementing real-time EIT imaging.

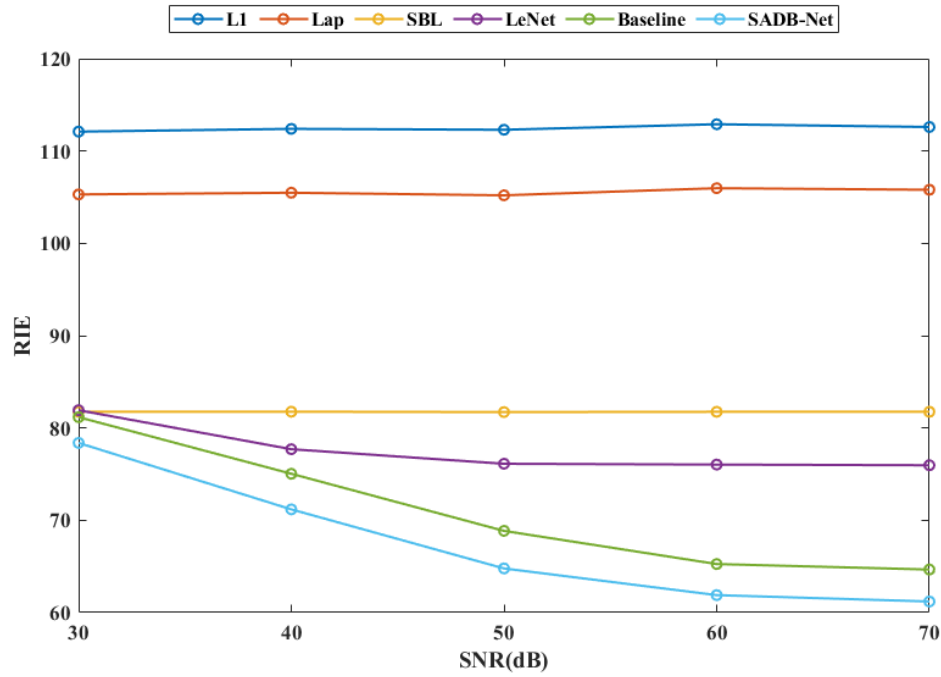


Figure 4.8: Noise robustness comparison in terms of *RIE*.

4.4.2 Evaluation on Experimental Data

In addition to the simulation study, we carried out real-world experiments on different miniature EIT sensors to examine the generalization ability of the proposed method. Image reconstruction on miniature EIT sensors is challenging due to their weak measurement signals and sensitivity to sensor imperfection. The miniature EIT sensor (Y. Yang et al., 2016) (see Fig. 4.9(a)) is equipped with 16 planar electrodes at the substrate and the inner diameter of the sensing chamber is 15 mm. We use cucumber, carrot, and potato cylinders with similar sizes but different conductivity values as imaging targets. The background substance is saline with a $0.25 \text{ S} \cdot \text{m}^{-1}$ conductivity. The excitation frequency is 20kHz. We also examined the performance of the given methods on MCF-7 human breast cancer cell spheroids with a quasi-2D miniature EIT sensor (Y. Yang, Wu, & Jia, 2018), which has a inner diameter of 14mm. The two MCF-7 human breast cancer cell spheroids with a diameter of 2mm are less conductive than the background substance. The parameter setting for all methods is the same as in the simulation.

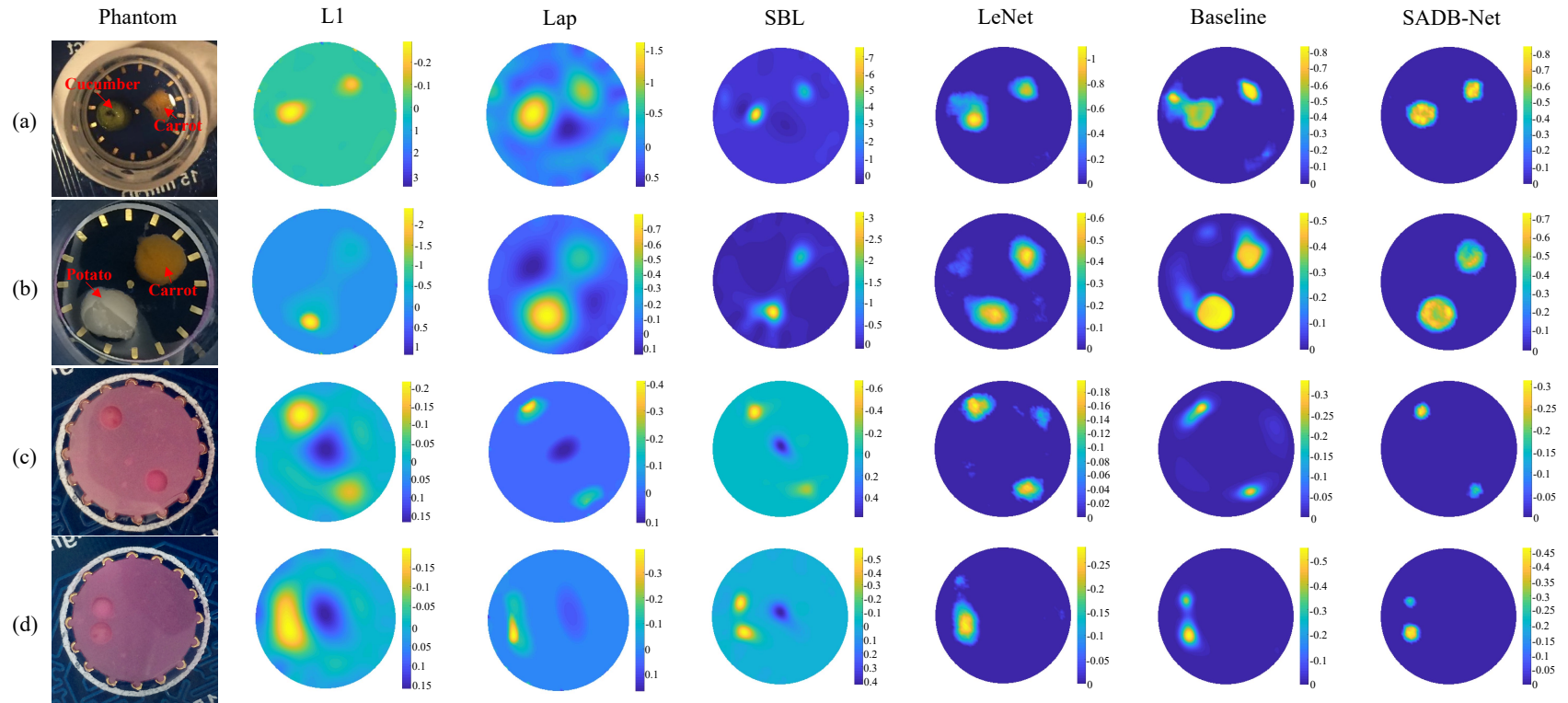


Figure 4.9: Experimental results on miniature EIT sensors. (a) Experiment phantom 1: cucumber and carrot cylinders. (b) Experiment phantom 2: potato and carrot cylinders. (c)-(d) Experiment phantom 3 and 4: two MCF-7 cell spheroids.

Fig. 4.9 illustrates the image reconstruction results of four phantoms. In experiment phantom 1, carrot has higher conductivity than cucumber, but both are lower than the background substance (Malone, Dos Santos, Holder, & Arridge, 2013). SBL could roughly recover such conductivity contrast but severely underestimates the size of both objects due to its strong sparsity constraint. Whilst L1, Lap, and LeNet could recover the shape of each object much better, but all generate significant artifacts (also can be found in simulations). The baseline even fails to tell either conductivity contrast or the target shape. SADB-Net performs better in terms of target shape and noise reduction whilst hardly reconstructing the conductivity contrast. In experiment phantom 2, the potato on the bottom-left corner induces a larger negative conductivity change than the carrot on the top-right corner (Malone et al., 2013). We can explicitly observe that L1 could hardly recover the top-right carrot cylinder, Lap suffers from significant artifacts, SBL underestimates target sizes, and LeNet and the baseline are unable to reconstruct the conductivity contrast. Differently, SADB-Net consistently outperforms the other approaches in shape preservation, conductivity contrast prediction and noise reduction. Based on Eq. (15) and the measured conductivity of carrot, potato and cucumber in Malone et al. (2013), we could deduct the relative conductivity changes of carrot, potato and cucumber under 20kHz are around -0.56, -0.76 and -0.81. By comparing the reconstructed images for experimental phantom 1 and phantom 2, we further confirm SADB-Net could better estimate both the conductivity change and the shape of imaging objects. Experiment phantom 3 and 4 contain two cell spheroids. L1, Lap, SBL and LeNet suffer from significant artifacts. They exhibit poor ability to distinguish the adjacent cell aggregates. SADB-Net yields consistently better shapes than the baseline. These results suggest that SADB-Net can generalize well to real experimental setups. Additionally, the unique architecture of SADB-Net makes a worthwhile contribution to accurate predictions of the structure and the conductivity difference between objects.

4.5 Summary

This chapter attempts to tackle the challenge of reconstructing the multi-object, multi-value conductivity distributions with EIT for tissue engineering applications. Typical convolutional networks (LeNet and the baseline model) run much faster than conventional approaches but are still unsatisfactory when estimating conductivity values. A novel network SADB-Net was proposed and demonstrated that:

1. by separating the estimation of structure distribution and conductivity values using two branches and then fusing the information together, SADB-Net could generate high-quality reconstructions of multi-object, multi-conductivity-value distributions with better structural and conductivity estimation;
2. SADB-Net exhibits good generalization ability based on the experimental results on miniature EIT sensors.

Multi-frequency Tissue Imaging with Model-based Learning

5.1 Introduction

Bioimpedance as an indicator of the physiological status of biological tissues varies with frequency. Therefore, different electrical properties between various tissues can be exploited to benefit physiological and pathological diagnostics for tissue differentiation, early cancer detection, and tumor or stroke imaging (A. Adler & Boyle, 2017; L. Yang et al., 2017). This motivates the development of multi-frequency EIT (mfEIT) (Y. Yang & Jia, 2017b), which measures the bio-impedances under different frequencies of interest and employs them to reconstruct a set of multi-frequency conductivity images related to tissue properties. The mfEIT-image-reconstruction problem concerns the simultaneous reconstruction of multiple conductivity images of selected frequencies. Existing algorithms generally require manual determination of regularization terms and fine-tuning hyper-parameters, such as penalty parameters and step sizes. In addition, the computational cost is considerable, preventing their wide adoption in biomedical applications that desire real-time imaging capability.

In this chapter, a model-based deep learning approach is developed to solve the mfEIT-image-reconstruction problem. The main target is to exploit intra- and inter-frequency dependencies to improve multi-frequency image quality. The proposed approach, named as MMV-Net, unrolls the iterative MMV-ADMM algorithm (M. Zhang et al., 2020) into a single pipeline (see Fig. 5.2). MMV-Net is composed of multiple blocks, each of which corresponds to one iteration. A deep network approximates and generalises the non-linear shrinkage operation in each block. MMV-Net fundamentally differs from ISTA-Net (J. Zhang & Ghanem, 2018) and FISTA-Net (Xiang et al., 2021). The main contributions are as follows:

1. A novel model-based deep learning approach is proposed for simultaneous mfEIT image reconstruction. The proposed MMV-Net tackles the inherent limitations of the conventional MMV-ADMM approach. Parameters across all iteration blocks are shared and learned through end-to-end training.

2. A dedicated network is developed to substitute the non-linear shrinkage operator, which learns a more general regularizer to incorporate spatial and frequency correlations between mfEIT images. The unique design could boost the reconstruction performance of mfEIT.
3. The proposed MMV-Net has much fewer parameters than the state-of-the-art model-based learning approaches, e.g. MoDL (Aggarwal, Mani, & Jacob, 2018) and FISTA-Net (Xiang et al., 2021) (by 12.8 and 8.5 times, respectively), making it easier to train even with a smaller dataset.
4. The *Edinburgh mfEIT Dataset* is constructed for mfEIT image reconstruction. The dataset mimics tissue engineering applications and comprises $4 \times 12,414$ randomly generated multi-object, multi-conductivity phantoms at four distinct frequencies.
5. MMV-Net is thoroughly evaluated on the *Edinburgh mfEIT Dataset* and various real-world experiments, and achieves superior reconstruction quality, convergence performance, and noise robustness, compared to state-of-the-art methods, such as MMV-ADMM (M. Zhang et al., 2020), MoDL (Aggarwal et al., 2018), and FISTA-Net (Xiang et al., 2021).

5.2 MMV-Net: A Model-based Learning Method

5.2.1 Multi-frequency EIT

Consider difference imaging of mfEIT (D. Liu et al., 2015), voltage changes $\Delta \mathbf{V} \in \mathbb{R}^{m \times l}$ at a set of excitation frequencies $\{f_1, f_2, \dots, f_l\}$ are measured to reconstruct the conductivity changes $\Delta \boldsymbol{\sigma} \in \mathbb{R}^{n \times l}$. The MMV model (Ziniel & Schniter, 2012) of mfEIT linearly approximates the relationship between $\Delta \mathbf{V}$ and $\Delta \boldsymbol{\sigma}$ by

$$\Delta \mathbf{V} = \mathbf{A} \Delta \boldsymbol{\sigma} \quad (5.1)$$

where $\mathbf{A} \in \mathbb{R}^{m \times n}$ ($m \ll n$) denotes the sensitivity matrix.

We define $\Delta \mathbf{V} = [\Delta \mathbf{v}_{f_1}, \Delta \mathbf{v}_{f_2}, \dots, \Delta \mathbf{v}_{f_l}]$, where $\Delta \mathbf{v}_{f_i} \in \mathbb{R}^{m \times 1}$ ($i = 1, \dots, l$) denotes the i^{th} column of $\Delta \mathbf{V}$. The first method to obtain voltage changes leverages Time-Difference (TD) measurements (Brown, 2003), i.e. $\Delta \mathbf{v}_{f_i} = \mathbf{v}_{f_i}(t_1) - \mathbf{v}_{f_i}(t_0)$, which requires mfEIT measurements at two time instants t_0 and t_1 , i.e. $\mathbf{v}_{f_i}(t_1)$, and $\mathbf{v}_{f_i}(t_0) \in \mathbb{R}^{m \times 1}$. Another prevailing method is to utilize Frequency-Difference (FD) measurements (Harrach & Seo, 2009). The FD approach employs voltage changes at different frequencies, i.e. $\Delta \mathbf{v}_{f_i} = \mathbf{v}_{f_i} - \mathbf{v}_{f_0}$, where f_0 is the reference frequency.

For convenience, we use \mathbf{B} and \mathbf{X} as substitutes for $\Delta \mathbf{V}$ and $\Delta \boldsymbol{\sigma}$ respectively in the rest of this chapter. Typically, the MMV model-based mfEIT image reconstruction problem can be solved by addressing the constrained optimization problem:

$$\begin{cases} \min_{\mathbf{X}} \mathcal{R}(\mathbf{X}) \\ s.t. \mathbf{A}\mathbf{X} = \mathbf{B} \end{cases} \quad (5.2)$$

where $\mathcal{R}(\cdot)$ denotes the regularization function, which encodes the *a priori* knowledge of the conductivity distribution \mathbf{X} . The MMV model uses the weighted $l_{2,1}$ regularization to promote the joint sparsity (Deng et al., 2013; M. Zhang et al., 2020):

$$\begin{cases} \min_{\mathbf{X}} \|\mathbf{X}\|_{w,2,1} := \sum_{i=1}^n w_i \|\mathbf{X}_i\|_2 \\ s.t. \mathbf{A}\mathbf{X} = \mathbf{B} \end{cases} \quad (5.3)$$

where $w_i (i = 1, \dots, n)$ is a positive scalar and \mathbf{X}_i is the i^{th} row of \mathbf{X} .

5.2.2 MMV-ADMM for mfEIT image reconstruction

The MMV-based mfEIT-image-reconstruction problem in (5.3) can be efficiently solved using the classic Alternating Direction Method of Multipliers (ADMM) (Fukushima, 1992; J. Wang et al., 2020). By introducing an auxiliary vector $\mathbf{Z} \in \mathbb{R}^{n \times l}$, the problem in (5.3) is equivalent to

$$\begin{cases} \min_{\mathbf{X}, \mathbf{Z}} \|\mathbf{Z}\|_{w,2,1} \\ s.t. \mathbf{Z} = \mathbf{X}, \mathbf{A}\mathbf{X} = \mathbf{B}. \end{cases} \quad (5.4)$$

The augmented Lagrangian problem of (5.4) is

$$\min_{\mathbf{X}, \mathbf{Z}} \left(\|\mathbf{Z}\|_{w,2,1} - \boldsymbol{\Lambda}_1^T (\mathbf{Z} - \mathbf{X}) + \frac{\beta_1}{2} \|\mathbf{Z} - \mathbf{X}\|_2^2 - \boldsymbol{\Lambda}_2^T (\mathbf{A}\mathbf{X} - \mathbf{B}) + \frac{\beta_2}{2} \|\mathbf{A}\mathbf{X} - \mathbf{B}\|_2^2 \right) \quad (5.5)$$

where $\boldsymbol{\Lambda} = \{\boldsymbol{\Lambda}_1 \in \mathbb{R}^{n \times l}, \boldsymbol{\Lambda}_2 \in \mathbb{R}^{m \times l}\}$ are Lagrangian multipliers and $\beta = \{\beta_1, \beta_2 > 0\}$ are penalty parameters. The ADMM is then applied to solve (5.5) through the following steps:

$$\begin{cases} \arg \min_{\mathbf{X}} \left(\boldsymbol{\Lambda}_1^T \mathbf{X} + \frac{\beta_1}{2} \|\mathbf{Z} - \mathbf{X}\|_2^2 - \boldsymbol{\Lambda}_2^T \mathbf{A}\mathbf{X} + \frac{\beta_2}{2} \|\mathbf{A}\mathbf{X} - \mathbf{B}\|_2^2 \right), \\ \arg \min_{\mathbf{Z}} \left(\|\mathbf{Z}\|_{w,2,1} - \boldsymbol{\Lambda}_1^T \mathbf{Z} + \frac{\beta_1}{2} \|\mathbf{Z} - \mathbf{X}\|_2^2 \right), \\ \boldsymbol{\Lambda}_1 \leftarrow \boldsymbol{\Lambda}_1 - \gamma_1 \beta_1 (\mathbf{Z} - \mathbf{X}), \\ \boldsymbol{\Lambda}_2 \leftarrow \boldsymbol{\Lambda}_2 - \gamma_2 \beta_2 (\mathbf{A}\mathbf{X} - \mathbf{B}), \end{cases} \quad (5.6)$$

where $\gamma = \{\gamma_1, \gamma_2 > 0\}$ are step lengths for the Lagrangian multipliers.

The first step in (5.6) is a convex quadratic problem, which has a closed-form solution:

$$\mathbf{X} = (\beta_1 \mathbf{I} + \beta_2 \mathbf{A}^T \mathbf{A})^{-1} (\beta_1 \mathbf{Z} - \boldsymbol{\Lambda}_1 + \beta_2 \mathbf{A}^T \mathbf{B} + \mathbf{A}^T \boldsymbol{\Lambda}_2) \quad (5.7)$$

where $\mathbf{I} \in \mathbb{R}^{n \times n}$ is an identity matrix.

To avoid large matrix inversion and reduce the computation cost, we in this work adopt the gradient descent method as a substitute for (5.7):

$$\mathbf{X} \leftarrow \mathbf{X} - \eta \nabla_{\mathbf{X}; \mathbf{Z}, \Lambda_1, \Lambda_2} \quad (5.8)$$

where η is the step size, and $\nabla_{\mathbf{X}; \mathbf{Z}, \Lambda_1, \Lambda_2}$ is the gradient of the first step in (5.6) with respect to \mathbf{X} given $\{\mathbf{Z}, \Lambda\}$, which is defined by:

$$\nabla_{\mathbf{X}; \mathbf{Z}, \Lambda_1, \Lambda_2} = (\beta_1 \mathbf{I} + \beta_2 \mathbf{A}^T \mathbf{A}) \mathbf{X} - (\beta_1 \mathbf{Z} - \Lambda_1 + \beta_2 \mathbf{A}^T \mathbf{B} + \mathbf{A}^T \Lambda_2) \quad (5.9)$$

Thus, to solve (5.4) with ADMM, we have the following updates at the k^{th} iteration:

$$\begin{cases} \mathbf{X}^{(k)} = \mathbf{X}^{(k-1)} - \eta \nabla_{\mathbf{X}^{(k-1)}; \mathbf{Z}^{(k-1)}, \Lambda_1^{(k-1)}, \Lambda_2^{(k-1)}}, & (5.10a) \\ \mathbf{Z}^{(k)} = \mathcal{S}(\mathbf{X}^{(k)} + \frac{1}{\beta_1} \Lambda_1^{(k-1)}, \frac{w}{\beta_1}), & (5.10b) \\ \Lambda_1^{(k)} = \Lambda_1^{(k-1)} + \gamma_1 \beta_1 (\mathbf{X}^{(k)} - \mathbf{Z}^{(k)}), & (5.10c) \\ \Lambda_2^{(k)} = \Lambda_2^{(k-1)} + \gamma_2 \beta_2 (\mathbf{B} - \mathbf{A} \mathbf{X}^{(k)}), & (5.10d) \end{cases}$$

where $k \in \{1 \dots K_s\}$ is the iteration index, and $\mathcal{S}(\cdot)$ represents a row-wise shrinkage operator associated with the weighted $l_{2,1}$ regularization:

$$\mathbf{z}_i^{(k)} = \max \left\{ \left\| \mathbf{x}_i^{(k)} + \frac{1}{\beta_1} (\Lambda_1)_i^{(k-1)} \right\|_2 - \frac{w_i}{\beta_1}, 0 \right\}. \quad (5.11)$$

$$\frac{\mathbf{x}_i^{(k)} + \frac{1}{\beta_1} (\Lambda_1)_i^{(k-1)}}{\left\| \mathbf{x}_i^{(k)} + \frac{1}{\beta_1} (\Lambda_1)_i^{(k-1)} \right\|_2}, \text{ for } i = 1, \dots, n.$$

This work proposes to approximate $\mathcal{S}(\cdot)$ through the data-driven method. Instead of directly applying (5.11) only to promote the joint sparsity, MMV-Net aims to learn a more general $\mathcal{S}(\cdot)$ to exploit both the spatial correlation and the inherent correlation across different frequencies (see illustration in Fig. 5.1), to reconstruct the multi-frequency conductivity distributions effectively and simultaneously.

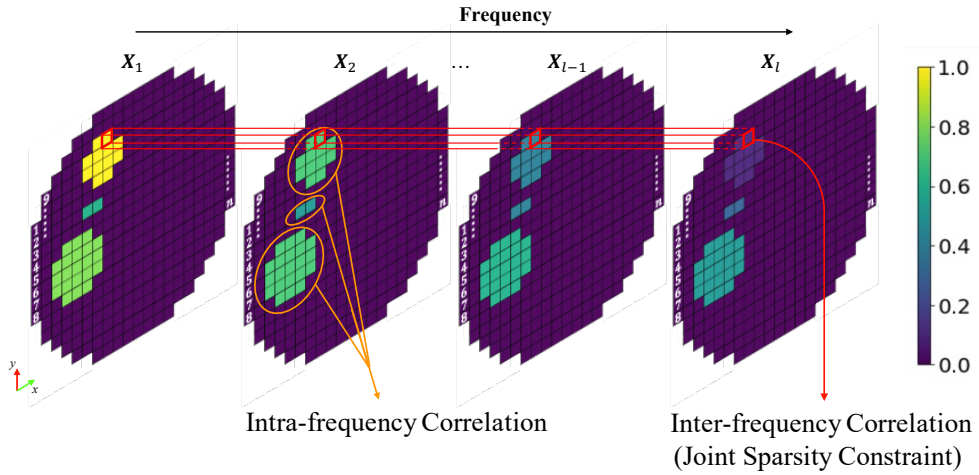


Figure 5.1: Illustration of intra- and inter-frequency correlation between mfEIT images.

5.2.3 MMV-Net for mfEIT image reconstruction

For the mfEIT-image-reconstruction problem, the conventional ADMM (MMV-ADMM) has limitations in three respects: a) typically it requires hundreds of iterations to achieve the optimum, which degrades the computational efficiency to a significant extent (Qu, Nasrabadi, & Tran, 2013; M. Zhang et al., 2020); b) the non-linear shrinkage operator $\mathcal{S}(\cdot)$ is only valid for specific image patterns (e.g. sparsity (Cotter, Rao, Engan, & Kreutz-Delgado, 2005), group sparsity (M. Zhang et al., 2020)); c) it is non-trivial to fine-tune the algorithm parameters $\{\beta, \gamma, \eta\}$.

To address the above issues, we propose a deep architecture named MMV-Net for mfEIT image reconstruction by unrolling the iterative MMV-ADMM algorithm. MMV-Net combines the model-based method and the deep neural network for mfEIT image reconstruction to exploit advantages from both sides. We map the four update procedures in (5.10a)-(5.10d) into an unfolded data flow with K_s iterations as illustrated in Fig. 5.2.

Algorithm : MMV-ADMM for mfEIT Image Reconstruction

Input : mfEIT measurement data \mathbf{B} .

Initialize : $\mathbf{X}^{(0)}$ using (12), $\mathbf{Z}^{(0)} = \mathbf{0}$, $\Lambda_1^{(0)} = \mathbf{0}$, $\Lambda_2^{(0)} = \mathbf{0}$.

for $k = 1, 2, \dots, K_s$ **do**

Update $\mathbf{X}^{(k)}$ using (5.10a);
 Update $\mathbf{Z}^{(k)}$ using (5.10b);
 Update $\Lambda_1^{(k)}$ using (5.10c);
 Update $\Lambda_2^{(k)}$ using (5.10d).

end for

Output : Estimated multi-frequency images $\mathbf{Z}^{(K_s)}$.

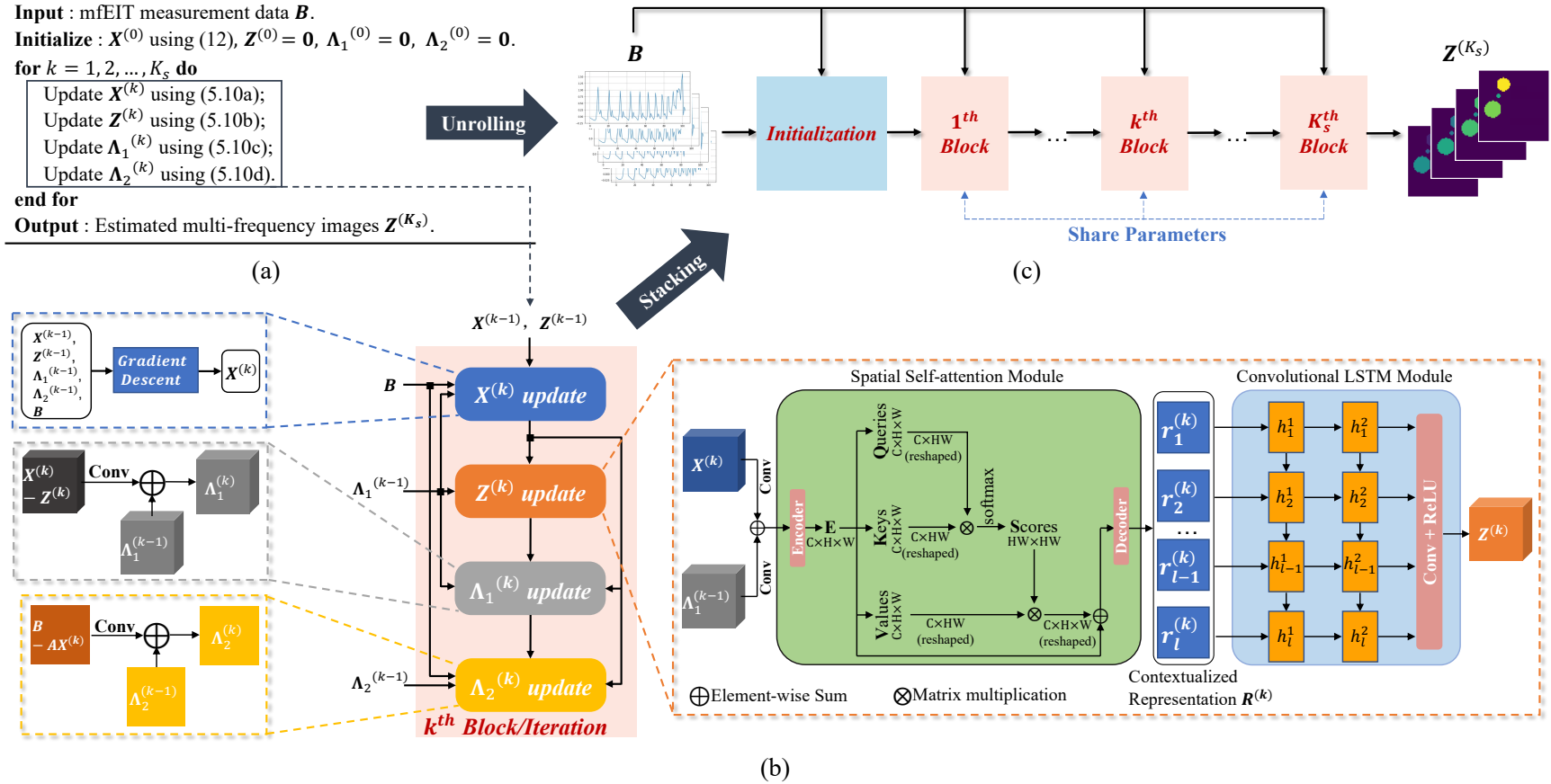


Figure 5.2: (a) The iterative MMV-ADMM algorithm. (b) Illustration of the four updating steps at the k^{th} iteration corresponding to (5.10a)-(5.10d). (c) The overall architecture of the proposed MMV-Net. MMV-Net is an unrolled architecture for K_s iterations. It alternates among the four update steps. These update steps share parameters across all iterations.

The input of the MMV-Net is the mfEIT measurement data \mathbf{B} . $\mathbf{Z}^{(0)}$, $\mathbf{\Lambda}_1^{(0)}$, and $\mathbf{\Lambda}_2^{(0)}$ are initialized as zeros. $\mathbf{X}^{(0)}$ is obtained by employing the one-step Gauss-Newton solver with the Laplacian filter (A. Adler et al., 2009):

$$\mathbf{X}^{(0)} = (\mathbf{A}^T \mathbf{A} + \lambda \mathbf{L}^T \mathbf{L})^{-1} \mathbf{A}^T \mathbf{B} \quad (5.12)$$

where \mathbf{L} is the Laplacian matrix, and λ is the regularization factor. The initialization results are then utilized to generate the final multi-frequency conductivity images $\mathbf{Z}^{(K_s)}$ after K_s iterations. The subsequent part of MMV-Net comprises of K_s blocks, where the k^{th} block corresponds to the k^{th} iteration of the MMV-ADMM algorithm. Each block consists of four update steps corresponding to one iteration of MMV-ADMM in (5.10a)-(5.10d), including gradient descent (\mathbf{X}) update, auxiliary variable (\mathbf{Z}) update, the first multiplier ($\mathbf{\Lambda}_1$) update, and the second multiplier ($\mathbf{\Lambda}_2$) update. The following parts discuss the four update steps at the k^{th} iteration in detail.

$\mathbf{X}^{(k)}$ update

This update step implements the gradient descent method. It generates the immediate result $\mathbf{X}^{(k)}$. Given $\mathbf{X}^{(k-1)}$, $\mathbf{Z}^{(k-1)}$, $\mathbf{\Lambda}_1^{(k-1)}$, and $\mathbf{\Lambda}_2^{(k-1)}$, which are obtained from the previous $(k-1)^{th}$ iteration, the output $\mathbf{X}^{(k)}$ is computed according to (5.10a).

$\mathbf{Z}^{(k)}$ update

This step updates the auxiliary variable by unrolling the generalized non-linear operator $\mathcal{S}(\cdot)$ in (5.10b), where the prior knowledge is integrated. For mfEIT, it is crucial to learn intra- and inter-image correlations simultaneously with respect to frequency channels (see Fig. 5.1). With this purpose, we propose to design $\mathcal{S}(\cdot)$ as a deep neural network, in particular, a cascade of a Spatial Self-Attention (SSA) module and a Convolutional Long Short-Term Memory (ConvLSTM) module. Fig. 5.2(b) illustrates how (5.10b) is mapped into a network. First, a more general combination of $\mathbf{X}^{(k)}$ and $\mathbf{\Lambda}_1^{(k-1)}$ is learned by two $1 \times 1 \times 1$ convolutional layers respectively and an element-wise sum. Afterwards, we apply the SSA and ConvLSTM to improve the reconstruction performance of $\mathbf{Z}^{(k)}$. Let $Conv_1(\cdot)$ and $Conv_2(\cdot)$ be the two convolutional layers, $\mathcal{F}_{SSA}(\cdot)$ and $\mathcal{F}_{LSTM}(\cdot)$ be the function of SSA and ConvLSTM, respectively, then (5.10b) can be reformulated as:

$$\mathbf{Z}^{(k)} = \mathcal{F}_{LSTM}(\mathcal{F}_{SSA}(Conv_1(\mathbf{X}^{(k)}) + Conv_2(\mathbf{\Lambda}_1^{(k-1)}))) \quad (5.13)$$

The detailed design of the SSA and ConvLSTM is elaborated as follows.

Spatial self-attention module $\mathcal{F}_{SSA}(\cdot)$: our previous work (Z. Chen et al., 2020) observed that by explicitly learning the structural information of the conductivity image, significant image quality improvement can be achieved in terms of spatial resolution and accuracy. This idea is inherited by using a spatial self-attention module to determine the structural information under each frequency channel to extract inter-frequency correlations.

The family of attention modules is capable of modeling long-range dependencies in natural language processing and computer vision. As a variation of attention, the self-attention mechanism was first proposed to extract global dependencies of inputs for machine translation (Vaswani et al., 2017). X. Wang, Girshick, Gupta, and He (2018) and Fu et al. (2019) extended the self-attention mechanism to video classification and image segmentation, respectively. Self-attention is usually inserted in a network and generates importance maps to refine the high-level feature maps. As a result, important regions can be focused on and feature representations are enriched with contextual relationships for intra-image compactness.

Inspired by the self-attention mechanism, the proposed SSA adopts the structure of a symmetric encoder–decoder network, embedded with a self-attention mechanism to the encoder output. An encoder typically comprises a stack of convolutional layers with activation layers to extract latent feature representations. For instance, X. Wang et al. (2018) and Fu et al. (2019) employed the pre-trained ResNet (K. He, Zhang, Ren, & Sun, 2016) as the backbone. Q. He, Sun, Yan, and Fu (2021) used a lightweight backbone based on ShuffleNetV2 (Ma, Zhang, Zheng, & Sun, 2018) followed by a deformable context feature pyramid network to improve the adaptive capability of multiscale features. As the reconstructed mfEIT images under all frequencies share the same structure, the encoder part first introduces a 3×3 convolutional layer producing one output channel. Then, we apply two 2×2 convolutional layers with a stride of 2. Each layer is followed by a Batch Normalization layer and an ELU layer. The encoder outputs a feature representation \mathbf{E} with the size of $C \times H \times W$, which is fed into three 3×3 convolutional layers to generate feature maps queries \mathbf{Q} , keys \mathbf{K} and values \mathbf{V} , respectively. \mathbf{Q} , \mathbf{K} and \mathbf{V} now have the size as \mathbf{E} . They are all reshaped to $C \times P$, where $P = H \times W$. \mathbf{Q} and \mathbf{K} are multiplied and fed into a softmax layer to generate a score/attention map \mathbf{S} with the size of $P \times P$. Afterwards \mathbf{S} and \mathbf{V} are multiplied and reshaped back to $C \times H \times W$. We then perform residual learning through a skip connection to \mathbf{E} . Finally, the decoder is applied and comprises two 2×2 deconvolutional layers with a stride of 2, each followed by a BatchNorm layer and an ELU layer. The final output is the contextualized representation of structure information $\mathbf{R}^{(k)} \in \mathbb{R}^{m \times l}$.

Convolutional LSTM module $\mathcal{F}_{LSTM}(\cdot)$: based on the structure information $\mathbf{R}^{(k)}$, we then attempt to learn the inter-frequency correlations by reconstructing the trend of the varying conductivity contrast along the frequency domain, meanwhile preserving the general structures learned from the SSA.

We view the contextualized representation $\mathbf{R}^{(k)}$ as a set of sequential images, i.e. $\{\mathbf{r}_i^{(k)}\}_{i=1}^l$, where $\mathbf{r}_i^{(k)} \in \mathbb{R}^m$ represents the i^{th} column of $\mathbf{R}^{(k)}$. To tackle this sequence-to-sequence (seq2-seq) problem, Recurrent Neural Network (RNN) and LSTM models (Cho et al., 2014; Donahue et al., 2015) are in a dominant position in the field of deep learning. One drawback of RNNs/LSTMs is that they require considerable memory to store intermediate cell gate parameters, especially for long sequences and high dimensional inputs, on account of the usage of full connections. Though powerful enough to capture temporal correlations, the fully-connected layers raise redundancy and distortion for spatial data. In contrast, Convolutional LSTM (ConvLSTM) (Shi et al., 2015) is more computationally efficient as it replaces the fully-connected layers with convolutional layers. This operation further preserves spatial correlations with much fewer parameters and better generalization, meaning we could employ more parameters to construct the SSA.

To learn the changes of conductivity contrast along with the frequency, we take advantage of ConvLSTMs. The proposed ConvLSTM module has a stack of multiple ConvLSTM layers with a kernel size of 3×3 . We set the layer number as two by default. We finally apply an additional 1×1 convolutional layer and a ReLU layer to generate $\mathbf{Z}^{(k)}$.

$\Lambda_1^{(k)}$ update

The multiplier update step corresponds to (5.10c). As shown in Fig. 5.2(b), the residual $(\mathbf{X}^{(k)} - \mathbf{Z}^{(k)})$ first goes through a $1 \times 1 \times 1$ convolutional layer, which is expected to learn $\gamma_1 \beta_1$. Then we perform an element-wise sum operation between the residual and $\mathbf{Z}^{(k-1)}$ to obtain the output $\Lambda_1^{(k)}$.

$\Lambda_2^{(k)}$ update

Fig. 5.2(b) also illustrates the multiplier update according to (5.10d) with inputs of $\Lambda_2^{(k-1)}$ and $(\mathbf{B} - \mathbf{A}\mathbf{X}^{(k)})$. Similar to the update of Λ_1 , we decompose this operation to a 1×1 convolutional layer to learn the product $\gamma_2 \beta_2$ and an element-wise sum to generate $\Lambda_2^{(k)}$.

Given a training dataset \mathcal{D} with $N_{\mathcal{D}}$ pairs of samples, we define the objective function as the Mean Square Error (MSE) between the predicted images $\mathbf{Z}^{(K_s)}$ and the ground truth $\mathbf{X}^{(gt)}$:

$$\mathcal{L} = \frac{1}{N_{\mathcal{D}}} \sum_{(\mathbf{B}, \mathbf{X}^{(gt)}) \in \mathcal{D}} \left\| \mathbf{Z}^{(K_s)} - \mathbf{X}^{(gt)} \right\|^2. \quad (5.14)$$

5.2.4 Network Training

We train the MMV-Net using PyTorch and employ Adam (Kingma & Ba, 2014) for optimization with the batch size of 6. Similar to Aggarwal et al. (2018); Xiang et al. (2021); Y. Yang, Sun, et al. (2018); J. Zhang and Ghanem (2018), the non-linear operator and parameters $\Theta = \{Conv_1(\cdot), Conv_2(\cdot), \mathcal{F}_{SSA}(\cdot), \mathcal{F}_{LSTM}(\cdot), \beta, \gamma, \eta\}$ are all learned from training data, rather than hand-tuning. We employ the parameter-sharing strategy to penalize the recursive network size for effective learning, where Θ of the MMV-Net is shared across all iterations. Inspired by the training approach in Aggarwal et al. (2018), we adopt a three-step approach for training. We first train the auxiliary variable update (\mathbf{Z}) to learn $\Theta_{\mathbf{Z}} = \{Conv_1(\cdot), Conv_2(\cdot), \mathcal{F}_{SSA}(\cdot), \mathcal{F}_{LSTM}(\cdot)\}$. Then we train the entire parameters Θ for only one iteration, initialized with the previously learned parameters $\Theta_{\mathbf{Z}}$. The trained parameters Θ with a single iteration serve as a starting point for training the MMV-Net with multiple iterations.

5.3 Experiments and Results

5.3.1 The Edinburgh mfEIT Dataset

We constructed the *Edinburgh mfEIT Dataset* (the dataset is available at <https://datashare.ed.ac.uk/handle/10283/4441>) to train the proposed MMV-Net. It contains multiple imaging objects with continuously varying conductivity values along four frequencies ($l = 4$) within a circular 16-electrode EIT sensor. The forward problem was solved by using COMSOL Multiphysics and Matlab. We adopt the adjacent measurement strategy (Brown & Seagar, 1987) and a completed non-redundant measurement cycle contains $m = 104$ voltage measurements. In solving the inverse problem, we divide the circular sensing region by a 64×64 quadrate mesh, which contains $n = 3228$ pixels.

The background substance is saline with a constant conductivity of $2 S/m$, which does not change with frequency. One to three circular objects are simulated with their diameters randomly determined by the uniform distribution $[0.05d, 0.3d]$ (d is the sensor diameter). Extra constraints are imposed to avoid overlap within the sensing region. We then design three possible groups of increasing conductivity values associated with the four frequencies as shown in Table 5.1, from which the changing conductivity values of target objects along frequency are assigned randomly. A distinct conductivity group is further ensured for each circular object within a phantom. This setup was adopted to simulate potential target application scenarios in tissue engineering (e.g. cell culture imaging (Z. Chen et al., 2020)).

Table 5.1: Groups of simulated conductivity values at different frequencies.

Group Index	f_1 (S/m)	f_2 (S/m)	f_3 (S/m)	f_4 (S/m)
1	0.01	0.6	1.2	1.8
2	0.4	0.6	0.8	1.0
3	0.8	1.0	1.2	1.4

A total of $4 \times 12,414$ (where 4 is the number of current frequencies) pairs of voltage-conductivity samples were generated through finite element modelling simulation. Considering phantom complexity, we generated $4 \times 3k$ one-object samples, $4 \times 4k$ two-object samples, $4 \times 5,414$ three-object samples. They are partitioned into $4 \times 8,700$ training set, $4 \times 1,900$ validation set, and $4 \times 1,814$ testing set for network training.

To eliminate the influence of systematic defect, we calibrate and normalize the voltage measurements and conductivity in the dataset, following:

$$\mathbf{B} = \frac{\mathbf{V}_{mea} - \mathbf{V}_{ref}}{\mathbf{V}_{ref}}, \quad (5.15)$$

$$\mathbf{X} = \frac{\boldsymbol{\sigma}_{mea} - \boldsymbol{\sigma}_{ref}}{\boldsymbol{\sigma}_{ref}}, \quad (5.16)$$

where $\boldsymbol{\sigma}_{ref}$ and \mathbf{V}_{ref} denote the reference conductivity distributions and corresponding measurement data respectively with only background substance (discussed in Section 5.2.1); $\boldsymbol{\sigma}_{mea}$ and \mathbf{V}_{mea} denote respectively the conductivity distribution and measurement with perturbations.

5.3.2 Evaluation on Simulation Data

In this sub-section, we evaluate the performance of the proposed MMV-Net using simulated mfEIT data.

Performance Comparison

We compare the proposed MMV-Net with three state-of-the-art image-reconstruction methods for mfEIT, i.e. MMV-ADMM (M. Zhang et al., 2020), MoDL (Aggarwal et al., 2018), and FISTA-Net (Xiang et al., 2021) on the *Edinburgh mfEIT Dataset*. MMV-ADMM is a conventional MMV-based method with the ADMM solver that can be adjusted and applied for mfEIT image reconstruction. MoDL and FISTA-Net are model-based deep learning methods targeted at single measurement vector-based tomographic imaging. MoDL unrolls the traditional ADMM algorithm, while FISTA-Net is based on the FISTA framework (Beck & Teboulle, 2009). The number of trainable parameters of the latter two model-based deep learning methods is given in the last row of Table 5.2.

Table 5.2: Performance comparisons (PSNR, SSIM and RMSE) on the *Edinburgh mfEIT Dataset*.

Metrics	Frequency Channel	MMV-ADMM	MoDL	FISTA-Net	MMV-Net
PSNR	1	19.3950	21.4738	21.4444	23.7423
	2	22.0398	24.1978	24.4338	26.1284
	3	24.3093	26.1114	26.6960	28.5507
	4	26.6077	27.0675	27.6000	28.6125
	<i>Average</i>	23.0880	24.7126	25.0435	26.7585
SSIM	1	0.4347	0.8467	0.8784	0.9354
	2	0.5266	0.8676	0.9092	0.9312
	3	0.6175	0.8712	0.9182	0.9469
	4	0.6383	0.8569	0.9092	0.9265
	<i>Average</i>	0.5543	0.8606	0.9038	0.9350
RMSE	1	0.1175	0.0910	0.0933	0.0700
	2	0.0836	0.0651	0.0644	0.0527
	3	0.0650	0.0526	0.0499	0.0404
	4	0.0549	0.0512	0.0496	0.0407
	<i>Average</i>	0.0803	0.0650	0.0643	0.0510
No. of learning parameters		NA	112,517	75,045	8,780

Best results are highlighted in bold.

Table 5.2 shows quantitative comparison based on the average Peak Signal to Noise Ratio (PSNR), Structural Similarity Index Measure (SSIM), and Root Mean Square Error (RMSE) on all the testing data. MMV-Net outperforms all competing approaches at all frequencies. Note that there is an explicit improvement of PSNR, SSIM and RMSE from f_1 to f_4 . This is due to the higher sensitivity of these metrics to larger conductivity contrasts.

Fig. 5.3 demonstrates reconstructions of two simulated phantoms for qualitative comparison. In the following work, qualitative results are presented in square images by doing zero padding outside the circular sensing region. MMV-ADMM can hardly reconstruct lower conductivity contrasts, especially at f_3 and f_4 , whereas MoDL and FISTA-Net perform better. In contrast, the proposed MMV-Net can restore the most consistent structures/shapes and the conductivity changes along the frequency domain more smoothly. In addition, MMV-Net can distinguish fairly close objects more effectively than the other methods, which demonstrates the advantages of SSA and ConvLSTM used in MMV-Net. However, all methods failed to yield accurate conductivity values for each object. Even the best-performing MMV-Net tends to assign similar values to all objects, although the shapes estimated are close to the ground truth. The potential reason is that the approximated linearization in (5.1) is unable to handle such non-linear circumstances, i.e. the sensitivity matrix \mathbf{A} suffers from errors when interpreting conductivity levels from the measurement data.

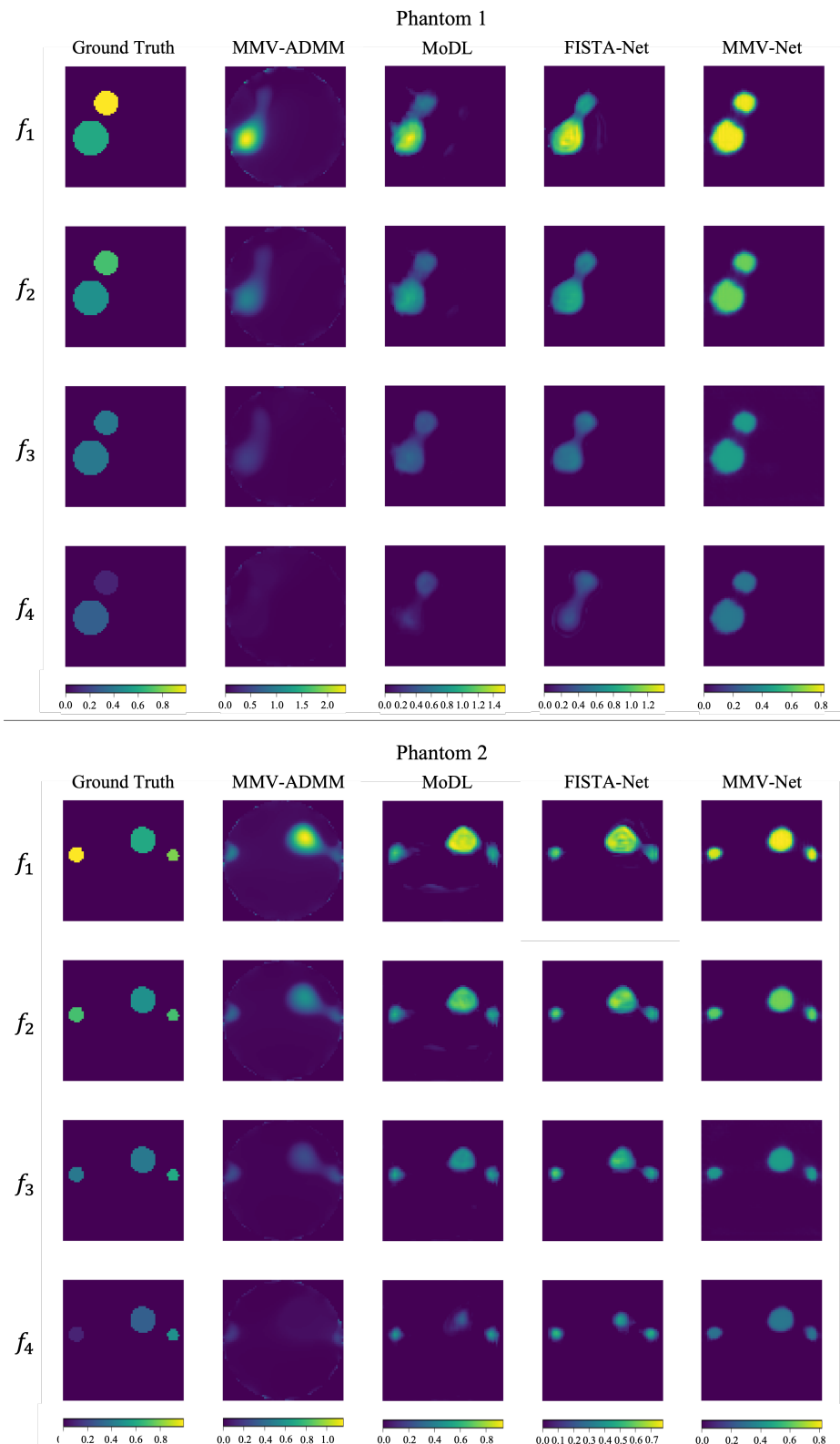


Figure 5.3: Comparison of the proposed MMV-Net with the state-of-the-art imaging approaches on two simulated phantoms in the testing set.

Fig. 5.4 shows two typical failure cases of MMV-Net. For case 1, MMV-Net fails to reconstruct the smallest object closely positioned to two larger objects. Case 2 contains a noticeable artifact at the center of the reconstructed images of each frequency. This artifact is possibly inherited from the one-step initialization, indicating that the quality of the initial guess may also affect the final reconstruction.

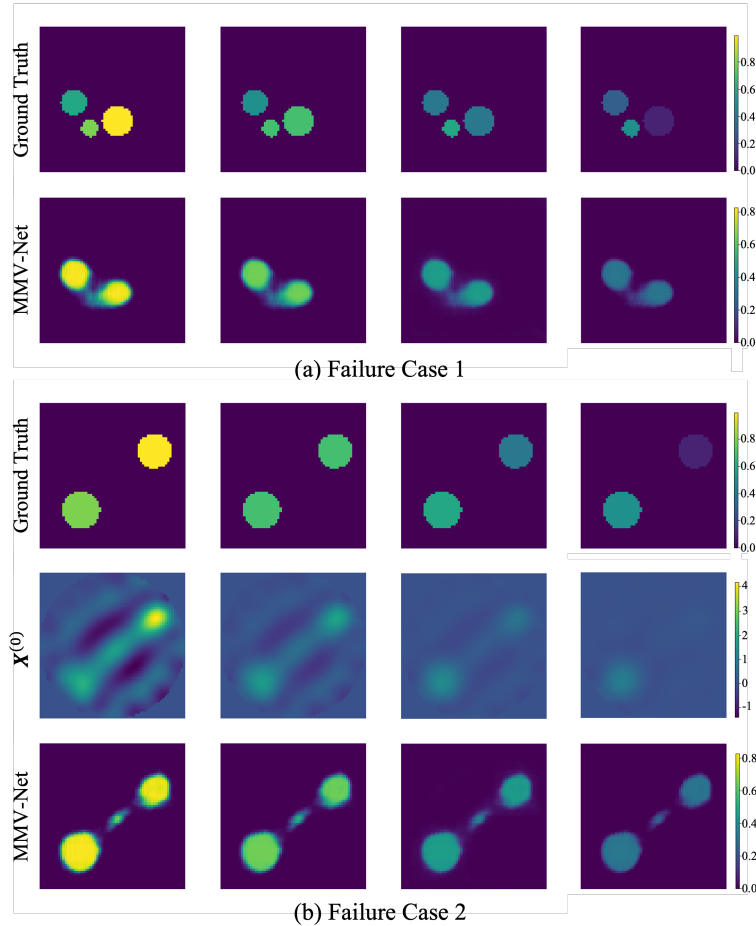


Figure 5.4: Two failure cases of MMV-Net.

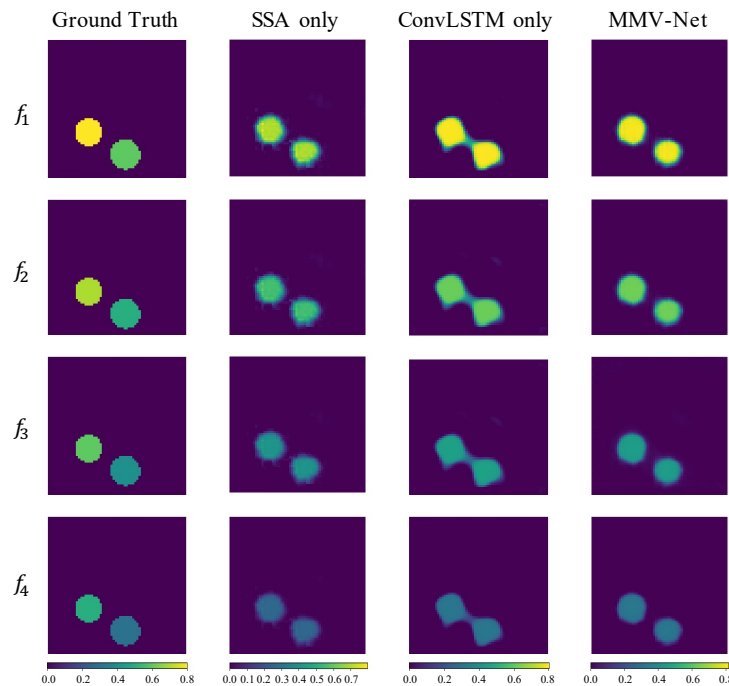
Ablation Studies

In MMV-Net, we employ a Spatial Self-Attention (SSA) Module and a Convolutional LSTM (ConvLSTM) Module to capture intra- and inter-frequency correlations for high-performance mfEIT reconstructions. To verify the performance of the two modules, we conduct ablation studies (see Table 5.3). MMV-Net with only the ConvLSTM module outperforms MMV-Net with individually the SSA module by 6% in PSNR, 22% in SSIM, and 15% in RMSE. Integration of the two modules into MMV-Net brings further improved performance of 26.9817 dB in PSNR, 0.9364 in SSIM, and 0.0498 in RMSE.

Table 5.3: Ablation study on the validation set. (SSA: Spatial Self-attention Module; ConvLSTM: Convolutional LSTM Module.)

Method	SSA	ConvLSTM	PSNR	SSIM	RMSE
MMV-Net	✓		24.9132	0.7640	0.0622
		✓	26.5144	0.9300	0.0530
	✓	✓	26.9817	0.9364	0.0498

Fig. 5.5 illustrates the visual effects of the two modules. As expected, the SSA module itself manages to split the two objects and provide rough shapes but relatively vague boundaries, whereas the ConvLSTM module enhances the continuity but focuses less on shapes. By taking advantage of both modules, the proposed MMV-Net demonstrates superior performance among all the given approaches.

**Figure 5.5:** An example of image reconstruction results from ablation study.

Iteration Analysis

Table 5.4 shows the impact of the iteration number K_s . It can be observed that average PSNR, SSIM, and RMSE values on the validation set are improved with increasing iterations. These improvements slow down considerably when $K_s \geq 7$. Therefore, we use $K_s = 7$ for configuration as a compromise of performance and computational cost.

Table 5.4: Improvement in reconstruction quality on validation data with the increasing number of iterations of the network.

No. of Iterations	5	6	7	8	9
PSNR	26.8428	26.9422	26.9817	27.0174	27.0177
SSIM	0.9341	0.9342	0.9364	0.9391	0.9394
RMSE	0.0506	0.0501	0.0498	0.0496	0.0496

We show the intermediate reconstructed images of MMV-Net, FISTA-Net and MMV-ADMM at different iterations in Fig. 5.6. Each row corresponds to an iteration under different frequencies. The reconstruction quality of MMV-Net improves gradually with iteration. More specifically, details in the structural information are clearer and more accurate while tiny changes in conductivity values raise as it goes deeper. It might be because we put more parameters in the SSA modules to learn the structural information.

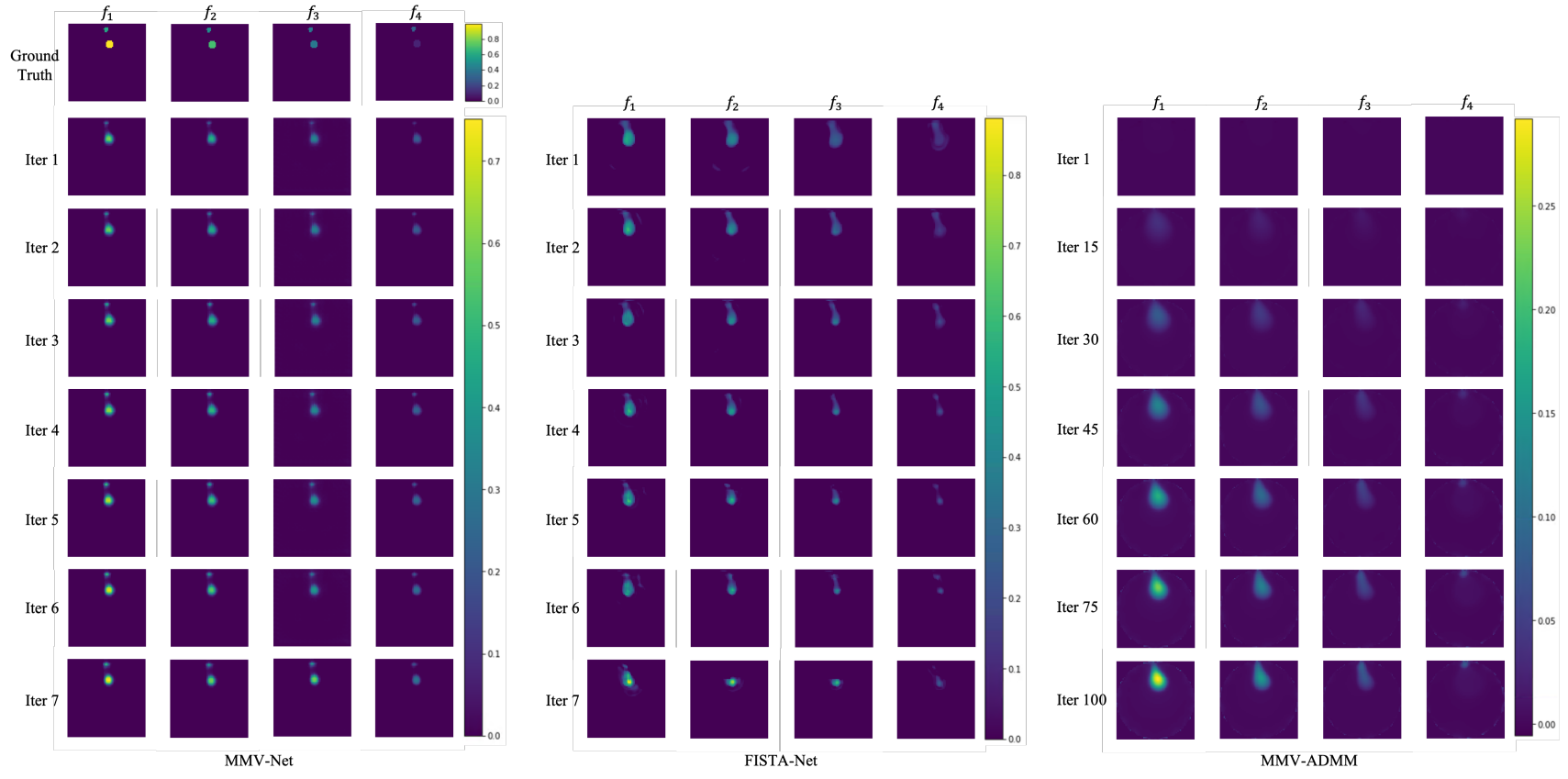


Figure 5.6: Intermediate reconstructed images by MMV-Net, FISTA-Net and MMV-ADMM at different iterations.

Generalization Ability

We demonstrate the generalization ability of MMV-Net by adding different levels of Gaussian noise to the measurement data and evaluating the image quality based on PSNR. Fig. 5.7 shows the average PSNR values of different methods. Degraded performance can be observed for all methods, whilst the proposed MMV-Net is the most robust against noise and FISTA-Net suffers a rapid decay. MoDL and FISTA-Net are more robust than MMV-ADMM with lower noise levels (e.g. 45dB) but MMV-ADMM exceeds both MoDL and FISTA-Net when the SNR is smaller than around 37dB.

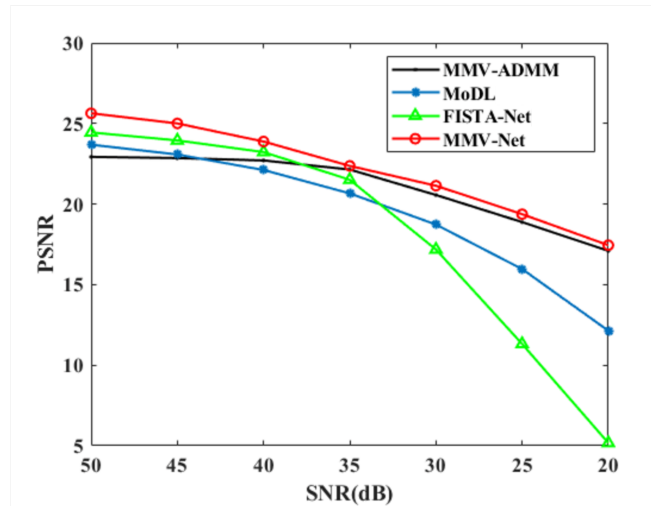


Figure 5.7: Generalization ability study of different noise levels.

However, it is worth mentioning that all three learning-based methods are trained with only noise-free data. We believe our MMV-Net will retain more advantage upon MMV-ADMM and the other two model-based learning approaches should demonstrate more robustness to noise if sufficient noisy data are added in the training stage.

Convergence Performance

Fig. 5.8 illustrates the convergence performance of MMV-ADMM, MoDL, FISTA-Net, and MMV-Net. MMV-ADMM runs 100 iterations and ultimately converges to a certain level, while much faster convergence can be achieved by all network-based approaches. They adopt only 7 iterations and saturate at a much lower RMSE. We also observe that FISTA-Net shows smoother convergence than MoDL though they finally stop at similar values. MMV-Net converges even faster than MoDL and FISTA-Net.

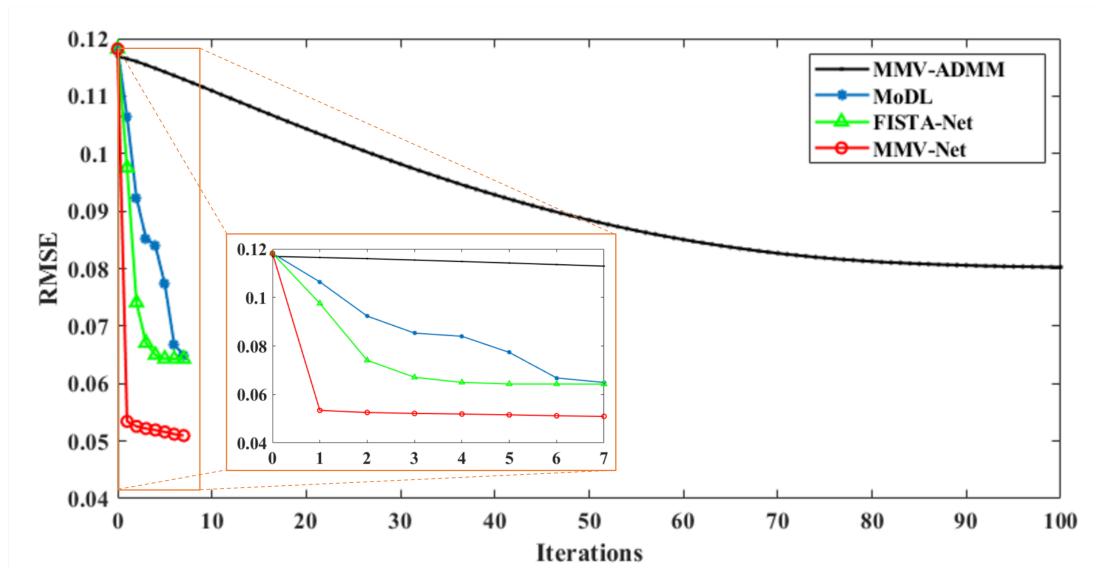


Figure 5.8: Convergence performance analysis on the testing set.

5.3.3 Computational Complexity Evaluation

Table 5.5 compares the model size and running speed of MMV-ADMM, MoDL, FISTA-Net, and MMV-Net as indicators for computational complexity. MMV-Net has the smallest model size while obtaining the best performance. In terms of FPS, MMV-ADMM is faster than MoDL and competitive to FISTA-Net, showing the advancement of the MMV model compared to the SMV model. The proposed MMV-Net achieves the highest model execution speed of 7.92 ft/s, making it suitable for real-time imaging. MMV-Net also achieves the lowest floating-point operations, which benefits from the lightweight backbone.

Table 5.5: Complexity evaluation. FPS means frame per second. FLOPS means floating point operations per second

Method	Model Size (MB)	FPS	FLOPS
MMV-ADMM	-	1.39	-
MoDL	0.46	0.48	12.93
FISTA-Net	0.32	1.87	12.91
MMV-Net	0.06	7.92	0.04

Best results are highlighted in bold.

5.3.4 Evaluation on Experimental Data

In addition to the simulation study, we carried out real-world experiments on two different EIT sensors (Z. Chen et al., 2020; Y. Yang & Jia, 2017b) to examine the generalization ability of the proposed method. The inner diameter of the first 16-electrode EIT sensor is 94 mm. We use a potato cylinder, a sweet potato cylinder, a metal cylinder and a plastic cylinder with different conductivity values as imaging targets. Fig. 5.9(a)-(f) show pictures and corresponding geometric distributions of the three phantoms based on the first EIT sensor, which contains combinations of different targets. The background substance is saline with a conductivity of $0.07 S \cdot m^{-1}$. The excitation frequencies are $\{f_1, f_2, f_3, f_4, f_5\} = \{100, 80, 50, 40, 10\} kHz$, and $10 kHz$ is selected as the reference frequency. The conductivity of metal and plastic hardly changes with frequency, whilst the conductivity of potato and sweet potato increases progressively with the increase of current frequency (Y. Yang & Jia, 2017b). The second miniature EIT sensor has 16 planar electrodes and an inner diameter of 15 mm (see Fig. 5.9(g)). The excitation frequencies are $\{f_1, f_2, f_3, f_4, f_5\} = \{20, 30, 40, 50, 10\} kHz$, and $10 kHz$ is selected as the reference frequency. The background substance is cell culture media with a conductivity of $2 S \cdot m^{-1}$. The imaging object is a triangular MCF-7 human breast cancer cell pellet, which is less conductive than the background substance and demonstrates an increasing conductivity with the increase of current frequency.

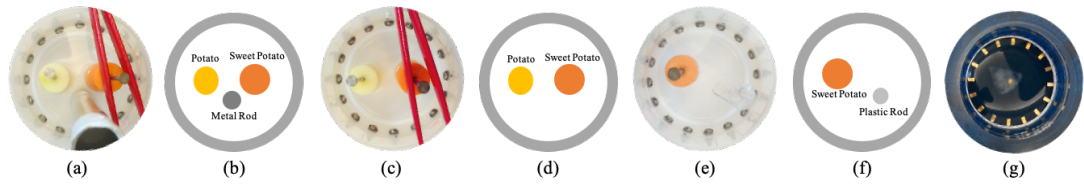


Figure 5.9: Experiment phantoms using two different 16-electrode EIT sensors. (a) Phantom 1: potato rod, sweet potato rod and metal rod. (b) Geometric distribution of phantom 1. (c) Phantom 2: potato rod and sweet potato rod. (d) Geometric distribution of phantom 2. (e) Phantom 3: sweet potato rod and plastic rod. (f) Geometric distribution of phantom 3. (g) Phantom 4: MCF-7 cell pellet

Fig. 5.10 illustrates the mfEIT image reconstruction results based on experimental data. We also compare the results quantitatively based on SSIM, which is listed in Table 5.6. Overall, only MMV-ADMM and the proposed MMV-Net manage to consistently provide a clear trend of conductivity values with respect to frequency. MMV-Net further produces more accurate shapes and fewer artifacts. Note that the potato cylinder and the sweet potato cylinder in experiment phantom 1 have the same location as that in experiment phantom 2, which is most successfully recovered by the MMV-Net. MMV, MoDL and FISTA-Net fail to identify the conductive metal cylinder in experiment phantom 1, whereas MMV-Net can roughly observe the metal cylinder but the shape is underestimated. For experiment phantom 3, MMV-ADMM, FISTA-Net and MMV-Net are more noise-resistant than MoDL. However, MoDL and MMV-

Net can reconstruct the non-conductive plastic cylinder. Similarly, for experiment phantom 4, MMV-Net is the most effective in inhibiting artifacts and shows more shape consistency at all frequencies. The results suggest that MMV-Net generalizes well to real-world experiments and outperforms the conventional model-based method and state-of-the-art learning approaches due to the competitive capability of capturing both intra- and inter-frequency correlations.

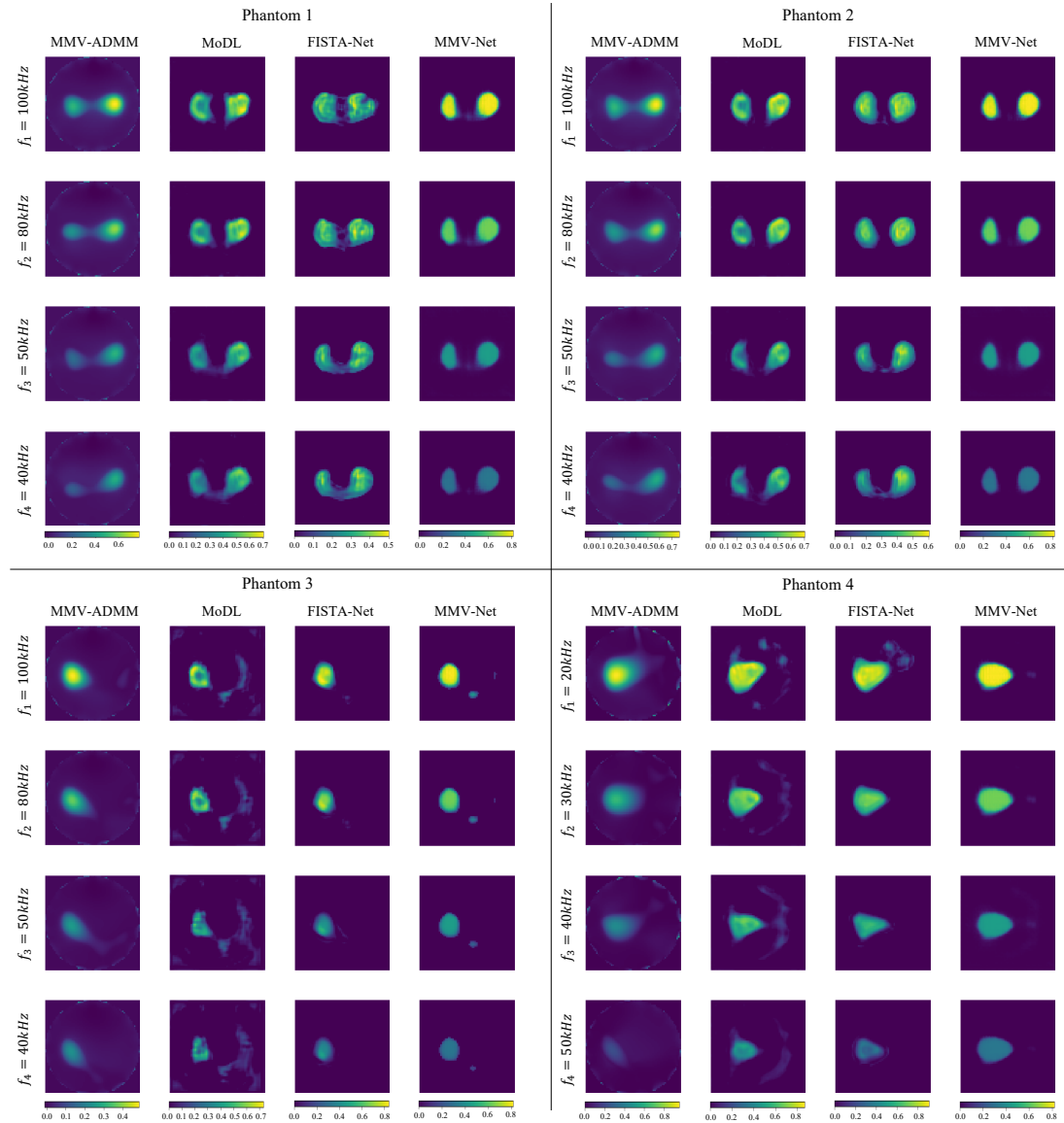


Figure 5.10: mfEIT image reconstruction results of four experimental phantoms.

Table 5.6: Numerical comparisons of experimental results based on SSIM.

Phantom		MMV-ADMM	MoDL	FISTA-Net	MMV-Net
1	f_1	0.39	0.71	0.71	0.77
	f_2	0.41	0.69	0.73	0.77
	f_3	0.45	0.69	0.72	0.76
	f_4	0.45	0.69	0.72	0.75
2	f_1	0.38	0.74	0.74	0.79
	f_2	0.41	0.75	0.76	0.79
	f_3	0.44	0.75	0.75	0.79
	f_4	0.43	0.74	0.75	0.79
3	f_1	0.53	0.61	0.79	0.80
	f_2	0.59	0.60	0.79	0.80
	f_3	0.61	0.59	0.80	0.80
	f_4	0.55	0.59	0.81	0.81
4	f_1	0.27	0.70	0.77	0.87
	f_2	0.40	0.71	0.86	0.87
	f_3	0.34	0.70	0.85	0.87
	f_4	0.36	0.74	0.85	0.87

Best results are highlighted in bold.

5.4 Summary

In this chapter, a model-based learning approach named MMV-Net was proposed to address the simultaneous image reconstruction problem of mfEIT. MMV-Net combines the advantages of the traditional MMV-ADMM algorithm and deep networks. All parameters are learned during training, rather than manually tuned. The regularizer of MMV-ADMM was generalized by introducing the spatial self-attention module and convolutional LSTM module to learn both spatial and frequency correlations between mfEIT images. Ablation experiments showed that cascading both modules strengthened the structural information effectively and provided superior results. Simulation and real-world experiments demonstrated that the proposed MMV-Net outperformed the state-of-the-art methods in terms of image quality, generalization ability, noise robustness and convergence performance.

3D Tissue Imaging with Point Cloud Network

6.1 Introduction

Despite the advancement of existing image reconstruction algorithms, most are focused on 2D geometries, and 3D image reconstruction algorithms are relatively rare. Some studies have been focused on extending 2D algorithms to 3D cases, such as direct 3D reconstruction based on Complex Geometrical Optics (CGO) solutions (Bikowski, Knudsen, & Mueller, 2010), 3D-Laplacian and sparsity joint regularization (Y. Yang et al., 2016), Bayesian learning with Total Variation prior (González, Huttunen, Kolehmainen, Seppänen, & Vauhkonen, 2016), and 3D Structure-Aware Sparse Bayesian Learning (SA-SBL) (S. Liu et al., 2019). However, these approaches are based on regular grids (e.g., voxels), and handcrafting parameters and regularization terms are usually required, resulting in low image quality and considerable computational cost.

This chapter proposes a learning-based 3D EIT reconstruction algorithm with efficient 3D representations to facilitate image accuracy, spatial resolution and computational efficiency. In terms of 3D representations, most existing image reconstruction methods adopt voxel grids for simplicity. However, voxelization of a 3D space inevitably discards lots of details, and the memory footprint increases cubically with the resolution, indicating that there is always a trade-off between the depth of network architectures and the resolution (Mescheder, Oechsle, Niemeyer, Nowozin, & Geiger, 2019). Therefore, we propose to employ point clouds to represent 3D objects in the 3D EIT reconstruction problem. We hypothesize that the dedicated deep network can generate 3D reconstructions with limited data but high resolution by learning point cloud distributions as the shape of 3D objects. In terms of the reconstruction algorithm, unlike voxel-based methods, the 3D image reconstruction task here transits to recover the 3D coordinates of points to adaptively portray objects' surfaces and predict each point's conductivity. Therefore, we propose a point cloud-based 3D EIT image reconstruction network, ptEIT. The network architecture of ptEIT resembles the structure of the well-known transformer proposed by (Vaswani et al., 2017). The main contributions of this chapter are as follows:

1. For the first time, we introduce point cloud as a new 3D representation in the 3D EIT image reconstruction problem, which provides fine-shape descriptions with a limited number of points, alleviates memory requirements, and allows for deeper network architectures.
2. A point cloud-based 3D EIT image reconstruction network, ptEIT, is proposed to translate EIT measurements to point cloud representations. ptEIT tackles the 3D EIT reconstruction problem by solving two sub-problems, i.e., shape reconstruction and conductivity prediction. Explicitly learning the two sub-problems through end-to-end training boosts the performance of ptEIT.
3. The proposed ptEIT is validated with simulation and experiments to demonstrate its superior performance compared to voxel-based 3D reconstruction algorithms.

6.2 Related Work

6.2.1 3D Representations

Learning-based 3D object reconstruction from low dimensional data (mainly 2D images (Han, Laga, & Bennamoun, 2019)) has been extensively investigated. The data representation is critical for reconstruction quality, network establishment and computational efficiency. Typically, 3D representations could be regular voxel-based, irregularly structured point cloud-based or mesh-based, and implicit function-based.

Voxels based on regular volumetric grids are a natural extension to 2D image pixels. The main advantage is that existing network architectures for 2D images can be easily extended by using 3D convolutions (J. Wu et al., 2017; Xie, Yao, Sun, Zhou, & Zhang, 2019; D. Zhang et al., 2020). However, accurate 3D reconstruction based on voxel-based representations requires finer discretization of the 3D space and deeper networks, thus limited by the computational and memory cost.

Meshes are targeted directly at the surfaces of 3D objects which are more efficient than voxel-based representations, assuming that rich information is usually located on/nearby the surfaces. Here, 3D surfaces can be described by constructing vertices and faces based on parameterization (Groueix, Fisher, Kim, Russell, & Aubry, 2018; Pumarola et al., 2018) or deformation (Kato, Ushiku, & Harada, 2018; N. Wang et al., 2018). These methods are limited to the template topology or genus-0 surfaces and the generated meshes tend to be self-intersecting and non-watertight.

Implicit Functions learned by deep networks have become an emerging strategy for describing 3D geometries (Chabra et al., 2020; Z. Chen & Zhang, 2019; Mescheder et al., 2019; Park, Florence, Straub, Newcombe, & Lovegrove, 2019). Instead of discretizing the 3D space with a fixed resolution, given a query point, these continuous functions predict the

signed surface distance value (Chabra et al., 2020; Park et al., 2019) or whether the point is inside the object as the continuous decision boundary (Z. Chen & Zhang, 2019; Mescheder et al., 2019). For visualization, one way is to feed every point in the voxel grid at any arbitrary resolution into the trained network to generate 3D volumetric images. Alternatively, the multi-resolution isosurface extraction algorithm (Mescheder et al., 2019) can extract 3D meshes from the trained network. The reported average inference time requires 3s per mesh, which is undesirable for real-time imaging.

Point Clouds are also an efficient format for 3D surfaces and have increasing popularity in many scene understanding-related applications (Y. Guo et al., 2020). Such representation is simply a collection of unordered points. It thus can naturally handle 3D shapes of arbitrary topologies with fine-grained details. Point-wise multilayer perceptrons (MLP) (Fan, Su, & Guibas, 2017; Jiang, Shi, Qi, & Jia, 2018; Mandikal & Radhakrishnan, 2019) and 1D convolutions (Gadelha, Wang, & Maji, 2018) are used to regress 3D point coordinates and the attributes for the unordered points. Similar to implicit functions, the resulting point clouds can also be post-processed to retrieve 3D meshes based on Poisson surface reconstruction (Kazhdan & Hoppe, 2013).

We propose to use point clouds to represent the 3D geometry in a non-Euclidean space for the 3D EIT image reconstruction problem for their simplicity, generalization ability, and efficiency in terms of memory and computation. Each object is described by a fixed number of points.

6.2.2 Transformer

Recently, Transformer (Vaswani et al., 2017) as a decoder–encoder structure and its variants (J. Lee et al., 2020; Z. Yang et al., 2019) have gained tremendous interest and achieved impressive performance in Natural Language Processing (NLP). The key component of Transformer is the self-attention module, which can capture long-term dependencies of context as an alternate of recurrence or convolutions by explicitly learning interactions along the sequences. This idea has been successfully extended to Computer Vision (CV) tasks, such as image recognition (Dosovitskiy et al., 2020) and object detection (Carion et al., 2020). Additionally, the self-attention module is inherently permutation invariant, which fits the property of disordered points. Therefore, it is natural to apply Transformer in point cloud learning, where it has achieved good performance in point cloud segmentation and classification tasks (M.-H. Guo et al., 2021; Hui, Yang, Cheng, Xie, & Yang, 2021).

This chapter proposes to exploit Transformer to solve the 3D EIT reconstruction problem. Extracting context dependencies between points is expected to facilitate the quality of reconstructed point cloud representations.

6.3 Point Cloud Network

6.3.1 Problem Definition

The EIT-image-reconstruction problem aims to recover the conductivity distribution given the boundary voltage measurements. In this work, we represent the targeted objects as point sets $S = P^{(1)} \cup P^{(2)} \cup \dots \cup P^{(N)}$, where $P^{(n)}$ donates the n^{th} object and N is the maximum number of objects. M points are used to represent each object, $P^{(n)} = \{(x_i^{(n)}, y_i^{(n)}, z_i^{(n)}, c^{(n)})\}_{i=1}^M$, where each point $P_i^{(n)}$ is a vector of 3D coordinates $(x_i^{(n)}, y_i^{(n)}, z_i^{(n)})$ and the conductivity value c^n . Here, we assume uniform conductivity distribution for each object. With point clouds, arbitrary topologies could be described. The input of the network is a sequence of ordered EIT voltage measurements $X = \{(v_i, C_i^{e1}, C_i^{e2})\}_{i=1}^{N_M}$, where N_M is the number of independent measurements; $v_i \in \mathbb{R}$ is the calibrated voltage readout; $C_i^{e1} \in \mathbb{R}^3$ is the 3D coordinates of current injection electrodes; $C_i^{e2} \in \mathbb{R}^3$ is the 3D coordinates of voltage measurement electrodes.

6.3.2 Point Cloud Network

We employ the proposed point-cloud transformer for 3D EIT image reconstruction, i.e., ptEIT (see Figure 6.1), which is established based on Transformer (Vaswani et al., 2017). As point clouds are not limited to regular geometry, ptEIT has a strong generalization ability for irregular shapes and expression ability for fine details. The key idea of ptEIT is to divide the challenging 3D EIT image reconstruction task into two sub-tasks: shape reconstruction and conductivity estimation.

In general, ptEIT comprises one encoder and two decoders. The objective of the encoder $E(\cdot)$ is to convert the voltage readouts incorporating the electrodes' topology information to a high-dimensional latent code-word. We consider that the geometry information of electrodes plays a vital role in helping the deep learning model to find the correct non-linear relationship, thus improving the convergence speed. The input of the encoder not only contains the voltage measurements but also six coordinates of each measurement's corresponding injection and measurement electrode pairs. The voltage measurement $v \in \mathbb{R}^{N_M}$ is first linearly transformed to the embedding dimension (128) for the following self-attention operation, by an MLP $f_v(\cdot)$ operation. The position information $(C^{e1}, C^{e2}) \in \mathbb{R}^{N_M \times 6}$ is encoded through another MLP $f_c(\cdot)$. After adding the extracted positional information and voltage measurements together, a transformer encoder module, which is identical to the original paper (Vaswani et al., 2017), is applied to generate latent code-word $L \in \mathbb{R}^{N_M \times 128}$.

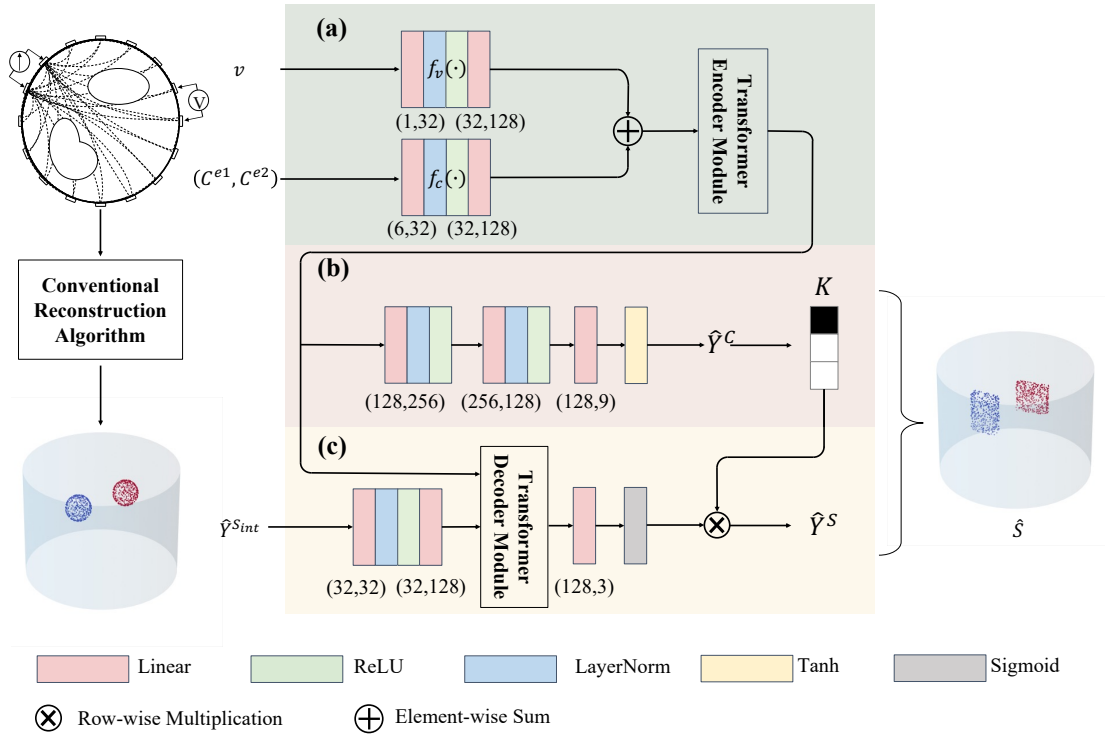


Figure 6.1: The network architecture of the proposed point-cloud transformer for 3D EIT image reconstruction (ptEIT). The voltage measurement and position information are embedded and then mapped into a latent space by an encoder. Based on the latent code, the conductivity decoder estimates conductivity values \hat{Y}^C and makes constraints K on structural information for the shape decoder. Meanwhile, the measurement data is reused to provide an initial guess about the shape distribution $\hat{Y}^{S_{int}}$. With the latent code, the initial shape is fed into the shape decoder to reconstruct a fine-tuned shape \hat{Y}^S . Finally, \hat{Y}^C and \hat{Y}^S are concatenated to provide the targeted point cloud S . (a) The encoder $E(\cdot)$. (b) The conductivity decoder $D_c(\cdot)$. (c) The shape decoder $D_s(\cdot)$.

Conductivity decoder: A conductivity decoder $D_c(\cdot)$ is introduced to estimate conductivity values: low conductivity, high conductivity and background. $D_c(\cdot)$ is constructed by a few MLPs followed by a tanh layer to generate a probability matrix $\hat{Y}^C = \{(c_{i0}, c_{i1}, c_{i2})\}_{i=1}^N$, where each column represents the class of conductivity value. We use cross-entropy \mathcal{L}_C to train $D_c(\cdot)$. \hat{Y}^C is further reused to create a structural constraint $K \in \mathbb{R}^N$ in the form of binary masks to inform the object number inside the sensing region for the following shape decoder.

Shape decoder: The main difficulty lies in the shape reconstruction task, which is treated as a deformation task accomplished by a shape decoder $D_s(\cdot)$. The network starts from certain initial shapes $\hat{Y}^{S_{int}}$. To generate an appropriate initial shape, we introduce the voxel-based algorithm, i.e. 3D-Laplacian (Y. Yang et al., 2016). 3D-Laplacian employs the one-step Gauss-Newton solver with a Laplacian filter to obtain an image. The reconstructed image is firstly segmented using a threshold of 30% of the maximum conductivity value. After segmentation, we use k-means clustering to determine 3D coordinates of the centroid of each object. Surrounding these centroids, we generate spheroids with the same radii for each object to construct $\hat{Y}^{S_{int}}$. Notice that our network has the ability to reconstruct arbitrary shapes away from the sphere. $\hat{Y}^{S_{int}}$ is then transformed into the embedding dimension by an MLP. Together with L , the output of the MLP is fed into a transformer decoder module identical to the original paper (Vaswani et al., 2017), a fully connected layer, and a sigmoid layer for activation. The output of the sigmoid layer is further masked by K to zero out coordinates of unnecessary objects, resulting in $\hat{Y}^S = \{(x_i, y_i, z_i)\}_{i=1}^{N \times M}$. In terms of the objective functions, Earth Mover’s Distance (EMD) (Andoni, Indyk, & Krauthgamer, 2008), Hausdorff Distance (HD) (Huttenlocher, Klanderman, & Rucklidge, 1993) and Chamfer Distance (CD) (Butt & Maragos, 1998) are commonly used in point cloud learning, which are defined by

$$\mathcal{L}_{EMD}(Y^S, \hat{Y}^S) = \min_{\phi: Y^S \rightarrow \hat{Y}^S} \sum_{s \in Y^S} \|s - \phi(s)\|_2^2 \quad (6.1)$$

$$\mathcal{L}_{HD}(Y^S, \hat{Y}^S) = \max_{\hat{Y}^S} (\max_{s \in Y^S} \min_{\hat{s} \in \hat{Y}^S} \|s - \hat{s}\|_2^2, \max_{s \in Y^S} \min_{\hat{s} \in \hat{Y}^S} \|s - \hat{s}\|_2^2) \quad (6.2)$$

$$\mathcal{L}_{CD}(Y^S, \hat{Y}^S) = \sum_{\hat{s} \in \hat{Y}^S} \min_{s \in Y^S} \|s - \hat{s}\|_2^2 + \sum_{s \in Y^S} \min_{\hat{s} \in \hat{Y}^S} \|s - \hat{s}\|_2^2 \quad (6.3)$$

where ϕ is a bijection, and Y^S is the ground truth of point cloud;. EMD conducts rigorous assignments that are computationally expensive due to repetitive forward and backward propagations during training, while HD is unable to guarantee stable convergence with the presence of outlier points. This chapter adopts an Object-Wise CD (OWCD) function for shape

reconstruction by modifying equation 6.3:

$$\mathcal{L}_s(Y^S, \hat{Y}^S) = \frac{1}{N} \sum_{i=1}^N \left(\sum_{\hat{p} \in \hat{P}^{(i)}} \min_{p \in P^{(i)}} \|p - \hat{p}\|_2^2 + \sum_{p \in P^{(i)}} \min_{\hat{p} \in \hat{P}^{(i)}} \|p - \hat{p}\|_2^2 \right) \quad (6.4)$$

where $\hat{P}^{(i)}$ and $P^{(i)}$ are the n^{th} object in \hat{Y}^S and Y^S respectively. Compared to CD, the main advantage of OWCD is that considering one point belonging to $\hat{P}^{(i)}$, it depresses the minimum distance within $\hat{P}^{(i)}$ instead of other objects $\hat{Y}^S \setminus \hat{P}^{(i)}$, indicating that points will not jump in-between objects during training. As a result, the object-level correspondence can be achieved and the mean-shape behaviour (Fan et al., 2017) can also be avoided.

6.3.3 Network Training

The training was implemented on two NVIDIA P5000 GPUs. The optimizer used in training is Adam (Kingma & Ba, 2014) with a weight decay of 10^{-8} . The initial learning rate is 10^{-4} and decreases by 0.7 times every 20 steps. The batch size is 32 and the maximum training epoch is 400. The models with the least validation loss are selected as the final models. The transformer encoder and decoder modules have 6 stacks of encoder/decoder sub-modules with 4 heads of attention.

6.4 Results and Discussion

6.4.1 3D EIT Dataset

To generate the 3D EIT dataset, we model a cylindrical 32-electrode EIT sensor using COMSOL Multiphysics (see figure 6.2). The voltage measurements are collected based on the adjacent measurement strategy. In total, the 3D EIT dataset has 21,135 samples. Details of the constitution are provided in table 6.1. The data set has at most three objects, two types of geometry, and two types of conductivity. The background conductivity is $2 \text{ S} \cdot \text{m}^{-1}$. Each object has a random location and size while overlapping in between is not allowed. Points are uniformly distributed on the surface of each object. To eliminate systematic defects due to sensor imperfection, both voltage measurements and conductivity values in the data set are normalized as did in (3.12) and (3.13). Finally, the normalized dataset is split into training, validation, and testing sets for network training with a ratio of 8:1:1.

We also implement data augmentation by adding Gaussian noise to measurement data in both training and validation sets. Additive noise with the Signal-to-Noise Ratio (SNR) of 50 dB is added to one-third of the training and validation samples. Additive noise with the SNR of 40 dB is then added to the other two-thirds of the training and validation data. Consequently, both training and validation data are doubled.

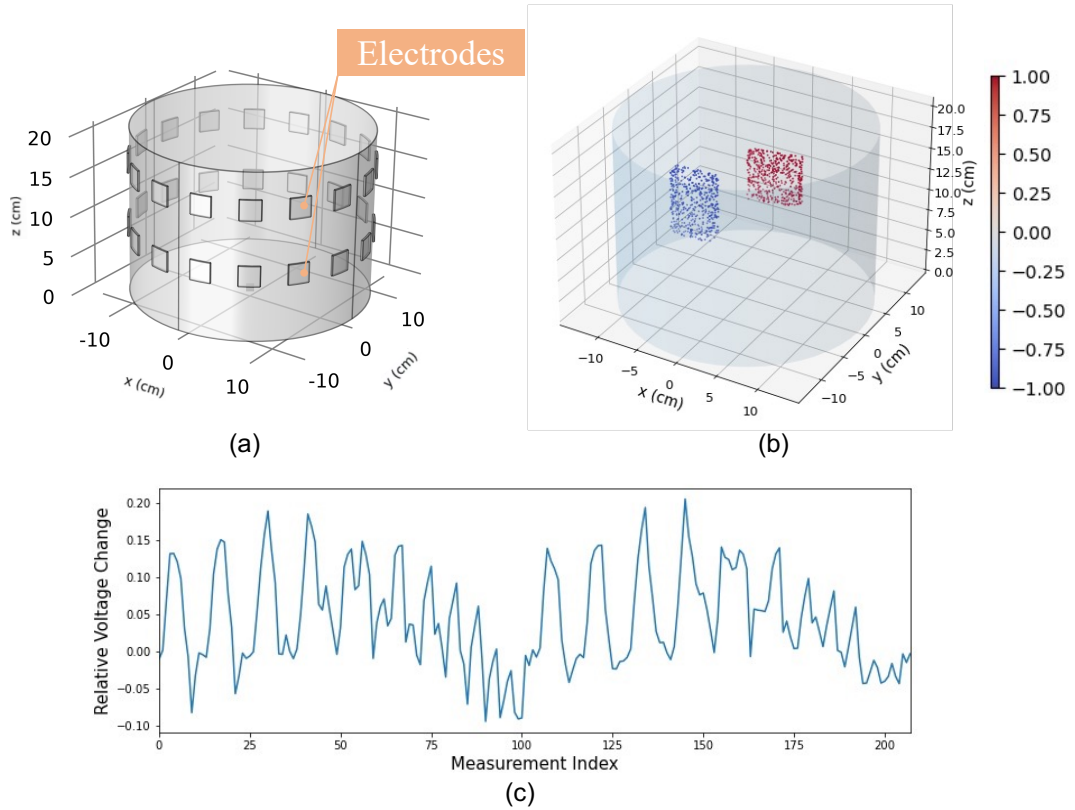


Figure 6.2: (a) Sensor modelling: the inner diameter is 28.7 cm and the height is 20.6 cm. (b)-(c) An example of 3D conductivity distribution represented by point clouds and corresponding voltage measurement.

Table 6.1: 3D EIT dataset constitution. For each object, the conductivity value and geometry are randomly selected from the given sets.

No. of objects	2	3
No. of samples	8,872	12,263
Conductivity ($S \cdot m^{-1}$)	{0.1, 3.9}	
Geometry	{spheroid, block}	

6.4.2 Evaluation on Simulation Data

In this sub-section, we evaluate the performance of the proposed ptEIT based on the 3D EIT simulation data.

Performance Comparison

We compare the proposed ptEIT with two state-of-the-art image-reconstruction methods for 3D EIT based on regular volumetric grid of $32 \times 32 \times 40$, i.e. 3D-Laplacian (Y. Yang et al., 2016) and the 3D version of the FC-UNet (3D-FC-UNet) (Z. Chen et al., 2020) on the testing set. 3D-Laplacian is a conventional model-based method while 3D-FC-UNet is a learning-based reconstruction method. Table 6.2 shows quantitative comparison based on average OWCD, OWHD (object-wise HD), CA (classification accuracy), Root Mean Square Error (RMSE), Structural Similarity Index Measure (SSIM), FPS (Frame Per Second), and FLOPS (Floating Point Operations Per Second) on all the testing data. All methods are suitable for real-time 3D EIT imaging, where 3D-Laplacian based on a simple mathematical inversion is 10 times faster than the other two learning-based methods. However, 3D-FC-UNet significantly performs better than 3D-Laplacian in terms of image quality, indicating the superiority of deep networks. Our ptEIT is 1.2 times more accurate in predicting the conductivity levels but with 15 times fewer trainable parameters than 3D-FC-UNet. ptEIT also achieves lower floating-point operations than 3D-FC-UNet.

Table 6.2: Numerical comparisons (OWCD, OWHD, CA, RMSE, SSIM, FPS, and FLOPS) on the testing set.

Metrics	3D-Laplacian Y. Yang et al. (2016)	3D-FC-UNet Z. Chen et al. (2020)	ptEIT
OWCD (cm)	-	-	0.0288
OWHD (cm)	-	-	0.514
CA	-	80.1%	98.1%
RMSE	0.134	0.086	-
SSIM	0.584	0.962	-
No. of learning parameters	-	31,859,331	2,088,823
FPS (ft/s)	566.74	52.79	41.61
FLOPS (GMac)	-	42.31	3.5

Best results are highlighted in bold.

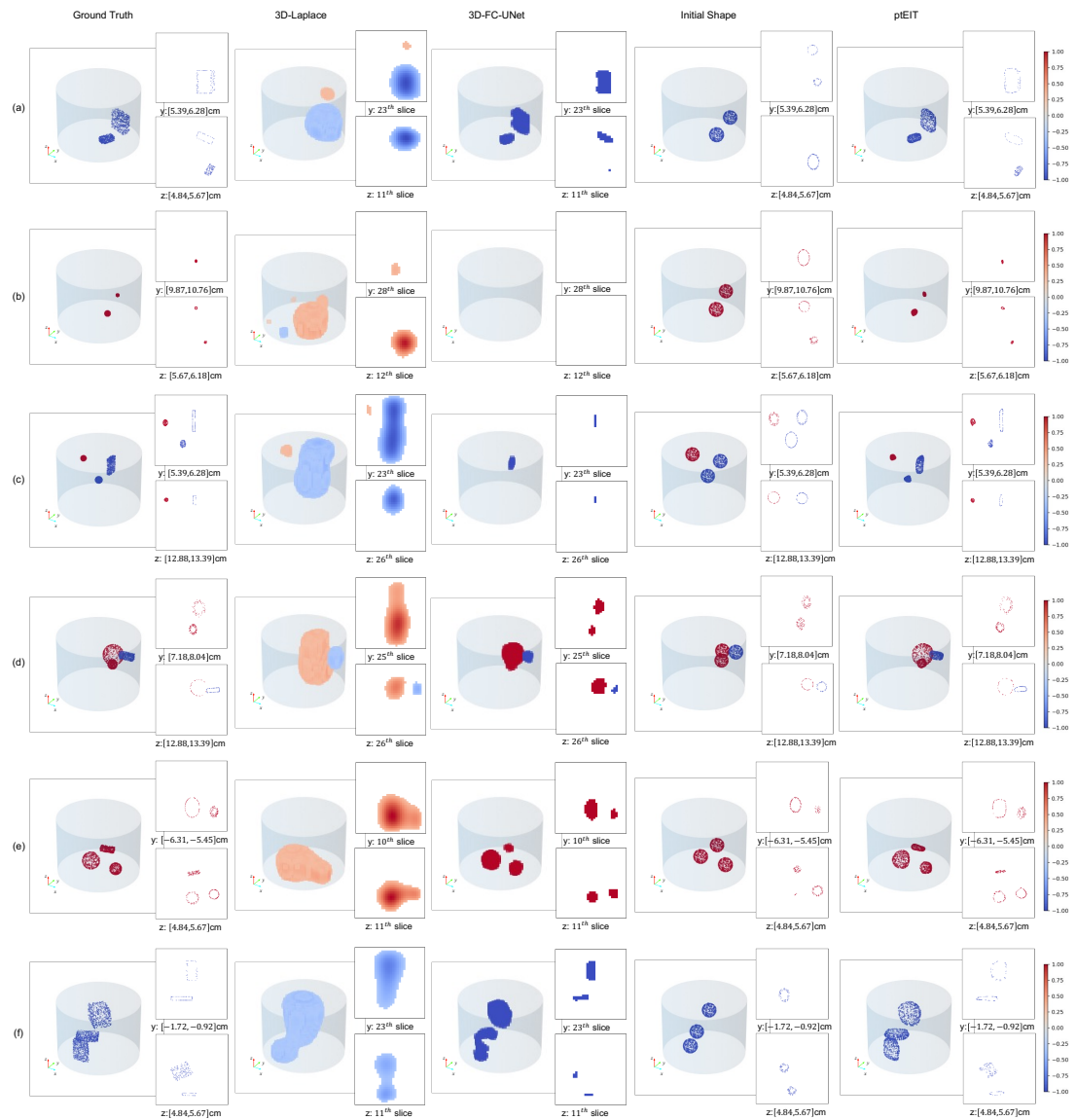


Figure 6.3: 3D reconstruction results from the testing set. The ground truth, initial shapes where ptEIT starts from, and results of ptEIT are represented by point clouds, whereas the other two algorithms are based on the voxel grid. Apart from 3D reconstructions, two critical 2D slices for each 3D image are visualized for qualitative comparison. For each row, numerical coordinate ranges to generate 2D slices for point clouds correspond to slice numbers in voxel grids.

Figure 6.3 illustrates six examples of 3D reconstruction results for qualitative comparison. Our ptEIT outperforms the benchmark algorithms with the highest image quality in terms of object number, position, geometry, and conductivity level estimation. Figure 6.4 provides a zoomed-in version of phantom (f) from Figure 6.3. Higher visual quality and finer surface details are achieved by ptEIT owing to the increased resolution and representation flexibility of point clouds.

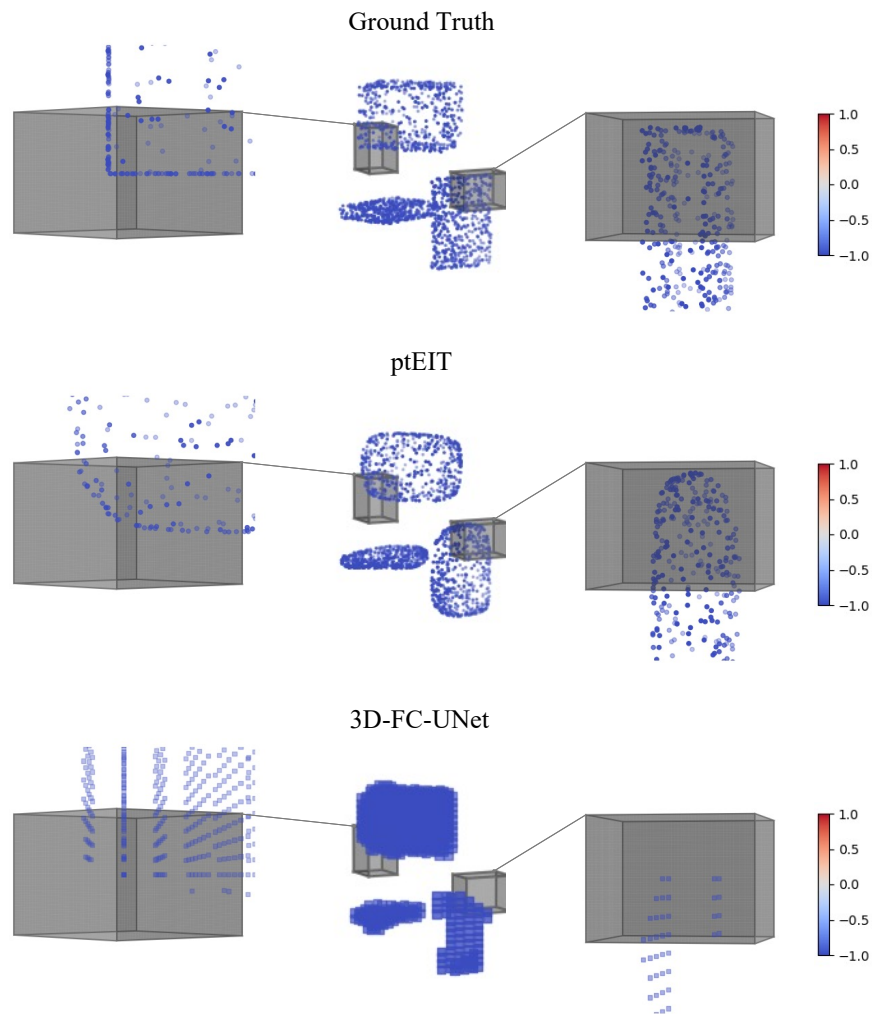


Figure 6.4: Qualitative comparison of the two learning-based algorithms. Cyan boxes: zoomed-in region of interest.

Generalization to Different Noise Levels

We demonstrate the generalization ability of ptEIT by testing the measurements with the noise of 100 dB (nearly noise-free), 50 dB, 40 dB and 30 dB respectively. Table 6.3 reports the average evaluation results on the testing set based on OWHD, OWCD, and CA of the conductivity branch. We observe that 50 dB results are close to 100 dB results. Furthermore, the upper limit of OWCD is empirically around 0.4 cm. In other words, certain reconstruction results with OWCD exceeding 0.4 cm suffer from considerable errors in shape, position or conductivity estimation. Our ptEIT achieves acceptable results even at the unseen 30 dB, which demonstrates its good generalization ability. Figure 6.5 illustrates an example of point cloud visualizations under various noise levels, which matches the average performance of ptEIT shown in Table 6.3.

Table 6.3: Evaluation on the testing set under different noise levels.

SNR(dB)	OWCD (cm)	OWHD (cm)	CA
100	0.0288	0.514	95.2%
50	0.0350	0.578	95.2%
40	0.0765	0.982	76.2%
30	0.205	2.208	47.6%

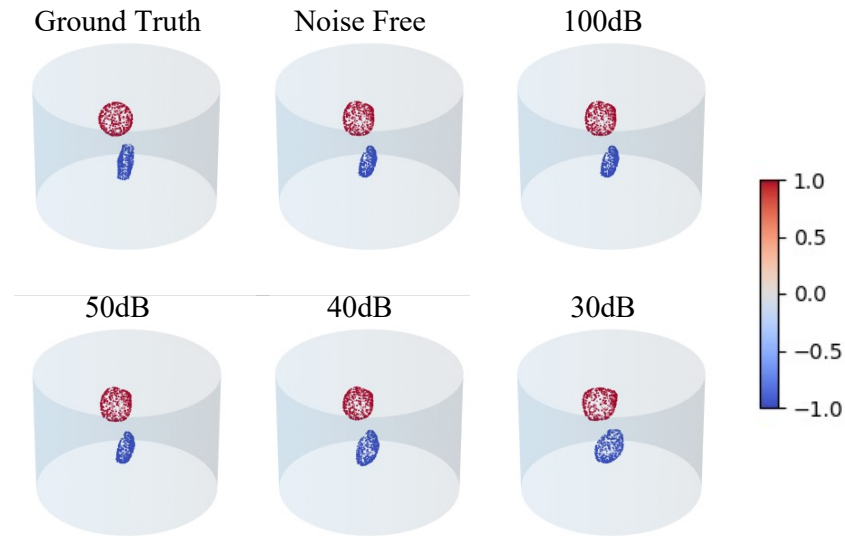


Figure 6.5: An example of qualitative results under different noise levels.

Variable Resolution Feature

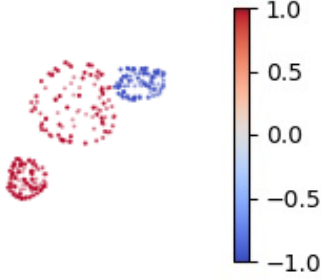
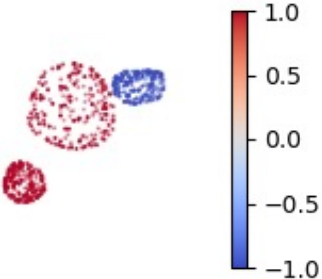
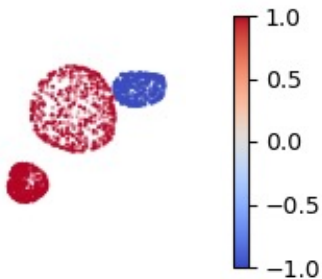
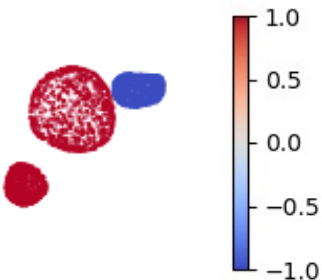
Existing learning-based reconstruction methods are restricted to the resolution of training data. Re-training these models is inevitable to handle different resolutions. In contrast, our ptEIT possesses an interesting and attractive property in that the model trained on one resolution dataset can be directly reused to reconstruct targets with arbitrary resolutions. In this chapter, ptEIT is trained on a 500-point-resolution dataset while it could reconstruct point clouds with a 200-point resolution by simply inputting initial shapes with 200 points. This variable resolution feature of ptEIT benefits from the power of self-attention operators, where the learnable parameters $W^Q \in \mathbb{R}^{n_{dim} \times d_Q}$, $W^K \in \mathbb{R}^{n_{dim} \times d_K}$, and $W^V \in \mathbb{R}^{n_{dim} \times d_V}$ to linearly project n_{dim} -dimensional feature maps queries \mathbf{Q} , keys \mathbf{K} and values \mathbf{V} to d_Q, d_K, d_V dimensions respectively are not relevant to the point resolution M but the feature number of each point n_{dim} . Therefore, the self-attention operators can implement matrix multiplication with input data of various M . Table 6.4 shows the results of applying ptEIT trained on data with $M = 500$ to various reconstruction tasks when $M \in \{100, 200, 500, 1000\}$. As M increases, OWCD and OWHD decline gradually whereas CA is not affected by M . The results indicate that our ptEIT could function as a uniform interpolater for the unordered output point set as long as both the training data set and initial point set are uniform.

6.4.3 Evaluation on Experimental Data

In addition to the simulation study, we carried out real-world experiments on a cylindrical EIT sensor designed by Y. Yang and Jia (2017b) to assess the generalization ability of the proposed method. 3D image reconstruction is challenging due to its sensitivity to sensor imperfection and its even more ill-posedness nature. The EIT sensor, as shown in the first column of Figure 6.6, is equipped with two layers of electrodes, and each layer has 16 electrodes. The inner diameter of the sensing chamber is 287 mm. The background substance is saline, with a height of 206 mm. The imaging targets are 3D printed with polylactide (PLA), a widely used plastic filament material for 3D printing. Shapes include spheroid and cuboid with different sizes. Conductive targets are wrapped with copper.

Fig. 6.6 illustrates the 3D image reconstruction results of three phantoms. In experiment phantom 1, 3D-Laplacian manages to recover both conductivity contrast and provides a rough 3D position of the spheroid, but the size is overestimated. 3D-FC-UNet suffers from severe image artifacts and fails to tell the target shape. This is because the single object pattern is not included in training data. In contrast, ptEIT exhibits strong generalization ability with accurate target shape and conductivity estimation. In experiment phantom 2, both targets induce negative conductivity change, which all methods recognise. Apart from conductivity values, all methods could provide accurate 3D positions of both targets but coarse shapes. Compared to the spheroid, the cuboid is a challenging shape which is overestimated by 3D-Laplacian. The two learning methods present a state between spheroid and cuboid. In

Table 6.4: Visual quality under different point resolutions and evaluation metrics.

Resolution M	Visual Quality	OWCD (cm)	OWHD (cm)	CA
100		0.0388	1.030	95.2%
200		0.0264	0.6303	95.2%
500		0.0176	0.2831	95.2%
1000		0.0138	0.2795	95.2%

experiment phantom 3, the upper left cuboid and the lower right spheroid induce positive and negative conductivity change, respectively. All methods perform accurate conductivity contrast prediction. However, ptEIT yields effectively and consistently better 3D shapes and positions. These results suggest that ptEIT can generalize well to real experimental setups and outperforms conventional voxel-based methods. Both the unique 3D data representation strategy and powerful network architecture of ptEIT make a worthwhile contribution to accurate predictions in terms of conductivity estimation, spatial resolution, noise-resistance performance, as well as computational efficiency.

6.5 Summary

In this chapter, a transformer-based 3D EIT image reconstruction algorithm was reported. The proposed algorithm synergically integrates point-cloud-based irregular-grid data representation, attention-based architecture, multi-task learning paradigm and tailored object-wise chamfer distance loss function. With a trivial requirement of prior knowledge, i.e., the maximum amount of objects, ptEIT could reconstruct 3D point clouds with high spatial resolution and visual quality. Compared with the voxel-based approach, ptEIT shows higher-fidelity visual quality with fine details and dramatically reduces memory cost and complexity. Moreover, due to the interpolation equivalence property of the self-attention operator, ptEIT trained on a specific resolution dataset can be applied to arbitrary resolution reconstructions. The proposed approach is an early study of 3D EIT image reconstruction, verified by experiments with 3D printed phantoms. Future work will investigate ptEIT's application in 3D tissue imaging.

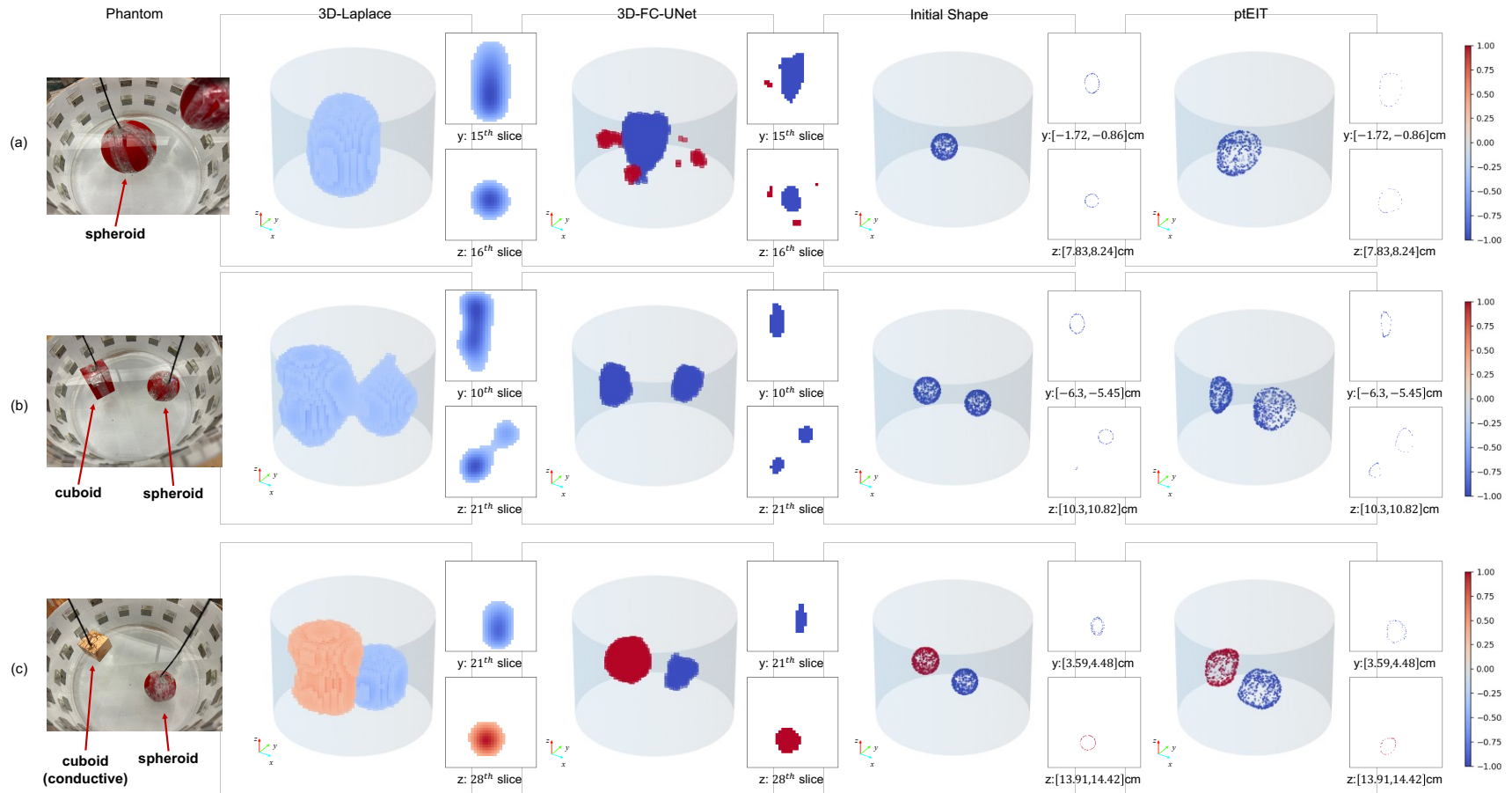


Figure 6.6: Experimental results on EIT sensors. For each row, numerical coordinate ranges for point clouds correspond to the selected 2D slice numbers for voxel grids. The results of ptEIT start from initial shapes. (a) Experiment phantom 1: a spheroid. (b) Experiment phantom 2: a cuboid (left) and a spheroid (right). (c) Experiment phantom 3: a conductive cuboid (upper left wrapped with copper) and a spheroid (lower right).

Conclusions and Future Work

7.1 Conclusions

Bioimpedance tomography, or EIT, as a promising tomographic imaging modality, has been widely adopted in biomedical engineering because of its non-destructiveness and label-free imaging nature. The main challenge of EIT comes from the nonlinear and ill-posed image reconstruction problem. Recent advances in deep learning have pointed out a promising direction for EIT image reconstruction. This thesis explored the development of an imaging platform integrating multi-frequency EIT and machine learning-based image reconstruction algorithms to image 3D cells under in vitro conditions. A comprehensive study was carried out in terms of hybrid learning-based cell imaging, structure-aware learning-based cell culture imaging, model-based learning algorithm for mfEIT image reconstruction and 3D imaging using a point cloud network. The detailed work, contributed by this thesis, is summarised as follows.

The foundation of EIT, the prospective use for EIT in tissue engineering, the cutting-edge EIT image reconstruction algorithms, and the recent challenge in tissue engineering were reviewed. This review pointed out the recent advances of the EIT and the importance of deep learning in biomedical imaging, which is the background of the innovative work demonstrated in this thesis.

For EIT image reconstruction, it is challenging to image multiple objects with varying conductivity levels with a single neural network. To address this issue, a hybrid algorithm, named DL-GS, based on deep learning and group sparsity regularization was proposed for 3D cultivated cell imaging with miniature EIT sensors. This work specifically focused on the challenge of performing multi-conductivity-level imaging under multiple objects setups. An EIT dataset with continuously varying conductivity values for different sensing objects was established. An FC-UNet model was then developed to provide structural information of multi-level conductivity distribution. Afterwards, this structural information was integrated into group sparsity regu-

larization to estimate the continuous conductivity values. Both simulation and experiments demonstrated that the proposed DL-GS method outperforms the other given image reconstruction approaches and demonstrates strong generalization ability on a practical miniature EIT sensor to image MCF-7 cell aggregates.

Deep learning in the DL-GS method provides binary structural information, whereas the regularization algorithm determines conductivity contrasts. Despite the advancement of structure distribution, the exact conductivity values of different objects are less accurately estimated by the regularization-based framework, which essentially prevents EIT's transition from generating qualitative images to quantitative images. Therefore, a structure-aware dual-branch deep learning method (SADB-Net) was proposed to further tackle the challenge of accurate reconstruction of the multi-object, multi-value conductivity distributions with EIT for tissue engineering applications. Typical convolutional networks (LeNet and the baseline model) run much faster than conventional approaches but are still unsatisfactory when estimating conductivity values. The proposed network SADB-Net demonstrated that by separating the estimation of structure distribution and conductivity values using two branches and then fusing the information together, SADB-Net could generate high-quality reconstructions of multi-object, multi-conductivity-value distributions with better structural and conductivity estimation. SADB-Net also exhibits good generalization ability on miniature EIT sensors.

Multi-frequency Electrical Impedance Tomography (mfEIT) is an emerging biomedical imaging modality to reveal frequency-dependent conductivity distributions in biomedical applications. Conventional model-based image reconstruction methods suffer from low spatial resolution, unconstrained frequency correlation and high computational cost. Most existing learning-based approaches deal with the single-frequency setup, which is inefficient and ineffective when extended to the multi-frequency setup. A model-based learning approach named MMV-Net was then proposed to address the simultaneous image reconstruction problem of mfEIT. MMV-Net combines the advantages of the traditional MMV-ADMM algorithm and deep networks. All parameters are learned during training, rather than manually tuned. The regularizer of MMV-ADMM was generalized by introducing the spatial self-attention module and convolutional LSTM module to learn both spatial and frequency correlations between mfEIT images. Ablation experiments showed that cascading both modules strengthened the structural information effectively and provided superior results. Simulation and real-world experiments demonstrated that the proposed MMV-Net outperformed the state-of-the-art methods regarding image quality, generalization ability, noise robustness and convergence performance.

Finally, this thesis investigated efficient representations of 3D geometries for EIT image reconstruction. Existing reconstruction algorithms adopt voxel grids for representation, which typically results in low image quality and considerable computational cost, and limits their applicability to real-time applications. Therefore, the point cloud was introduced as a new 3D representation in the 3D EIT image reconstruction problem. Based on point cloud rep-

resentation, a transformer-based 3D EIT image reconstruction algorithm named ptEIT was reported. The proposed algorithm synergically integrates point-cloud-based irregular-grid data representation, attention-based architecture, multi-task learning paradigm and tailored object-wise chamfer distance loss function. With a trivial requirement of prior knowledge, i.e., the maximum amount of objects, ptEIT could reconstruct 3D point clouds with high spatial resolution and visual quality. Compared with the voxel-based approach, ptEIT shows higher-fidelity visual quality with fine details, dramatically reducing memory cost and complexity. Moreover, due to the interpolation equivalence property of the self-attention operator, ptEIT trained on a specific resolution dataset can be applied to arbitrary resolution reconstructions. This work offered an alternative approach for 3D tissue imaging with EIT.

In summary, the work demonstrated in this thesis contributes to addressing the existing research void in tissue imaging with bioimpedance tomography. Learning-based imaging approach development and integration with the in-house developed bioimpedance tomography system have been explored. The reliable results achieved in this thesis could promote bioimpedance tomography as a robust, intelligent tissue imaging technique for tissue engineering applications, which can also facilitate data-driven decision systems in biomedical engineering.

7.2 Future Work

Although this thesis promotes the application of miniature EIT in regenerative medicine, the adoption of EIT in this field is still at its preliminary stage. Extensive efforts are still needed to promote EIT in tissue engineering from the following directions:

1. The study of point cloud network for 3D EIT image reconstruction is still at an early stage examined on simplified phantoms. Its application in practical cell culture monitoring is more complicated and its feasibility requires further investigations.
2. Monitoring the 3D cell culture process requires dynamic imaging, resulting in time-series measurement data. Conventional algorithms often use single-frame data to reconstruct EIT images, and images reconstructed from multiple frames are independent. These methods ignore the temporal correlation of the conductivity distribution. In addition, the reconstructed images are susceptible to measurement noise, which may break the temporal correlation of images reconstructed at different time points. Therefore, the spatiotemporal correlation of conductivity distribution needs exploration to improve the EIT image quality and algorithm stabilization.
3. Based on measurement data merely from the EIT system, the state-of-the-art learning-based image reconstruction algorithms have demonstrated significant improvement in reconstructing the electrical properties of cell aggregates, regarding conductivity accuracy and artefact reduction. However, other imaging modalities with information fu-

sion may further enhance image quality in terms of structure preservation, background artifact suppression, and conductivity prediction. Multi-modal approaches are also attractive in alleviating EIT ill-posedness with the help of complementary information from other imaging modalities.

4. While EIT is an attractive solution for non-destructive, label-free monitoring of 3D cell cultures, the ideal spatial resolution is at the cellular level ($\sim 50 \mu m$) to allow monitoring of specific cells. Besides algorithm design, more advanced EIT sensors could be developed targeting cellular resolution.

Reference

- Adler, A., Arnold, J. H., Bayford, R., Borsic, A., Brown, B., Dixon, P., ... others (2009). Greit: a unified approach to 2d linear eit reconstruction of lung images. *Physiological measurement*, 30(6), S35.
- Adler, A., & Boyle, A. (2017). Electrical impedance tomography: Tissue properties to image measures. *IEEE Transactions on Biomedical Engineering*, 64(11), 2494–2504.
- Adler, J., & Öktem, O. (2018). Learned primal-dual reconstruction. *IEEE transactions on medical imaging*, 37(6), 1322–1332.
- Aggarwal, H. K., Mani, M. P., & Jacob, M. (2018). Modl: Model-based deep learning architecture for inverse problems. *IEEE transactions on medical imaging*, 38(2), 394–405.
- Ahn, S., Oh, T. I., Jun, S. C., Seo, J. K., & Woo, E. J. (2011). Validation of weighted frequency-difference eit using a three-dimensional hemisphere model and phantom. *Physiological measurement*, 32(10), 1663.
- Andoni, A., Indyk, P., & Krauthgamer, R. (2008). Earth mover distance over high-dimensional spaces. In *Soda* (Vol. 8, pp. 343–352).
- Audebert, N., Le Saux, B., & Lefèvre, S. (2018). Beyond rgb: Very high resolution urban remote sensing with multimodal deep networks. *ISPRS journal of photogrammetry and remote sensing*, 140, 20–32.
- Bavli, D., Prill, S., Ezra, E., Levy, G., Cohen, M., Vinken, M., ... Nahmias, Y. (2016). Real-time monitoring of metabolic function in liver-on-chip microdevices tracks the dynamics of mitochondrial dysfunction. *Proceedings of the National Academy of Sciences*, 113(16), E2231–E2240.
- Beck, A., & Teboulle, M. (2009). A fast iterative shrinkage-thresholding algorithm for linear inverse problems. *SIAM journal on imaging sciences*, 2(1), 183–202.
- Benson, K., Cramer, S., & Galla, H.-J. (2013). Impedance-based cell monitoring: barrier properties and beyond. *Fluids and Barriers of the CNS*, 10(1), 1–11.
- Bikowski, J., Knudsen, K., & Mueller, J. L. (2010). Direct numerical reconstruction of conductivities in three dimensions using scattering transforms. *Inverse Problems*, 27(1), 015002.

- Borsic, A., Graham, B. M., Adler, A., & Lionheart, W. R. (2009). In vivo impedance imaging with total variation regularization. *IEEE transactions on medical imaging*, 29(1), 44–54.
- Brown, B. H. (2003). Electrical impedance tomography (eit): a review. *Journal of medical engineering & technology*, 27(3), 97–108.
- Brown, B. H., & Seagar, A. D. (1987). The sheffield data collection system. *Clinical physics and physiological measurement*, 8(4A), 91.
- Butt, M. A., & Maragos, P. (1998). Optimum design of chamfer distance transforms. *IEEE Transactions on Image Processing*, 7(10), 1477–1484.
- Carion, N., Massa, F., Synnaeve, G., Usunier, N., Kirillov, A., & Zagoruyko, S. (2020). End-to-end object detection with transformers. In *European conference on computer vision* (pp. 213–229).
- Carlson, M. W., Alt-Holland, A., Egles, C., & Garlick, J. A. (2008). Three-dimensional tissue models of normal and diseased skin. *Current Protocols in Cell Biology*, 41(1), 19–9.
- Chabra, R., Lenssen, J. E., Ilg, E., Schmidt, T., Straub, J., Lovegrove, S., & Newcombe, R. (2020). Deep local shapes: Learning local sdf priors for detailed 3d reconstruction. In *European conference on computer vision* (pp. 608–625).
- Chen, S., Einspanier, R., & Schoen, J. (2015). Transepithelial electrical resistance (teer): a functional parameter to monitor the quality of oviduct epithelial cells cultured on filter supports. *Histochemistry and cell biology*, 144, 509–515.
- Chen, Z., et al. (2020). Deep learning based cell imaging with electrical impedance tomography. In *2020 IEEE International Instrumentation and Measurement Technology Conference (I2MTC)* (pp. 1–6).
- Chen, Z., et al. (2021). Structure-aware dual-branch network for electrical impedance tomography in cell culture imaging. *IEEE Transactions on Instrumentation and Measurement*, 70, 1–9.
- Chen, Z., Xiang, J., Bagnaninchi, P.-O., & Yang, Y. (2022). Mmv-net: A multiple measurement vector network for multifrequency electrical impedance tomography. *IEEE Transactions on Neural Networks and Learning Systems*.
- Chen, Z., Yang, Y., & Bagnaninchi, P.-O. (2020). Hybrid learning-based cell aggregate imaging with miniature electrical impedance tomography. *IEEE Transactions on Instrumentation and Measurement*, 70, 1–10.
- Chen, Z., & Zhang, H. (2019). Learning implicit fields for generative shape modeling. In *Proceedings of the IEEE/CVF conference on computer vision and pattern recognition* (pp. 5939–5948).

- Cheng, K.-S., Isaacson, D., Newell, J., & Gisser, D. G. (1989). Electrode models for electric current computed tomography. *IEEE Transactions on Biomedical Engineering*, 36(9), 918–924.
- Chitturi, V., & Farrukh, N. (2017). Spatial resolution in electrical impedance tomography: A topical review. *Journal of Electrical Bioimpedance*, 8(1), 66–78.
- Cho, K., Van Merriënboer, B., Gulcehre, C., Bahdanau, D., Bougares, F., Schwenk, H., & Bengio, Y. (2014). Learning phrase representations using rnn encoder-decoder for statistical machine translation. *arXiv preprint arXiv:1406.1078*.
- Choi, M. H., Kao, T.-J., Isaacson, D., Saulnier, G. J., & Newell, J. C. (2007). A reconstruction algorithm for breast cancer imaging with electrical impedance tomography in mammography geometry. *IEEE transactions on biomedical engineering*, 54(4), 700–710.
- Cotter, S. F., Rao, B. D., Engan, K., & Kreutz-Delgado, K. (2005). Sparse solutions to linear inverse problems with multiple measurement vectors. *IEEE Transactions on Signal Processing*, 53(7), 2477–2488.
- Davalos, R. V., Otten, D. M., Mir, L. M., & Rubinsky, B. (2004). Electrical impedance tomography for imaging tissue electroporation. *IEEE Transactions on Biomedical Engineering*, 51(5), 761–767.
- Del Agua, I., Marina, S., Pitsalidis, C., Mantione, D., Ferro, M., Iandolo, D., . . . Mecerreyes, D. (2018). Conducting polymer scaffolds based on poly (3, 4-ethylenedioxythiophene) and xanthan gum for live-cell monitoring. *ACS omega*, 3(7), 7424–7431.
- De León, S. E., Pupovac, A., & McArthur, S. L. (2020). Three-dimensional (3d) cell culture monitoring: Opportunities and challenges for impedance spectroscopy. *Biotechnology and bioengineering*, 117(4), 1230–1240.
- Deng, W., Yin, W., & Zhang, Y. (2013). Group sparse optimization by alternating direction method. In *Wavelets and sparsity xv* (Vol. 8858, pp. 242–256).
- Dmitriev, R. I. (2017). *Multi-parametric live cell microscopy of 3d tissue models* (Vol. 1035). Springer.
- Donahue, J., Anne Hendricks, L., Guadarrama, S., Rohrbach, M., Venugopalan, S., Saenko, K., & Darrell, T. (2015). Long-term recurrent convolutional networks for visual recognition and description. In *Proceedings of the IEEE conference on computer vision and pattern recognition* (pp. 2625–2634).
- Dosovitskiy, A., Beyer, L., Kolesnikov, A., Weissenborn, D., Zhai, X., Unterthiner, T., . . . others (2020). An image is worth 16x16 words: Transformers for image recognition at scale. *arXiv preprint arXiv:2010.11929*.

- Duan, X., Taurand, S., & Soleimani, M. (2019). Artificial skin through super-sensing method and electrical impedance data from conductive fabric with aid of deep learning. *Scientific reports*, 9(1), 1–11.
- Fan, H., Su, H., & Guibas, L. J. (2017). A point set generation network for 3d object reconstruction from a single image. In *Proceedings of the IEEE conference on computer vision and pattern recognition* (pp. 605–613).
- Fu, J., Liu, J., Tian, H., Li, Y., Bao, Y., Fang, Z., & Lu, H. (2019). Dual attention network for scene segmentation. In *Proceedings of the IEEE/CVF conference on computer vision and pattern recognition* (pp. 3146–3154).
- Fukushima, M. (1992). Application of the alternating direction method of multipliers to separable convex programming problems. *Computational Optimization and Applications*, 1, 93–111.
- Gadelha, M., Wang, R., & Maji, S. (2018). Multiresolution tree networks for 3d point cloud processing. In *Proceedings of the European conference on computer vision (ECCV)* (pp. 103–118).
- Gehre, M., Kluth, T., Lipponen, A., Jin, B., Seppänen, A., Kaipio, J. P., & Maass, P. (2012). Sparsity reconstruction in electrical impedance tomography: an experimental evaluation. *Journal of Computational and Applied Mathematics*, 236(8), 2126–2136.
- González, G., Huttunen, J., Kolehmainen, V., Seppänen, A., & Vauhkonen, M. (2016). Experimental evaluation of 3d electrical impedance tomography with total variation prior. *Inverse Problems in Science and Engineering*, 24(8), 1411–1431.
- González, G., Kolehmainen, V., & Seppänen, A. (2017). Isotropic and anisotropic total variation regularization in electrical impedance tomography. *Computers & Mathematics with Applications*, 74(3), 564–576.
- Goren, N., Avery, J., Dowrick, T., Mackle, E., Witkowska-Wrobel, A., Werring, D., & Holder, D. (2018). Multi-frequency electrical impedance tomography and neuroimaging data in stroke patients. *Scientific data*, 5(1), 1–10.
- Gregor, K., & LeCun, Y. (2010). Learning fast approximations of sparse coding. In *Proceedings of the 27th international conference on international conference on machine learning* (pp. 399–406).
- Griffiths, H., Tucker, M., Sage, J., & Herrenden-Harker, W. (1996). An electrical impedance tomography microscope. *Physiological Measurement*, 17(4A), A15.
- Groeber, F., Engelhardt, L., Egger, S., Werthmann, H., Monaghan, M., Walles, H., & Hansmann, J. (2015). Impedance spectroscopy for the non-destructive evaluation of in vitro epidermal models. *Pharmaceutical research*, 32, 1845–1854.

- Groueix, T., Fisher, M., Kim, V. G., Russell, B. C., & Aubry, M. (2018). A papier-mâché approach to learning 3d surface generation. In *Proceedings of the IEEE conference on computer vision and pattern recognition* (pp. 216–224).
- Guo, M.-H., Cai, J.-X., Liu, Z.-N., Mu, T.-J., Martin, R. R., & Hu, S.-M. (2021). Pct: Point cloud transformer. *Computational Visual Media*, 7(2), 187–199.
- Guo, Y., Wang, H., Hu, Q., Liu, H., Liu, L., & Bennamoun, M. (2020). Deep learning for 3d point clouds: A survey. *IEEE transactions on pattern analysis and machine intelligence*, 43(12), 4338–4364.
- Hamilton, S. J., Mueller, J., & Santos, T. (2018). Robust computation in 2d absolute eit (a-eit) using d-bar methods with the 'exp' approximation. *Physiological Measurement*, 39(6), 064005.
- Hamilton, S. J., et al. (2018). Deep d-bar: Real-time electrical impedance tomography imaging with deep neural networks. *IEEE transactions on medical imaging*, 37(10), 2367–2377.
- Han, X.-F., Laga, H., & Bennamoun, M. (2019). Image-based 3d object reconstruction: State-of-the-art and trends in the deep learning era. *IEEE transactions on pattern analysis and machine intelligence*, 43(5), 1578–1604.
- Harrach, B., & Seo, J. K. (2009). Detecting inclusions in electrical impedance tomography without reference measurements. *SIAM Journal on Applied Mathematics*, 69(6), 1662–1681.
- He, K., Gkioxari, G., Dollár, P., & Girshick, R. (2017). Mask r-cnn. In *Proceedings of the IEEE international conference on computer vision* (pp. 2961–2969).
- He, K., Zhang, X., Ren, S., & Sun, J. (2016). Deep residual learning for image recognition. In *Proceedings of the IEEE conference on computer vision and pattern recognition* (pp. 770–778).
- He, Q., Sun, X., Yan, Z., & Fu, K. (2021). Dabnet: Deformable contextual and boundary-weighted network for cloud detection in remote sensing images. *IEEE Transactions on Geoscience and Remote Sensing*, 60, 1–16.
- Henderson, R. P., & Webster, J. G. (1978). An impedance camera for spatially specific measurements of the thorax. *IEEE Transactions on Biomedical Engineering*(3), 250–254.
- Hu, D., Lu, K., & Yang, Y. (2019). Image reconstruction for electrical impedance tomography based on spatial invariant feature maps and convolutional neural network. In *2019 IEEE international conference on imaging systems and techniques (ist)* (pp. 1–6).

- Huang, J., & Zhang, T. (2010). The benefit of group sparsity. *The Annals of Statistics*(4), 1978 – 2004. Retrieved from <https://doi.org/10.1214/09-AOS778> doi: 10.1214/09-AOS778
- Hui, L., Yang, H., Cheng, M., Xie, J., & Yang, J. (2021). Pyramid point cloud transformer for large-scale place recognition. In *Proceedings of the IEEE/CVF International Conference on Computer Vision* (pp. 6098–6107).
- Huttenlocher, D. P., Klanderman, G. A., & Rucklidge, W. J. (1993). Comparing images using the hausdorff distance. *IEEE Transactions on Pattern Analysis and Machine Intelligence*, 15(9), 850–863.
- Jang, J., Lee, S., Kim, K., & Choi, B. (2006). Modified iterative landweber method in electrical capacitance tomography. *Measurement Science and Technology*, 17(7), 1909.
- Jiang, L., Shi, S., Qi, X., & Jia, J. (2018). Gal: Geometric adversarial loss for single-view 3d-object reconstruction. In *Proceedings of the European Conference on Computer Vision (ECCV)* (pp. 802–816).
- Jin, B., Khan, T., & Maass, P. (2012). A reconstruction algorithm for electrical impedance tomography based on sparsity regularization. *International Journal for Numerical Methods in Engineering*, 89(3), 337–353.
- Johnson, J., Alahi, A., & Fei-Fei, L. (2016). Perceptual losses for real-time style transfer and super-resolution. In *Computer Vision—ECCV 2016: 14th European Conference, Amsterdam, The Netherlands, October 11–14, 2016, Proceedings, Part II 14* (pp. 694–711).
- Justice, B. A., Badr, N. A., & Felder, R. A. (2009). 3d cell culture opens new dimensions in cell-based assays. *Drug Discovery Today*, 14(1-2), 102–107.
- Kato, H., Ushiku, Y., & Harada, T. (2018). Neural 3d mesh renderer. In *Proceedings of the IEEE Conference on Computer Vision and Pattern Recognition* (pp. 3907–3916).
- Kazhdan, M., & Hoppe, H. (2013). Screened poisson surface reconstruction. *ACM Transactions on Graphics (TOG)*, 32(3), 1–13.
- Khademhosseini, A., & Langer, R. (2016). A decade of progress in tissue engineering. *Nature Protocols*, 11(10), 1775–1781.
- Khambampati, A., Liu, D., Konki, S., & Kim, K. (2018). An automatic detection of the ROI using otsu thresholding in nonlinear difference EIT imaging. *IEEE Sensors Journal*, 18(12), 5133–5142.
- Kingma, D. P., & Ba, J. (2014). Adam: A method for stochastic optimization. *arXiv preprint arXiv:1412.6980*.

- Knudsen, K., Lassas, M., Mueller, J. L., & Siltanen, S. (2007). D-bar method for electrical impedance tomography with discontinuous conductivities. *SIAM Journal on Applied Mathematics*, 67(3), 893–913.
- Knudsen, K., Lassas, M., Mueller, J. L., & Siltanen, S. (2009). Regularized d-bar method for the inverse conductivity problem. *Inverse Problems and Imaging*, 35(4), 599.
- K'Owino, I. O., & Sadik, O. A. (2005). Impedance spectroscopy: a powerful tool for rapid biomolecular screening and cell culture monitoring. *Electroanalysis: An International Journal Devoted to Fundamental and Practical Aspects of Electroanalysis*, 17(23), 2101–2113.
- Krizhevsky, A., Sutskever, I., & Hinton, G. E. (2017). Imagenet classification with deep convolutional neural networks. *Communications of the ACM*, 60(6), 84–90.
- LeCun, Y., Bottou, L., Bengio, Y., & Haffner, P. (1998). Gradient-based learning applied to document recognition. *Proceedings of the IEEE*, 86(11), 2278–2324.
- Lee, E. J., Wi, H., McEwan, A. L., Farooq, A., Sohal, H., Woo, E. J., . . . Oh, T. I. (2014). Design of a microscopic electrical impedance tomography system for 3d continuous non-destructive monitoring of tissue culture. *Biomedical engineering online*, 13, 1–15.
- Lee, J., Yoon, W., Kim, S., Kim, D., Kim, S., So, C. H., & Kang, J. (2020). Biobert: a pre-trained biomedical language representation model for biomedical text mining. *Bioinformatics*, 36(4), 1234–1240.
- Lei, K. F., Liu, T.-K., & Tsang, N.-M. (2018). Towards a high throughput impedimetric screening of chemosensitivity of cancer cells suspended in hydrogel and cultured in a paper substrate. *Biosensors and Bioelectronics*, 100, 355–360.
- Li, F., Tan, C., & Dong, F. (2020). Electrical resistance tomography image reconstruction with densely connected convolutional neural network. *IEEE Transactions on Instrumentation and Measurement*, 70, 1–11.
- Li, X., Yang, F., He, W., & Rubinsky, B. (2019). A theoretical study on real time monitoring of single cell mitosis with micro electrical impedance tomography. *Biomedical Microdevices*, 21, 1–10.
- Linderholm, P., Marescot, L., Loke, M. H., & Renaud, P. (2007). Cell culture imaging using microimpedance tomography. *IEEE Transactions on Biomedical Engineering*, 55(1), 138–146.
- Liu, D., Kolehmainen, V., Siltanen, S., & Seppänen, A. (2015). A nonlinear approach to difference imaging in eit; assessment of the robustness in the presence of modelling errors. *Inverse Problems*, 31(3), 035012.

- Liu, S., Huang, Y., Wu, H., Tan, C., & Jia, J. (2020). Efficient multitask structure-aware sparse bayesian learning for frequency-difference electrical impedance tomography. *IEEE Transactions on industrial informatics*, 17(1), 463–472.
- Liu, S., Jia, J., Zhang, Y. D., & Yang, Y. (2018). Image reconstruction in electrical impedance tomography based on structure-aware sparse bayesian learning. *IEEE transactions on medical imaging*, 37(9), 2090–2102.
- Liu, S., Wu, H., Huang, Y., Yang, Y., & Jia, J. (2019). Accelerated structure-aware sparse bayesian learning for three-dimensional electrical impedance tomography. *IEEE transactions on industrial informatics*, 15(9), 5033–5041.
- Lu, Y., Zhu, B., Darne, C. D., Tan, I.-C., Rasmussen, J. C., & Sevick-Muraca, E. M. (2011). Improvement of fluorescence-enhanced optical tomography with improved optical filtering and accurate model-based reconstruction algorithms. *Journal of biomedical optics*, 16(12), 126002.
- Lukaschewitsch, M., Maass, P., & Pidcock, M. (2003). Tikhonov regularization for electrical impedance tomography on unbounded domains. *Inverse Problems*, 19(3), 585.
- Luvizon, D. C., Picard, D., & Tabia, H. (2020). Multi-task deep learning for real-time 3d human pose estimation and action recognition. *IEEE transactions on pattern analysis and machine intelligence*, 43(8), 2752–2764.
- Ma, N., Zhang, X., Zheng, H.-T., & Sun, J. (2018). Shufflenet v2: Practical guidelines for efficient cnn architecture design. In *Proceedings of the european conference on computer vision (eccv)* (pp. 116–131).
- Mahfouzi, S. H., Amoabediny, G., Doryab, A., Safiabadi-Tali, S. H., & Ghanei, M. (2018). Noninvasive real-time assessment of cell viability in a three-dimensional tissue. *Tissue Engineering Part C: Methods*, 24(4), 197–204.
- Malone, E., Dos Santos, G. S., Holder, D., & Arridge, S. (2013). Multifrequency electrical impedance tomography using spectral constraints. *IEEE transactions on medical imaging*, 33(2), 340–350.
- Mandikal, P., & Radhakrishnan, V. B. (2019). Dense 3d point cloud reconstruction using a deep pyramid network. In *2019 IEEE winter conference on applications of computer vision (wacv)* (pp. 1052–1060).
- McDermott, B., Elahi, A., Santorelli, A., O'Halloran, M., Avery, J., & Porter, E. (2020). Multi-frequency symmetry difference electrical impedance tomography with machine learning for human stroke diagnosis. *Physiological Measurement*, 41(7), 075010.

- Mescheder, L., Oechsle, M., Niemeyer, M., Nowozin, S., & Geiger, A. (2019). Occupancy networks: Learning 3d reconstruction in function space. In *Proceedings of the IEEE/CVF conference on computer vision and pattern recognition* (pp. 4460–4470).
- Metherall, P., Barber, D. C., Smallwood, R. H., & Brown, B. H. (1996). Three-dimensional electrical impedance tomography. *Nature*, *380*(6574), 509–512.
- Miklavčič, D., Pavšelj, N., & Hart, F. X. (2006). Electric properties of tissues. *Wiley encyclopedia of biomedical engineering*.
- Monga, V., Li, Y., & Eldar, Y. C. (2021). Algorithm unrolling: Interpretable, efficient deep learning for signal and image processing. *IEEE Signal Processing Magazine*, *38*(2), 18–44.
- Muller, P. A., Mueller, J. L., Mellenthin, M., Murthy, R., Capps, M., Wagner, B. D., . . . Hoppe, J. (2018). Evaluation of surrogate measures of pulmonary function derived from electrical impedance tomography data in children with cystic fibrosis. *Physiological measurement*, *39*(4), 045008.
- Nachman, A. I. (1996). Global uniqueness for a two-dimensional inverse boundary value problem. *Annals of Mathematics*, 71–96.
- Nair, V., & Hinton, G. E. (2010). Rectified linear units improve restricted boltzmann machines. In *Proceedings of the 27th international conference on machine learning (icml-10)* (pp. 807–814).
- Ngiam, J., Khosla, A., Kim, M., Nam, J., Lee, H., & Ng, A. Y. (2011). Multimodal deep learning. In *Proceedings of the 28th international conference on machine learning (icml-11)* (pp. 689–696).
- Obozinski, G., Taskar, B., & Jordan, M. I. (2010). Joint covariate selection and joint subspace selection for multiple classification problems. *Statistics and Computing*, *20*, 231–252.
- Pan, Y., Hu, N., Wei, X., Gong, L., Zhang, B., Wan, H., & Wang, P. (2019). 3d cell-based biosensor for cell viability and drug assessment by 3d electric cell/matrigel-substrate impedance sensing. *Biosensors and Bioelectronics*, *130*, 344–351.
- Park, J. J., Florence, P., Straub, J., Newcombe, R., & Lovegrove, S. (2019). Deepsdf: Learning continuous signed distance functions for shape representation. In *Proceedings of the IEEE/CVF conference on computer vision and pattern recognition* (pp. 165–174).
- Pumarola, A., Agudo, A., Porzi, L., Sanfeliu, A., Lepetit, V., & Moreno-Noguer, F. (2018). Geometry-aware network for non-rigid shape prediction from a single view. In *Proceedings of the IEEE conference on computer vision and pattern recognition* (pp. 4681–4690).

- Qu, Q., Nasrabadi, N.-N. M., & Tran, T. D. (2013). Abundance estimation for bilinear mixture models via joint sparse and low-rank representation. *IEEE Transactions on Geoscience and Remote Sensing*, 52(7), 4404–4423.
- Radu, V., Tong, C., Bhattacharya, S., Lane, N. D., Mascolo, C., Marina, M. K., & Kawsar, F. (2018). Multimodal deep learning for activity and context recognition. *Proceedings of the ACM on Interactive, Mobile, Wearable and Ubiquitous Technologies*, 1(4), 1–27.
- Rahman, A., Register, J., Vuppala, G., & Bhansali, S. (2008). Cell culture monitoring by impedance mapping using a multielectrode scanning impedance spectroscopy system (cellmap). *Physiological measurement*, 29(6), S227.
- Ravi, M., Paramesh, V., Kaviya, S., Anuradha, E., & Solomon, F. P. (2015). 3d cell culture systems: advantages and applications. *Journal of cellular physiology*, 230(1), 16–26.
- Romsauerova, A., McEwan, A., Horesh, L., Yerworth, R., Bayford, R., & Holder, D. S. (2006). Multi-frequency electrical impedance tomography (eit) of the adult human head: initial findings in brain tumours, arteriovenous malformations and chronic stroke, development of an analysis method and calibration. *Physiological measurement*, 27(5), S147.
- Ronneberger, O., Fischer, P., & Brox, T. (2015). U-net: Convolutional networks for biomedical image segmentation. In *Medical image computing and computer-assisted intervention—miccai 2015: 18th international conference, munich, germany, october 5-9, 2015, proceedings, part iii 18* (pp. 234–241).
- Rumelhart, D. E., Hinton, G. E., & Williams, R. J. (1986). Learning representations by back-propagating errors. *nature*, 323(6088), 533–536.
- Sadleir, R. J., Sajib, S. Z., Kim, H. J., Kwon, O. I., & Woo, E. J. (2013). Simulations and phantom evaluations of magnetic resonance electrical impedance tomography (mreit) for breast cancer detection. *Journal of Magnetic Resonance*, 230, 40–49.
- Santos, S. A., Czaplik, M., Orschulik, J., Hochhausen, N., & Leonhardt, S. (2018). Lung pathologies analyzed with multi-frequency electrical impedance tomography: Pilot animal study. *Respiratory physiology & neurobiology*, 254, 1–9.
- Schullcke, B., Gong, B., Krueger-Ziolek, S., Soleimani, M., Mueller-Lisse, U., & Moeller, K. (2016). Structural-functional lung imaging using a combined ct-eit and a discrete cosine transformation reconstruction method. *Scientific reports*, 6(1), 25951.
- Shi, X., Chen, Z., Wang, H., Yeung, D.-Y., Wong, W.-K., & Woo, W.-c. (2015). Convolutional lstm network: A machine learning approach for precipitation nowcasting. *Advances in neural information processing systems*, 28.

- Tan, C., Lv, S., Dong, F., & Takei, M. (2018). Image reconstruction based on convolutional neural network for electrical resistance tomography. *IEEE Sensors Journal*, 19(1), 196–204.
- Tehrani, J. N., McEwan, A., Jin, C., & Van Schaik, A. (2012). L1 regularization method in electrical impedance tomography by using the l1-curve (pareto frontier curve). *Applied Mathematical Modelling*, 36(3), 1095–1105.
- Torrey, L., & Shavlik, J. (2010). Transfer learning. In *Handbook of research on machine learning applications and trends: algorithms, methods, and techniques* (pp. 242–264). IGI global.
- Vaswani, A., Shazeer, N., Parmar, N., Uszkoreit, J., Jones, L., Gomez, A. N., . . . Polosukhin, I. (2017). Attention is all you need. *Advances in neural information processing systems*, 30.
- Vinci, M., Gowan, S., Boxall, F., Patterson, L., Zimmermann, M., Lomas, C., . . . others (2012). Advances in establishment and analysis of three-dimensional tumor spheroid-based functional assays for target validation and drug evaluation. *BMC biology*, 10(1), 29.
- Wang, G., et al. (2020). Deep learning for tomographic image reconstruction. *Nature Machine Intelligence*, 2(12), 737–748.
- Wang, G., Ye, J. C., Mueller, K., & Fessler, J. A. (2018). Image reconstruction is a new frontier of machine learning. *IEEE transactions on medical imaging*, 37(6), 1289–1296.
- Wang, J., Huang, J., Zhang, F., & Wang, W. (2020). Group sparse recovery in impulsive noise via alternating direction method of multipliers. *Applied and Computational Harmonic Analysis*, 49(3), 831–862.
- Wang, N., Zhang, Y., Li, Z., Fu, Y., Liu, W., & Jiang, Y.-G. (2018). Pixel2mesh: Generating 3d mesh models from single rgb images. In *Proceedings of the european conference on computer vision (eccv)* (pp. 52–67).
- Wang, X., Girshick, R., Gupta, A., & He, K. (2018). Non-local neural networks. In *Proceedings of the ieee conference on computer vision and pattern recognition* (pp. 7794–7803).
- Watzenig, D., & Fox, C. (2009). A review of statistical modelling and inference for electrical capacitance tomography. *Measurement Science and Technology*, 20(5), 052002.
- Wei, Z., Liu, D., & Chen, X. (2019). Dominant-current deep learning scheme for electrical impedance tomography. *IEEE Transactions on Biomedical Engineering*, 66(9), 2546–2555.

- Wu, H., Yang, Y., Bagnaninchi, P. O., & Jia, J. (2018). Electrical impedance tomography for real-time and label-free cellular viability assays of 3d tumour spheroids. *Analyst*, *143*(17), 4189–4198.
- Wu, H., Zhou, W., Yang, Y., Jia, J., & Bagnaninchi, P. (2018). Exploring the potential of electrical impedance tomography for tissue engineering applications. *Materials*, *11*(6), 930.
- Wu, J., Wang, Y., Xue, T., Sun, X., Freeman, B., & Tenenbaum, J. (2017). Marnet: 3d shape reconstruction via 2.5 d sketches. *Advances in neural information processing systems*, *30*.
- Xiang, J., Dong, Y., & Yang, Y. (2021). Fista-net: Learning a fast iterative shrinkage thresholding network for inverse problems in imaging. *IEEE Transactions on Medical Imaging*, *40*(5), 1329–1339.
- Xie, H., Yao, H., Sun, X., Zhou, S., & Zhang, S. (2019). Pix2vox: Context-aware 3d reconstruction from single and multi-view images. In *Proceedings of the IEEE/CVF international conference on computer vision* (pp. 2690–2698).
- Yang, L., Dai, M., Xu, C., Zhang, G., Li, W., Fu, F., . . . Dong, X. (2017). The frequency spectral properties of electrode-skin contact impedance on human head and its frequency-dependent effects on frequency-difference eit in stroke detection from 10hz to 1mhz. *PloS one*, *12*(1), e0170563.
- Yang, Y., & Jia, J. (2017a). An image reconstruction algorithm for electrical impedance tomography using adaptive group sparsity constraint. *IEEE Transactions on Instrumentation and Measurement*, *66*(9), 2295–2305.
- Yang, Y., & Jia, J. (2017b). A multi-frequency electrical impedance tomography system for real-time 2d and 3d imaging. *Review of Scientific Instruments*, *88*(8), 085110.
- Yang, Y., Jia, J., Polydorides, N., & McCann, H. (2014). Effect of structured packing on eit image reconstruction. In *2014 IEEE international conference on imaging systems and techniques (IST) proceedings* (pp. 53–58).
- Yang, Y., Jia, J., Smith, S., Jamil, N., Gamal, W., & Bagnaninchi, P.-O. (2016). A miniature electrical impedance tomography sensor and 3-d image reconstruction for cell imaging. *IEEE Sensors Journal*, *17*(2), 514–523.
- Yang, Y., Sun, J., Li, H., & Xu, Z. (2018). Admm-csnet: A deep learning approach for image compressive sensing. *IEEE transactions on pattern analysis and machine intelligence*, *42*(3), 521–538.

- Yang, Y., Wu, H., & Jia, J. (2017). Image reconstruction for electrical impedance tomography using enhanced adaptive group sparsity with total variation. *IEEE Sensors Journal*, 17(17), 5589–5598.
- Yang, Y., Wu, H., & Jia, J. (2018). Quasi-2d eit-optical dual modality sensor for cellular imaging. *Electrical Impedance Tomography*, 47.
- Yang, Y., Wu, H., Jia, J., & Bagnaninchi, P.-O. (2019). Scaffold-based 3-d cell culture imaging using a miniature electrical impedance tomography sensor. *IEEE Sensors Journal*, 19(20), 9071–9080.
- Yang, Z., Dai, Z., Yang, Y., Carbonell, J., Salakhutdinov, R. R., & Le, Q. V. (2019). Xlnet: Generalized autoregressive pretraining for language understanding. *Advances in neural information processing systems*, 32.
- Yin, X., Wu, H., Jia, J., & Yang, Y. (2018). A micro eit sensor for real-time and non-destructive 3-d cultivated cell imaging. *IEEE Sensors Journal*, 18(13), 5402–5412.
- Zhang, D., Yang, Z., Jiang, S., Zhou, Z., Meng, M., & Wang, W. (2020). Automatic segmentation and applicator reconstruction for ct-based brachytherapy of cervical cancer using 3d convolutional neural networks. *Journal of Applied Clinical Medical Physics*, 21(10), 158–169.
- Zhang, J., & Ghanem, B. (2018). Ista-net: Interpretable optimization-inspired deep network for image compressive sensing. In *Proceedings of the IEEE conference on computer vision and pattern recognition* (pp. 1828–1837).
- Zhang, K., Li, M., Yang, F., Xu, S., & Abubakar, A. (2019). Three-dimensional electrical impedance tomography with multiplicative regularization. *IEEE Transactions on Biomedical Engineering*, 66(9), 2470–2480.
- Zhang, L., Wang, G., & Giannakis, G. B. (2019). Real-time power system state estimation and forecasting via deep unrolled neural networks. *IEEE Transactions on Signal Processing*, 67(15), 4069–4077.
- Zhang, M., Ma, Y., Huang, N., & Ge, H. (2022). Survey of eit image reconstruction algorithms. *Journal of Shanghai Jiaotong University (Science)*, 27(2), 211–218.
- Zhang, M., Zhu, L., Wang, H., Li, Y., Soleimani, M., & Yang, Y. (2020). Multiple measurement vector-based complex-valued multifrequency ect. *IEEE Transactions on Instrumentation and Measurement*, 70, 1–10.
- Zhang, X., Wang, Z., Fu, R., Wang, D., Chen, X., Guo, X., & Wang, H. (2022). V-shaped dense denoising convolutional neural network for electrical impedance tomography. *IEEE Transactions on Instrumentation and Measurement*, 71, 1–14.

- Zheng, J., et al. (2018). An autoencoder-based image reconstruction for electrical capacitance tomography. *IEEE Sensors Journal*, 18(13), 5464–5474.
- Zhou, Z., dos Santos, G. S., Dowrick, T., Avery, J., Sun, Z., Xu, H., & Holder, D. S. (2015). Comparison of total variation algorithms for electrical impedance tomography. *Physiological measurement*, 36(6), 1193.
- Ziniel, J., & Schniter, P. (2012). Efficient high-dimensional inference in the multiple measurement vector problem. *IEEE Transactions on Signal Processing*, 61(2), 340–354.
- Zong, Z., Wang, Y., & Wei, Z. (2020). A review of algorithms and hardware implementations in electrical impedance tomography. *Progress In Electromagnetics Research*, 169, 59–71.